



**Alison Tatiana Madrid Sani**

**Addition of divalent cations ( $Zn^{2+}$ ,  $Ni^{2+}$ ) to  $ZrMgMo_3O_{12}$  and  
their effects on physical properties**

**Dissertação de Mestrado**

Dissertation presented to the Programa de Pós-Graduação em Engenharia de Materiais e de Processos Químicos e Metalúrgicos of PUC-Rio in partial fulfillment of the requirements for the degree of Mestre em Engenharia de Materiais e de Processos Químicos e Metalúrgicos.

Advisor: Prof. Bojan Marinkovic

Rio de Janeiro

August 2019



**Alison Tatiana Madrid Sani**

**Addition of divalent cations ( $Zn^{2+}$ ,  $Ni^{2+}$ ) to  $ZrMgMo_3O_{12}$  and  
their effects on physical properties**

Dissertation presented to the Programa de Pós-graduação em Engenharia de Materiais e de Processos Químicos e Metalúrgicos of PUC-Rio in partial fulfillment of the requirements for the degree of Mestre em Engenharia de Materiais e de Processos Químicos e Metalúrgicos. Approved by the undersigned Examination Committee.

**Prof. Bojan Marinkovic**

Advisor

Departamento de Engenharia Química e de Materiais – PUC-Rio

**Prof. Roberto Ribeiro de Avillez**

Departamento de Engenharia Química e de Materiais – PUC-Rio

**Profa. Paula Mendes Jardim**

Departamento de Engenharia Metalúrgica e de Materiais UFRJ

All rights reserved.

### **Alison Tatiana Madrid Sani**

Majored in Biotechnology Engineering at Universidad de las Fuerzas Armadas-ESPE (Quito–Ecuador, 2017). She has experience in the synthesis of nanostructures, materials with negative and near zero thermal expansion.

#### Bibliographic data

Madrid Sani, Alison Tatiana

Addition of divalent cations ( $Zn^{2+}$ ,  $Ni^{2+}$ ) to  $ZrMgMo_3O_{12}$  and their effects on physical properties / Alison Tatiana Madrid Sani; advisor: Bojan Marinkovic.– 2019.

94 f.: il. (color.); 30 cm

Dissertação (mestrado)– Pontifícia Universidade Católica do Rio de Janeiro, Departamento de Engenharia Química e de Materiais, 2019.

Inclui bibliografia

1. Engenharia Química e de Materiais – Teses. 2. Expansão térmica próxima a zero. 3. Coeficiente de expansão térmica. 4. Transição de fase. I. Marinkovic, Bojan. II. Pontifícia Universidade Católica do Rio de Janeiro. Departamento de Engenharia Química e de Materiais. III. Título.

CDD: 620.11

To my parents Edison and Mariana,  
To my sister Karen,  
To my husband Danilo and my son Mateo.

## Acknowledgments

To my advisor, professor Bojan Marinkovic, for all the time dedicated to our project. I am infinitely grateful for your valuable teachings in the classroom and throughout the process of carrying out this work. Thanks for trusting and for the incentive to continue growing personally and professionally. My admiration and respect for him.

To my mentor and friend Patricia Pontón, who motivated me to accomplish this goal, without her it would not have been possible, my eternal gratitude.

To professor Mary Anne White and to Michel Johnson for their contribution with this project, as well as for their participation in our scientific article.

To professor Flávio García and Professor Waldeci Paraguassu for their assistance with the use of XRPD and Raman Spectroscopy.

To our research group, especially to Tamires Martinhão for imparting me her knowledge. To Yuri dos Santos for his assistance in the synthesis process. To Anja Dosen and Juliana Viol for their patience with characterization. To Isabella Loureiro, Lucas Almeida, Freddy Rojas and Fabián Orozco for the great teamwork made and for their great friendship.

This study was financed in part by the Coordenação de Aperfeiçoamento de Pessoal de Nível Superior – Brasil (CAPES) – Finance Code 001.

I mainly thank my parents for the example and education they gave me, for trusting me and for supporting me in the realization of this great professional dream. Without their love and incentive, I would never have come here.

To my husband Danilo and my beloved son Mateo, thank you very much for so much love, thank you very much for waiting. The rest of my life will be with you.

I love them.

## Abstract

Madrid Sani, Alison Tatiana; Marinkovic, Bojan (advisor). Addition of divalent cations ( $Zn^{2+}$ ,  $Ni^{2+}$ ) to  $ZrMgMo_3O_{12}$  and their effects on physical properties. Rio de Janeiro, 2019. 94p. Dissertação de mestrado – Departamento de Engenharia Química e de Materiais, Pontifícia Universidade Católica do Rio de Janeiro.

Although the vast majority of materials dilates when heated and contract when cooled, there is a class of materials that contracts or does not change their dimensions when heated, presenting a negative thermal expansion coefficient (NTE) or close to zero (ZTE), respectively. The possibility of reducing the coefficient of thermal expansion while increasing its physical properties has been the main driving force in the search for crystalline phases within the  $A_2M_3O_{12}$  family and its subfamilies. In the present study, we propose to synthesize two new systems,  $ZrMg_{1-x}Zn_xMo_3O_{12}$  ( $x = 0.1, 0.3, 0.35, 0.4$ ) and  $ZrMg_{1-x}Ni_xMo_3O_{12}$  ( $x = 0.05; 0.1, 0.15, 0.2$ ), to try to reduce the coefficient of thermal expansion of the  $ZrMgMo_3O_{12}$  phase. The solubility limit of  $Zn^{2+}$  and  $Ni^{2+}$  in the  $ZrMgMo_3O_{12}$  system is in the range of  $0.35 \leq x \leq 0.4$  and  $0.1 \leq x \leq 0.2$ , respectively. The lowest coefficient of thermal expansion ( $\alpha_l = 2.82 \times 10^{-7} K^{-1}$ ) was obtained for the composition  $x = 0.1$  in the  $ZrMg_{1-x}Zn_xMo_3O_{12}$  system in the temperature range of 213 K to 298 K. In this system, the phase transition from monoclinic to orthorhombic was observed, occurring below the room temperature for all compositions from  $x = 0.1$  to  $x = 0.4$ . This transition temperature increases as the  $Zn^{2+}$  composition increases. Analyzes of thermogravimetry indicated that the phases of the two systems are not hygroscopic. Applying the Kubelka-Munk equation, and considering an indirect transition to  $ZrMg_{1-x}Zn_xMo_3O_{12}$ , it was concluded that there are no significant differences in the band gap energy of the analyzed phases. However, for an indirect transition to  $ZrMg_{1-x}Ni_xMo_3O_{12}$  there is a decrease in energy of the band energy, as  $Ni^{2+}$  content increases in composition, in addition to the appearance of absorption in the visible spectrum due to d-d transition. Finally, the results of this study showed that it is possible to obtain a ceramic material, within the systems studied, that presents a thermal expansion behavior close to zero.

## **Keywords**

Near zero thermal expansion; coefficient of thermal expansion; thermal shock resistance; phase transition.

## Resumo

Madrid Sani, Alison Tatiana; Marinkovic, Bojan. **Adição de cátions divalentes ( $Zn^{2+}$ ,  $Ni^{2+}$ ) à  $ZrMgMo_3O_{12}$  e seus efeitos sobre propriedades físicas.** Rio de Janeiro, 2019. 94p. Dissertação de Mestrado-Departamento de Engenharia Química e de Materiais, Pontifícia Universidade Católica do Rio de Janeiro.

Embora a grande maioria dos materiais dilate quando aquecida e contraia quando resfriada, existe uma classe de materiais que se contrai, ou não muda de dimensões, ao aquecida, apresentando um coeficiente de expansão térmica negativo (ETN) ou próximo à zero (ETZ), respectivamente. A possibilidade de reduzir significativamente o coeficiente de expansão térmica, e ao mesmo tempo, incrementar suas propriedades físicas tem sido a principal força motriz na busca por fases cristalinas dentro da família  $A_2M_3O_{12}$  e suas subfamílias. Tendo isso em vista, a proposta deste estudo foi sintetizar dois sistemas novos,  $ZrMg_{1-x}Zn_xMo_3O_{12}$  ( $x=0,1; 0,3; 0,35; 0,4$ ) e  $ZrMg_{1-x}Ni_xMo_3O_{12}$  ( $x=0,05; 0,1; 0,15; 0,2$ ), para tentar reduzir o coeficiente de expansão térmica da fase mãe, a  $ZrMgMo_3O_{12}$ . O limite de solubilidade de  $Zn^{2+}$  e  $Ni^{2+}$  no sistema  $ZrMgMo_3O_{12}$  se encontra no intervalo de  $0,35 \leq x \leq 0,4$  e  $0,1 \leq x \leq 0,2$ , respectivamente. O menor coeficiente de expansão térmica ( $\alpha_t = 2,82 \times 10^{-7} K^{-1}$ ) foi obtido para a composição  $x=0,1$  no sistema  $ZrMg_{1-x}Zn_xMo_3O_{12}$  na faixa de temperatura de 213 K a 298 K. Neste sistema, a transição de fase de monoclinica para ortorrômbica foi observada, ocorrendo abaixo da temperatura ambiente para todas as composições de  $x=0,1$  a  $x=0,4$ . Esta temperatura de transição aumenta conforme aumenta a composição de  $Zn^{2+}$ . As análises de termogravimetria indicaram que as fases dos dois sistemas não são higroscópicas. Aplicando a equação de Kubelka-Munk, e considerando uma transição indireta para o  $ZrMg_{1-x}Zn_xMo_3O_{12}$ , concluiu-se que não existem diferenças significativas na energia de banda proibida das fases analisadas. No entanto, para uma transição indireta para o  $ZrMg_{1-x}Ni_xMo_3O_{12}$  existe um decréscimo da energia da banda de energia, conforme o conteúdo de  $Ni^{2+}$  aumenta na composição, além do surgimento da absorção no espectro visível devido à transição d-d. Por fim, os resultados deste estudo mostraram que é possível obter um material cerâmico, dentro dos sistemas estudados, que apresente um comportamento de expansão térmica próxima à zero.

## **Palavras-chave**

Expansão térmica próxima a zero; Coeficiente de expansão térmica;  
Transição de fase.

# Contents

1 Introduction	18
2 Literature review	20
2.1. Thermal properties	20
2.2. Fundamentals of thermal expansion	20
2.2.1. Coefficient of thermal expansion (CTE)	21
2.2.2. Materials with negative thermal expansion coefficient (NTE) and near-zero thermal expansion materials (NZTE)	23
2.3. Families of thermomiotic materials	25
2.4. $A_2M_3O_{12}$ Family	26
2.4.1. $ABM_3O_{12}$ subfamily	26
2.4.2. Structure	27
2.4.3. Phase transition and electronegativity	28
2.4.4. Anisotropic thermal expansion	29
2.4.5. Hygroscopicity	30
2.5. Effect of the substitution of $A^{2+}$ cation in $A_2M_3O_{12}$ family	31
2.6. Relation between attractive forces ( $F_a$ ) and $A^{3+}$ cations in $A_2M_3O_{12}$ family	32
2.7. Relation between thermal shock resistance and CTE	34
2.8. Merit figure for thermal shock resistance	35
2.9. Heat capacity ( $C_p$ )	37
2.10. Thermal conductivity	38
2.11. Applications of thermomiotic materials	39
3 Objectives	22
3.1. General Objective	22
3.2. Specific objectives	22
4 Materials and methods	42
4.1. Solid state reaction	42

4.1.1. Synthesis of $\text{ZrMg}_{1-x}(\text{Zn/Ni})_x\text{Mo}_3\text{O}_{12}$ systems	42
4.2. Characterization of $\text{ZrMg}_{1-x}(\text{Zn/Ni})_x\text{Mo}_3\text{O}_{12}$ systems	43
4.2.1. X-ray powder diffraction (XRPD)	43
4.2.2. High temperature X-ray powder diffraction	43
4.2.3. Low temperature X-ray powder diffraction	44
4.2.4. Thermogravimetry (TGA)	44
4.2.5. Differential Scanning Calorimetry (DSC)	45
4.2.6. Diffuse Reflectance Spectroscopy (DRS)	45
4.2.7. Raman Spectroscopy	45
5 Results and discussions	47
5.1. Phase composition	47
5.2. Determination of the solubility limit of $\text{Zn}^{2+}$ and $\text{Ni}^{2+}$ in $\text{ZrMg}_{1-x}(\text{Zn/Ni})_x\text{Mo}_3\text{O}_{12}$ systems	51
5.3. Phase transition temperature	57
5.3.1. Phase transition temperature by XRPD	57
5.3.2. Phase transition temperature by DSC	59
5.4. Thermal expansion coefficient at low temperatures	61
5.5. Thermal expansion coefficient at high temperatures	63
5.6. Hygroscopicity in $\text{ZrMg}_{1-x}\text{Zn/Ni}_x\text{Mo}_3\text{O}_{12}$ systems	66
5.7. Effect of the addition of $\text{Zn}^{2+}$ and $\text{Ni}^{2+}$ cations on the UV-Vis absorption in $\text{ZrMg}_{1-x}\text{Zn}_x\text{Mo}_3\text{O}_{12}$ and $\text{ZrMg}_{1-x}\text{Ni}_x\text{Mo}_3\text{O}_{12}$ systems	68
5.8. Raman Spectroscopy	72
6 Conclusions and future works	79
7 References	81

## List of Figures

Figure 1- Potential energy curves as a function of the interatomic distance ( $r$ ) for an ideal harmonic system (dashed curve) and a real asymmetric system (full curve) [6]. Interatomic distances due to heating are given by hollow or full circles, depending on the type of curves.....	21
Figure 2- Longitudinal vibrations (left), which increase the average distance between the external atoms due to the asymmetry of the potential energy curve. Transversal vibrations (right), which decrease that average distance between the non-bonding atoms [12]. .....	24
Figure 3- Above: Octahedral motif and its mechanism of rotation between octahedra. Down: Structure of $ZrW_2O_8$ which contains tetrahedra and octahedra, and its mechanism of rotation between polyhedral [16].....	25
Figure 4- Nuclear Magnetic Resonance (NMR)-refined structure of $ZrMgMo_3O_{12}$ . O atoms are shown in red, $MgO_6$ coordination polyhedral in orange, $ZrO_6$ in green, and $MoO_4$ tetrahedra in purple [2]. .....	27
Figure 5- Temperature of the monoclinic to orthorhombic phase transitions in $A_2M_3O_{12}$ as a function of the electronegativity of $A^{3+}$ ions [15].....	29
Figure 6- Linear and volumetric thermal expansion coefficients for $Al_{2x}Fe_{2-2x}Mo_3O_{12}$ as a function of $Al^{3+}$ [4]. .....	30
Figure 7- Distortion of the $AO_6$ polyhedron as a function of the $A^{3+}$ cationic radius in the $A_2M_3O_{12}$ family [2]. .....	32

Figure 8- Coefficient of linear thermal expansion ( $\alpha_l$ ) as a function of the $AO_6$ distortion of $A_2M_3O_{12}$ family [2].....	32
Figure 9- Coefficient of thermal expansion as a function of A site ionic attractive force in $A_2M_3O_{12}$ family [2].....	33
Figure 10- Heat capacity of MgO, SiC, $Al_2O_3$ and $3Al_2O_3 \cdot 2SiO_2$ (mullite) as a function of temperature [7].....	37
Figure 11- Schematic representation of the synthesis of $ZrMg_{1-x}(Zn/Ni)_xMo_3O_{12}$ system by solid state reaction. ....	43
Figure 12- Diffraction pattern of $ZrMgMo_3O_{12}$ adjusted by Le Bail method. ....	48
Figure 13- Diffraction patterns of a) $ZrMg_{1-x}Zn_xMo_3O_{12}$ and b) $ZrMg_{1-x}Ni_xMo_3O_{12}$ .....	49
Figure 14-X-ray diffraction patterns for a) $ZrMg_{1-x}Zn_xMo_3O_{12}$ phases and b) $ZrMg_{1-x}Ni_xMo_3O_{12}$ phases, showing the characteristic peaks of orthorhombic crystal system for the $ABM_3O_{12}$ subfamily. ....	50
Figure 15- Diffraction pattern for a) $ZrZnMo_3O_{12}$ composition with two phases (*) hexagonal $ZrMo_2O_8$ and (.) monoclinic $ZnMoO_4$ and for b) $ZrNiMo_3O_{12}$ composition with two phases (*)hexagonal $ZrMo_2O_8$ and (.) monoclinic $NiMoO_4$ .....	51
Figure 16- X-ray diffraction patterns of the composition $x=0.1; 0.3; 0.35$ and $0.4$ of the $ZrMg_{1-x}Zn_xMo_3O_{12}$ system in the range from $10^\circ$ to $60^\circ$ ( $2\theta$ ) with $ZrMo_2O_8$ as a second phase. The arrow is marking the position of $ZrMo_2O_8$ diffraction line.....	52

Figure 17- X-ray diffraction patterns adjusted by the Le Bail method of the compositions: a)  $ZrMg_{0.9}Zn_{0.1}Mo_3O_{12}$  b)  $ZrMg_{0.7}Zn_{0.3}Mo_3O_{12}$  and c)  $ZrMg_{0.65}Zn_{0.35}Mo_3O_{12}$ . (\*) Peak associated with the space group  $P-3_1c$  of hexagonal  $ZrMo_2O_8$ . ..... 54

Figure 18- X-ray diffraction pattern adjusted by the Le Bail method of the compositions  $ZrMg_{0.6}Zn_{0.4}Mo_3O_{12}$  (\*) Peaks associated with the trigonal space group  $P-3_1c$  of  $ZrMo_2O_8$  phase. (·) Peaks associated with the monoclinic space group  $C2/m$ , of  $ZnMoO_4$ ..... 55

Figure 19- a) X-ray diffraction pattern adjusted by the LeBail method for  $ZrMg_{0.9}Ni_{0.1}Mo_3O_{12}$ . and b)  $ZrMg_{0.8}Ni_{0.2}Mo_3O_{12}$  . (·) Peaks associated with the trigonal space group  $P-3_1c$  of  $ZrMo_2O_8$  phase. (\*) Peaks associated with the monoclinic space group  $C2/m$ , of  $NiMoO_4$ ..... 57

Figure 20- Diffraction pattern lines for a)  $ZrMgMo_3O_{12}$ , b)  $ZrMg_{0.9}Zn_{0.1}Mo_3O_{12}$ , c)  $ZrMg_{0.7}Zn_{0.3}Mo_3O_{12}$  and d)  $ZrMg_{0.65}Zn_{0.35}Mo_3O_{12}$ . (↓) Characteristic pick which corresponds to the transition of monoclinic to orthorhombic structure by the division of peak at  $22^\circ-22.5^\circ$  ( $2\theta$ ). ..... 58

Figure 21- a) Diffraction pattern of  $ZrMg_{0.95}Ni_{0.05}Mo_3O_{12}$  system and b) Diffraction pattern of  $ZrMg_{0.9}Ni_{0.1}Mo_3O_{12}$  system. (↓) Characteristic pick which corresponds to the transition of monoclinic to orthorhombic structure by the division of peak at  $22^\circ-22.5^\circ$  ( $2\theta$ ). ..... 59

Figure 22- Onset temperatures getting by DSC. As increasing  $Zn^{2+}$  composition in  $ZrMg_{1-x}Zn_xMo_3O_{12}$ ; the phase transition temperature increase..... 60

Figure 23-DSC curves for  $ZrMg_{0.95}Ni_{0.05}Mo_3O_{12}$  and  $ZrMg_{0.9}Ni_{0.1}Mo_3O_{12}$  phases..... 61

Figure 24- Coefficients of thermal expansion for $\text{ZrMg}_{0.9}\text{Zn}_{0.1}\text{Mo}_3\text{O}_{12}$ phase in three crystallographic directions and volumetric one; a) a-axes, b) b-axes c) c-axes and d) volume.....	63
Figure 26- Coefficients of thermal expansion for $\text{ZrMg}_{0.7}\text{Zn}_{0.3}\text{Mo}_3\text{O}_{12}$ phase in three crystallographic directions and volume; a) a-axes, b) b-axes c) c-axes and d) volume. ....	64
Figure 27- Weight loss for $\text{ZrMg}_{1-x}\text{Zn}_x\text{Mo}_3\text{O}_{12}$ system. ....	66
Figure 28- Weight loss as a function of temperature for $\text{ZrMg}_{1-x}\text{Ni}_x\text{Mo}_3\text{O}_{12}$ system. ....	67
Figure 29- Kubelka-Munk plots of $\text{ZrMg}_{1-x}\text{Zn}_x\text{Mo}_3\text{O}_{12}$ system, regarding an indirect transition as a function of excitation energy and the extrapolations $(F(R)h\nu)^{1/2} = 0$ used to obtain the band-gap energies.....	69
Figure 30- Kubelka-Munk curves of $\text{ZrMg}_{1-x}\text{Ni}_x\text{Mo}_3\text{O}_{12}$ system, considering an indirect transition. ....	70
Figure 31- UV-Vis spectra for $\text{ZrMg}_{1-x}\text{Ni}_x\text{Mo}_3\text{O}_{12}$ system.....	71
Figure 32- Raman spectra for precursor oxides ( $\text{ZnO}$ , $\text{MgO}$ , $\text{ZrO}_2$ and $\text{MoO}_3$ ). ....	73
Figure 33- Raman spectrum of the a) $\text{ZrMg}_{0.7}\text{Zn}_{0.3}\text{Mo}_3\text{O}_{12}$ , b) $\text{ZrMg}_{0.8}\text{Ni}_{0.2}\text{Mo}_3\text{O}_{12}$ , and c) $\text{ZrMgMo}_3\text{O}_{12}$ systems and depicts spectral information of five points of the phases.....	74
Figure 35- Raman spectrum of a) $\text{ZrMg}_{0.65}\text{Zn}_{0.35}\text{Mo}_3\text{O}_{12}$ and b) $\text{ZrMg}_{0.9}\text{Ni}_{0.1}\text{Mo}_3\text{O}_{12}$ . (*) represents $\text{Zr}_2\text{Mo}_2\text{O}_8$ .....	76
Figure 36- Raman spectra of $\text{ZrMg}_{1-x}\text{Zn}_x\text{Mo}_3\text{O}_{12}$ , where $x=0.3$ , $0.35$ and $0.4$ . (*) Represents the peak of $\text{ZnMoO}_4$ phase.....	77

Figure 37- Raman spectrum of  $\text{ZrMg}_{1-x}\text{Ni}_x\text{Mo}_3\text{O}_{12}$ , where  $x=0, 0.1$   
and  $0.2$ . (\*) Represents the peak of  $\text{NiMoO}_4$ . ..... 78

## List of Tables

Table 1-	Extrinsic coefficient of thermal expansion ( $\alpha_e$ ) and intrinsic coefficient of thermal expansion ( $\alpha_i$ ) of some compounds of the $A_2M_3O_{12}$ family [23].....	26
Table 2-	Linear thermal expansion coefficient for some phases inside $HfMg_{1-x}Zn_xMo_3O_{12}$ system.....	30
Table 3-	Coefficient of linear thermal expansion for some ceramic materials [50].....	31
Table 4-	Thermal shock resistance moderate and severe parameters for some ceramics [51].....	33
Table 5.	Thermal conductivity for some ceramic materials..	35
Table 6-	R factors obtained by Le Bail adjustment for $ZrMgMo_3O_{12}$ and $ZrMg_{1-x}Zn_xMo_3O_{12}$ system.....	44
Table 7-	Transition Temperature (K) of $ZrMg_{1-x}Zn_xMo_3O_{12}$ system determined by DSC .....	56
Table 8-	Temperatures of phase transition of $ZrMg_{1-x}Ni_xMo_3O_{12}$ determined by DSC.....	57
Table 9-	Near zero thermal expansion coefficients for some $ZrMg_{1-x}Zn_xMo_3O_{12}$ phases.....	60
Table 10-	Near zero thermal expansion coefficients for some $A_2M_3O_{12}$ phases, according to the literature.....	60
Table 11-	Weight loss in $ZrMg_{1-x}Zn_xMo_3O_{12}$ system as determined by TGA.....	61
Table 12-	Weight loss in $ZrMg_{1-x}Ni_xMo_3O_{12}$ system as determined by TGA.....	62
Table 13-	Band-gap energies for $ZrMg_{1-x}Zn_xMo_3O_{12}$ system.....	64
Table 14-	Band-gap energie of $ZrMg_{1-x}Ni_xMo_3O_{12}$ system..	65
Table 15-	Assignment of vibrational modes of Raman spectra obtained in this work (according to the literature).....	70

# 1 Introduction

Considered as the one of the main scientific and technological challenges in the applications that require high thermal shock resistance, such as transparent infrared windows, missile domes or glass-ceramic for induction cookers, materials that have coefficients of thermal expansion (CTE) close to zero would be perfect candidates for those applications [1]. In this context, the substitution of  $Zn^{2+}$  (0.074 nm) and  $Ni^{2+}$  (0.069 nm) by  $Mg^{2+}$  (0.072nm) radii in the  $ZrMgMo_3O_{12}$  phase would have the purpose of controlling the thermal expansion, obtaining materials with thermal expansion close to zero (considered to be in the range of  $10^{-7}K^{-1}$  or lower). For such a purpose it is relevant to establish the solubility limit of these two elements inside  $ZrMgMo_3O_{12}$ , since this will impact the extant of  $Zn^{2+}$  and  $Ni^{2+}$  influence over CTE of the parent phase  $ZrMgMo_3O_{12}$ . Systems are characterized in order to know their hygroscopicity and possible phase transition, two relevant properties for eventual applications of these phases. It is reported that  $ZrMgMo_3O_{12}$  has a coefficient of thermal expansion of  $\alpha_1 = 1.6 \pm 0.2 \times 10^{-7} K^{-1}$  from 25 °C to 450 °C, crystallizing in an orthorhombic structure [2], although another report brought much higher CTE for this phase with  $\alpha_1 = -3.8 \times 10^{-7} K^{-1}$  from 300K to 1000K [3]. A phase transition for  $ZrMgMo_3O_{12}$  only occurs below room temperature [3]. Therefore with these two systems  $ZrMg_{1-x}Zn_xMo_3O_{12}$  and  $ZrMg_{1-x}Ni_xMo_3O_{12}$  an efficient reduction of the coefficient of thermal expansion without phase transition can possibly be achieved in accordance to the substitution of higher cation radius ( $Zn^{2+}$ ) which could produce weaker Zn-O bonds, consequently less rigid octahedra and more negative the CTE will be. In the other hand with a smaller cationic radius ( $Ni^{2+}$ ) could produce stronger Ni-O bonds, more rigid the octahedra, so less negative the CTE will be [4].

This work is organized as follows:

Chapter 2: Literature review, which summarizes the thermal properties and optical properties by the theoretical foundation of the study, emphasizing the theory of thermal expansion. Characteristics of the  $A_2M_3O_{12}$  family are presented, as well as

the main relationships between ion attraction forces and cation size. Thermal shock, heat capacity, thermal conductivity are described, as the relevant properties for this study. In addition, some applications of NZTE materials have been reviewed.

- Chapter 3: The objectives of the study are presented.
- Chapter 4: This chapter describes the materials and methods used for the synthesis and characterization of the proposed systems.
- Chapter 5: Presents results obtained in this study and discussed them through a theoretical foundation.
- Chapter 6: Conclusions and future works

## 2 Literature review

### 2.1. Thermal properties

The thermal properties are associated with a response of a material when it has been exposed to temperature. This response can cause in the material phase transitions, change of its volume, energy storage, thermal conductivity melting/decomposition, chemical reactions and even the rupture of a material due to thermal stresses [5]. The thermally induced fracture in a ceramic material is a very common occurrence due to its inherent fragility and low thermal conductivity. In addition to the development of stresses, if these stresses are very high, the ceramic will generate and propagate cracks [6]. However, a proper use of thermal properties, such as thermal expansion and conductivity, could improve the fracture resistance of ceramic materials.

An increase of temperature in a certain material will generate vibration of the atoms, which depends on type and strength of interatomic bonds and crystal structure. Among the most important thermal properties are thermal expansion, heat capacity, thermal conductivity and thermal shock resistance [7].

### 2.2. Fundamentals of thermal expansion

The most common effects caused by temperature variations in bodies or substances are the changes in their dimensions and phase transitions. Thermal expansion is the change of any linear dimension of the solid body, such as its length, height or width, which occurs when temperature raises [8].

The majority of known solids have a positive coefficient of thermal expansion (PTE); that is, they expand on heating [9]. The phenomenon of PTE can be understood by understanding the potential energy curve as a function of interatomic distance. An increase in the average distance between the neighboring atoms will cause a lengthening of the bonds; an overall effect is dilatation of the

material due to the asymmetry of the potential energy curve. Figure 1, where the x-axis represents the interatomic distances, while the y-axis represents the potential energy, depicts the equilibrium interatomic distance at 0K, and it corresponds to the minimum point of the potential energy curve. When heating occurs, the vibrational (kinetic) energy increases, and thus, as the potential energy curve is, more or less, asymmetric for all materials the mean distances between the atoms increase, resulting in expansion of the material [6].

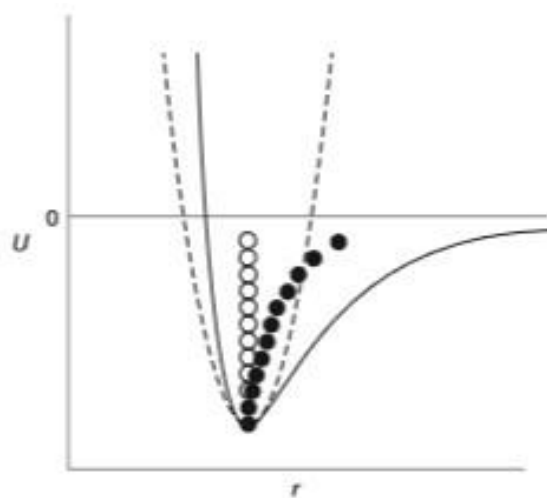


**Figure 1-** Potential energy curves as a function of the interatomic distance ( $r$ ) for an ideal harmonic system (dashed curve) and a real asymmetric system (full curve) [6]. Interatomic distances due to heating are given by hollow or full circles, depending on the type of curves.

A positive thermal expansion could be explained by the intrinsic asymmetry of the potential energy curve; however, negative thermal expansion (NTE) cannot be explained based on the behavior of interatomic bonds showed in Figure 1.

For an explication of NTE it is necessary to consider other mechanisms that can overcome the PTE of interatomic bonds, such as vibrational effects or non-vibrational mechanisms, which emerge from ferroelectric or magnetic effects, or phase transitions [10].

### 2.2.1. Coefficient of thermal expansion (CTE)

Each material has a specific relation between its temperature and its thermal deformation. This relationship is represented by the coefficient of thermal

expansion (CTE), which is the measure of the deformation that the material undergoes to the addition of a unit of temperature. Most thermal expansion measurements on solids are of linear thermal expansion coefficient ( $\alpha_l$ )[10]. Mathematically, the CTE is defined by Equation 1 and Equation 2 [6]:

**Equation 1:** Linear Thermal Expansion Coefficient

$$\alpha_l = \frac{1}{l_0} \left( \frac{dl}{dT} \right)_p$$

Where:

$\alpha_l$ = Linear Thermal Expansion Coefficient

$l_0$  = original length

$\frac{dl}{dT}$ =Rate of change of linear dimension per unit change in temperature

**Equation 2:** Volumetric Thermal Expansion Coefficient

$$\alpha_v = \frac{1}{V_0} \left( \frac{dV}{dT} \right)_p$$

Where:

$\alpha_v$ = Volumetric Thermal Expansion Coefficient

$V_0$ = Original material volume

$\frac{dV}{dT}$ = Rate of volume variation as a function of temperature variation

The unit of measure of the CTE is the inverse of the temperature ( $^{\circ}\text{C}^{-1}$  or  $\text{K}^{-1}$ ). When the CTE is measured in only one direction, the symbol ( $\alpha_l$ ) is adopted, and it is called the coefficient of linear thermal expansion.

Thermal expansion may occur in isotropic or anisotropic form. Temperature-isotropic materials undergo the same expansion in either direction of the crystallographic axes and therefore volumetric CTE  $\alpha_v$  and linear CTE  $\alpha_l$  have the following correlation expressed by Equation 3.

**Equation 3:** Relation between CTE  $\alpha_v$  and linear CTE  $\alpha_l$

$$\alpha_l = \frac{\alpha_v}{3}$$

Where:

$\alpha_l$ = Linear Thermal Expansion Coefficient

$\alpha_v$ = Volumetric Thermal Expansion Coefficient

The non-cubic materials do not have isotropic behavior under the effect of temperature, and the extent of their volume expansion will depend on the crystallographic direction. Thus, to quantify the anisotropic thermal expansion, it is common to define it as a function of a specific crystallographic direction, according to Equation 1.

### 2.2.2.

#### **Materials with negative thermal expansion coefficient (NTE) and near-zero thermal expansion materials (NZTE)**

In section 2.2 positive thermal expansion was discussed. However, a select group of materials manages to contract their dimensions and even not produce any significant changes in their dimensions, being known as materials that have negative thermal expansion (NTE) and an expansion close to zero (NZTE), respectively [2].

Because negative and near-zero thermal expansion cannot be explained by the potential energy well as the positive thermal expansion, there is an effect that allows understanding the negative thermal expansion through the transversal movement of oxygen or another ion within the 2-folded coordination. This effect generates a coordinated movement of polyhedra, such tetrahedra and octahedra, which are joined by the vertices, providing a reduction of the volume of the material [11][12].

Phonons play a major role in thermal expansion, except for some materials at very low temperatures [10], and they are represented as collective vibrations of atoms in the crystalline lattice, making an important role in several phenomena in the solid-state. The vibration waves can be propagated in the longitudinal or transverse direction [13]. An example of this phenomenon is explained by an M-O-M bond (where M is a cation and O is Oxygen), shown in Figure 2. As there is an increase in energy due to the increase of temperature, simultaneous longitudinal and transverse vibrations occur [11].

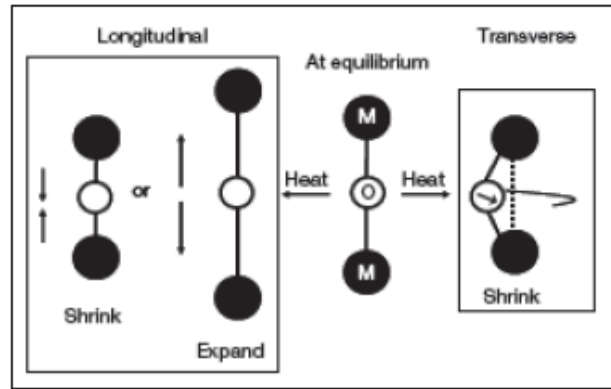


**Figure 2-** Longitudinal vibrations (left), which increase the average distance between the external atoms due to the asymmetry of the potential energy curve. Transversal vibrations (right), which decrease that average distance between the non-bonding atoms [12].

Negative volumetric expansion is most likely to be found in materials consisted of an open crystal structure, where coordination numbers are low [10]. To understand the mechanism of NTE the connection between polyhedra and octahedra in three dimensions through the vertices should be noted, where transverse vibrations generate a rotation movement between the polyhedra. This mechanism considers the rigid unit mode model (RUM) which considers that polyhedra are rigid units that present this rotation among themselves. Figure 3 shows the mechanism for a structure consisted of vertices shared octahedra, as well as for the one consisted of octahedra and tetrahedra, being possible to identify that the average distances between the polyhedrons decrease with the increase of polyhedra twisting, leading to NTE. It is important to mention that NTE is only possible in  $A_2M_3O_{12}$  family when inherent distortion of the  $AO_6$  polyhedron occurs [14][15].

Romao et al.,[12] introduced the term thermomiotic to refer to the materials that have a negative thermal expansion, where thermomiotic is derived from the Greek "thermo" which means heat and "mio" meaning contraction.

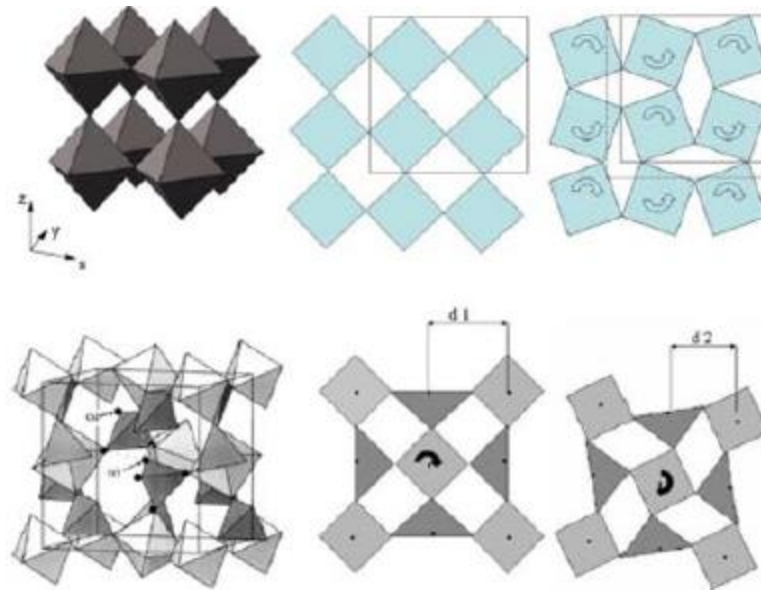


**Figure 3-** Above: Octahedral motif and its mechanism of rotation between octahedra. Down: Structure of  $ZrW_2O_8$  which contains tetrahedra and octahedra, and its mechanism of rotation between polyhedral [16].

NZTE materials would, specially, be less likely to fail when exposed to temperature extremes [12][17]. However, some thermomiotic materials have low thermal conductivities due to the transverse vibrations associated with NTE [18], which would decrease thermal shock resistance, therefore reduction of thermal expansion is important. Those materials that exhibit NZTE could withstand high temperature variations and therefore, have high thermal shock resistance [19] [20].

### 2.3. Families of thermomiotic materials

There are six main ceramics families which present NTE and NZTE:  $AO_3$ ,  $AM_2O_7$ , like  $ZrV_2O_7$ ; studied by Sleight et al,  $AMO_5$ ,  $M_2O$ ,  $AM_2O_8$  like  $ZrW_2O_8$ ; studied by Mary et al, and  $A_2M_3O_{12}$  like  $Sc_2W_3O_{12}$ ; studied by Evans et al., Among them  $A_2M_3O_{12}$  family has, perhaps, the major advantage because of its considerable chemical flexibility to accommodate various bivalent ions within the same crystal structure. It is, in principle, possible to tailor the thermal expansion coefficient to any desired value including zero by forming a suitable solid solution between various members of the family [11] [21] [22].

## 2.4. A<sub>2</sub>M<sub>3</sub>O<sub>12</sub> Family

The A<sub>2</sub>M<sub>3</sub>O<sub>12</sub> family exhibits great variability concerning to its chemical composition. The M cation can be Mo<sup>6+</sup> or W<sup>6+</sup>, and A can be one of many trivalent cations with a huge range of ionic radius including Al, Ga, Sc, In, Y and member of the lanthanide group elements, such as Nd, Ce, Gd, Dy, Ho, Er, Tm, Yb and Lu [23] [24]. Therefore, it is possible to tailor the thermal expansion coefficient to any desired value including zero by forming a suitable solid solution between various members of the family [11].

A<sub>2</sub>M<sub>3</sub>O<sub>12</sub> family may crystallize in either monoclinic or orthorhombic crystal system depending on the electronegativity of the cation A<sup>3+</sup> and temperature [9]. At high temperatures (above room temperature) an orthorhombic structure will be crystallized and for low temperatures (below room temperature) monoclinic structure will be crystallized, this fact could be perfectly seen for Al<sub>2</sub>Mo<sub>3</sub>O<sub>12</sub> phase [25] and AlScMo<sub>3</sub>O<sub>12</sub> phase [26]. It is common to find that the orthorhombic structure presents negative CTE as in the case of In<sub>2</sub>Mo<sub>3</sub>O<sub>12</sub> ( $\alpha_1 = -1.85 \times 10^{-6} \text{ K}^{-1}$ ) [14] and for the monoclinic structure shows a positive CTE as AlScMo<sub>3</sub>O<sub>12</sub> ( $\alpha_1 = 10.8 \times 10^{-6} \text{ K}^{-1}$ ) [26]. [27] Nevertheless some select materials as Sc<sub>2</sub>W<sub>3</sub>O<sub>12</sub> [11], Y<sub>2</sub>W<sub>3</sub>O<sub>12</sub> [28] and Y<sub>2</sub>Mo<sub>3</sub>O<sub>12</sub> [29] do [30] [24]. not appear a phase transition at low temperatures.

In addition to wide choice of trivalent cations, these compounds may contain cations with the valences different than 3 and 6. In the case of A<sub>2</sub>M<sub>3</sub>O<sub>12</sub> family, there are subfamilies such ABM<sub>3</sub>O<sub>12</sub> and ABM<sub>2</sub>XO<sub>12</sub> [31] where trivalent cations can be substituted by divalent and tetravalent cations, while hexavalent cations can be substituted by pentavalent ones, respectively.

### 2.4.1. ABM<sub>3</sub>O<sub>12</sub> subfamily

ABM<sub>3</sub>O<sub>12</sub> subfamily in which A= Hf<sup>4+</sup> / Zr<sup>4+</sup>, B= Mg<sup>2+</sup> / Mn<sup>2+</sup>, M= W<sup>6+</sup> / Mo<sup>6+</sup> like HfMgMo<sub>3</sub>O<sub>12</sub> and ZrMgMo<sub>3</sub>O<sub>12</sub> phases, have been synthesized initially by Marinkovic et al., [27] and Song et al., [3] respectively. The other subfamily corresponds to ABM<sub>2</sub>XO<sub>12</sub> in which A= tetravalent cation, B= trivalent cation, M= W<sup>6+</sup> / Mo<sup>6+</sup> and X= P<sup>5+</sup> / V<sup>5+</sup> like HfScW<sub>2</sub>PO<sub>12</sub> has been studied by Cheng et al. [32].

These compounds also have an open framework crystal structure sharing polyhedra and octahedra.  $ABM_3O_{12}$  phases have been synthesized and characterized for thermal expansion, showing promising and unusually low positive, negative and near-zero thermal expansion. They are also of interest because of the high ionic conductivity, display low magnitude thermal expansion in an orthorhombic space group  $Pna2_1$  such as  $HfMgW_3O_{12}$ . [33][34].

#### 2.4.2. Structure

Orthorhombic and monoclinic molybdates and tungstates of the  $A_2M_3O_{12}$  family consist of corner-sharing  $AO_6$  octahedra and  $MO_4$  tetrahedra. Within this family appear the transverse movements of oxygen in the A-O-M ligations in the orthorhombic structure, a phenomenon responsible for ETN [23][11]. In Figure 4 is showed the atoms positions inside of unit cell for  $A_2M_3O_{12}$  family. [2] It is worth to note that only the corner-sharing orthorhombic structure exhibits NTE properties, because, in this structure, the A-O-M linkages could result in the transverse thermal vibrations of the bridging oxygen, and also the librational or translational vibrations of the A and M atoms. So, vibrations induce the contract of the material with increasing the temperature [35].

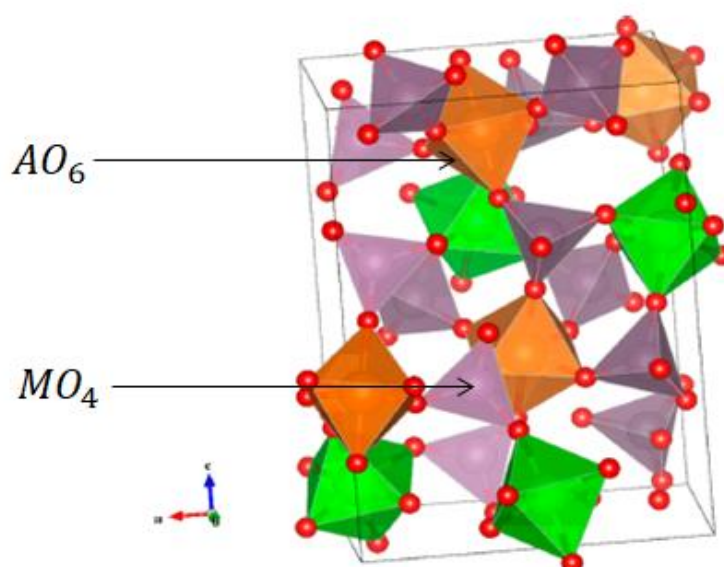


**Figure 4-** Nuclear Magnetic Resonance (NMR)-refined structure of  $ZrMgMo_3O_{12}$ . O atoms are shown in red,  $MgO_6$  coordination polyhedral in orange,  $ZrO_6$  in green, and  $MoO_4$  tetrahedra in purple [2].

### 2.4.3. Phase transition and electronegativity

Another important characteristic of the  $A_2M_3O_{12}$  family is the existence of an orthorhombic-to-monoclinic phase transition because low-temperature monoclinic counterparts of the orthorhombic phases have very different thermal expansion properties and their linear coefficients of thermal expansion are highly positive [9][36].

The materials of the  $A_2M_3O_{12}$  family generally adopt a monoclinic crystal system with a  $P2_1/a$  space group at lower temperatures and an orthorhombic structure with a  $Pbcn$  ( $Pnca$ ) space group at higher temperatures. Many of the compounds assume the monoclinic polymorph only at below ambient temperatures. In both cases, the structure is composed of octahedra of  $AO_6$  that share vertices with tetrahedra of  $MO_4$ . The orthorhombic structure often presents negative CET, but the monoclinic always have CET positive [24][12][16].

Previous studies have reported an interesting relationship between the phase transition temperature (from monoclinic to orthorhombic) and the electronegativity of the cation (A) [9][23]. In this relationship, it is observed that higher electronegativity of the cation (A) leads to higher phase transition temperature. Later studies also highlight the effect of the electronegativity of the cation on the effective oxygen valence. In this relation it is observed that as the cation A is more electronegative, the effective valence of the oxygen decreases, and secondary bonds are induced between the oxygens of neighboring polyhedra. More electronegative A cations would cause less negative oxygens and therefore more stronger secondary bonds which hinder transverse motion of the polyhedra while also keep the phase within monoclinic, and more dense, crystal system. Figure 5 shows this statement in the phase transition temperatures of many molybdates are higher than compounds with trivalent cations of lower electronegativity [15] [37].

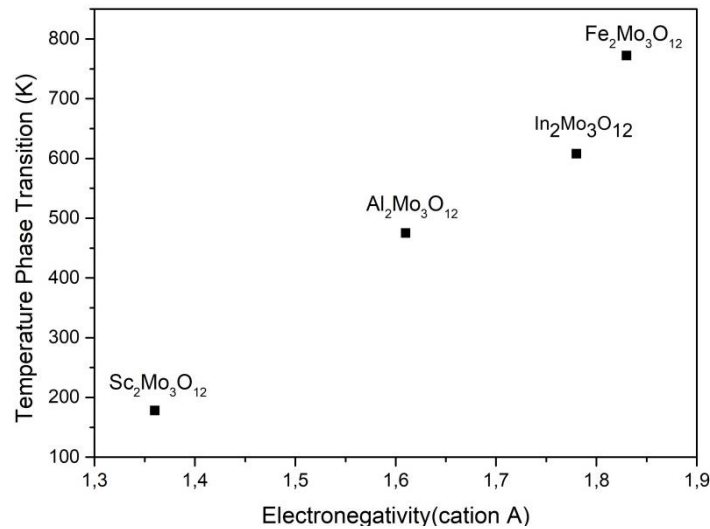


**Figure 5-** Temperature of the monoclinic to orthorhombic phase transitions in  $A_2M_3O_{12}$  as a function of the electronegativity of  $A^{3+}$  ions [15].

#### 2.4.4. Anisotropic thermal expansion

During heating, materials with anisotropic thermal expansion contracting their unit cells in some directions while they are expanding in other directions, this combination sometimes causes a small volume contraction with increasing temperature and a small expanding volume with decreasing temperature [22]. In anisotropic materials, the contraction is small and generally occurs over a small temperature range [38].

The thermal expansion of materials from the  $A_2M_3O_{12}$  family is known to be highly anisotropic, that is the material presents different values of thermal expansion along the crystallographic axes [39] [40]. Such anisotropy can cause large thermal stresses and microcracks in polycrystalline bodies [41]. However, there are exceptions, since  $Al_{1.6}In_{0.4}W_3O_{12}$  studied by Evans et al., [23] shows an isotropic behavior.

Many ceramic materials may exhibit negative thermal expansion when measured by dilatometry, even if the thermal expansion of the unit cell is intrinsically positive, as in the case of  $Al_2W_3O_{12}$  [41], as shown in Table 1. This is because the dilatometry technique considers the changes generated in the dimensions of a material, calling this value as an extrinsic CTE ( $\alpha_e$ ). While the measurement is done by X-ray diffraction, there is based on changes in the lattice parameters of the unit cell, so the value is called as intrinsic CTE ( $\alpha_i$ ). By having

two different values of anisotropy for the same material, discrepancies can be generated for different applications [42].

**Table 1-** Extrinsic coefficient of thermal expansion ( $\alpha_e$ ) and intrinsic coefficient of thermal expansion ( $\alpha_i$ ) of some compounds of the  $A_2M_3O_{12}$  family [23].

Compound	$\alpha_e$ ( $1 \times 10^{-6}$ )	$\alpha_i$ ( $1 \times 10^{-6}$ )
$Al_2W_3O_{12}$	-3	+2.2
$Sc_2W_3O_{12}$	-11	-2.2
$Sc_2Mo_3O_{12}$	-5	-1.1
$Zr_2WP_2O_{12}$	-6	-3

Anisotropic thermal expansion may result in a low positive or near-zero thermal expansion, like  $Al_{2x}Fe_{2-2x}Mo_3O_{12}$  studied by M. Ari et al., [4]. In Figure 6 displayed linear CTE for this system, showing an anisotropic thermal expansion.

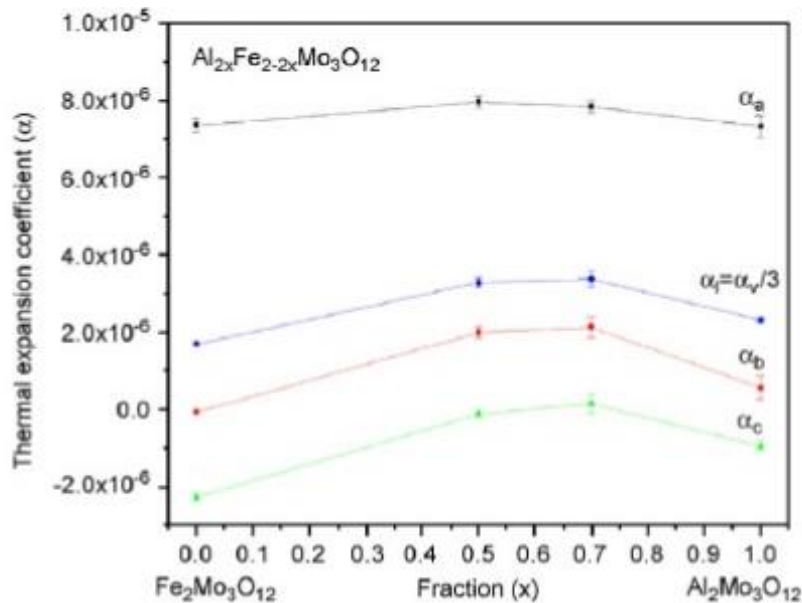


**Figure 6-** Linear and volumetric thermal expansion coefficients for  $Al_{2x}Fe_{2-2x}Mo_3O_{12}$  as a function of  $Al^{3+}$  [4].

#### 2.4.5. Hygroscopicity

There is a property, which describes the ability of a material to take up moisture from the surrounding atmosphere. Materials can interact with the

moisture from the air by absorbing water vapor at room temperatures, in other words, hygroscopicity is a measure of interaction between water and material. This ability may vary depending on the material structure [43].

The hygroscopicity is one of the most important properties to be taken into account in the NTE and NZTE because the entrance of water molecules in the unit cell of a certain material hinders the vibrational modes that induce the NTE. Phases such as  $Y_2M_3O_{12}$  and  $Y_2W_3O_{12}$  are two examples of highly hygroscopic materials, where it was observed that the entrance of water molecules in the microchannels can partially cause amorphization of these phases. Wu et. al, identified that the oxygen of water molecule is associated with the cation of  $Y^{3+}$  and the two hydrogens form a hydrogen bond with the nearest oxygen, interpreting that when the  $A^{3+}$  cation is larger, the phase will be hygroscopic and will directly affect the NTE at room temperature [12][44].

## 2.5.

### Effect of the substitution of $A^{2+}$ cation in $A_2M_3O_{12}$ family

As already described in this chapter, the mechanism responsible for the NTE and the NZTE is attributed to the transverse vibrations of polyhedra in the unit cell. In general, a larger distortion of this polyhedron is generated when the cation  $A^{2+}$  is larger [45]. However, the distortions of the octahedral belonging to the  $A_2M_3O_{12}$  family do not have a linear increase with the cationic radius, Figure 7 shows the percentage of  $AO_6$  polyhedra distortion as a function of different cation radius.

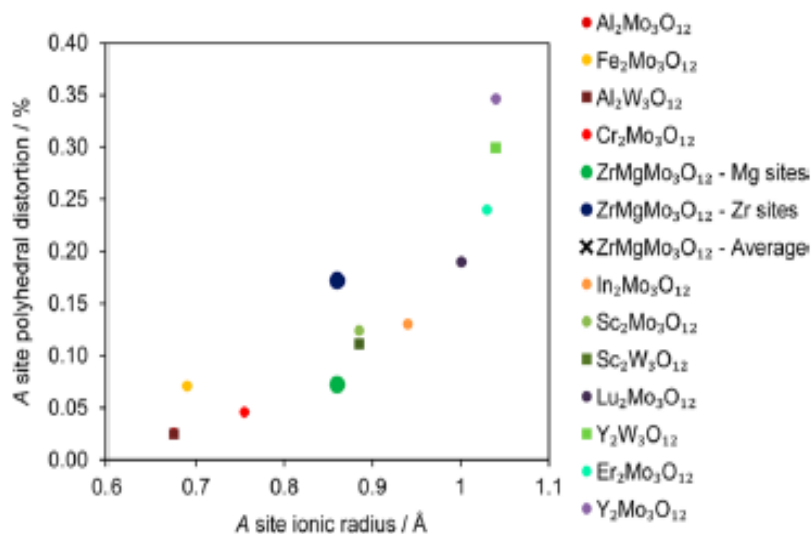


**Figure 7-** Distortion of the  $AO_6$  polyhedron as a function of the  $A^{3+}$  cationic radius in the  $A_2M_3O_{12}$  family [2].

To quantitatively assess the distortion of the polyhedra, the distortion parameter of the volume ( $v$ ) was proposed by Makovicky et al., [37]. This parameter has been introduced by Marinkovic et al., [15]. These authors determined that this parameter has a very important relationship with the linear CET ( $\alpha_l$ ) in  $A_2M_3O_{12}$  family, as shown in Figure 8. Although phases like  $Y_2Mo_3O_{12}$  and  $Y_2W_3O_{12}$  have the same cation A, the octahedron  $YO_6$  generates a greater distortion for molybdate than for tungstate, explaining a lower CET and it is observed that a chemical substitution dramatically influences in the thermal expansion properties of materials in  $A_2M_3O_{12}$  family [46].

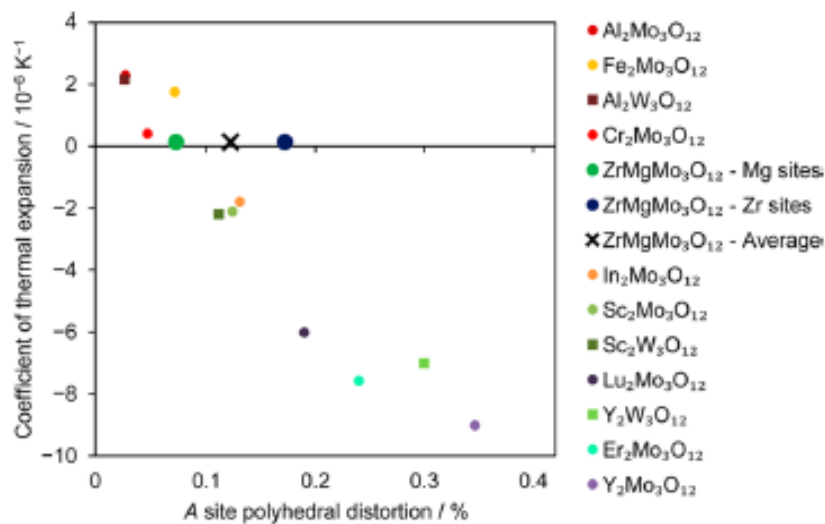


**Figure 8-** Coefficient of linear thermal expansion ( $\alpha_l$ ) as a function of the  $AO_6$  distortion of  $A_2M_3O_{12}$  family [2].

## 2.6.

### Relation between attractive forces ( $F_a$ ) and $A^{3+}$ cations in $A_2M_3O_{12}$ family

Romao et al,[2] suggested a rationalization that relates the ion attraction forces ( $F_a$ ) between A-O inside  $AO_6$  polyhedra with CTE of  $A_2M_3O_{12}$ -type phases. The Equation 4 describes mathematically  $F_a$  as a function of interionic distances and their valences [47].

**Equation 4:** Ionic attraction force between  $A^{2+/3+/4+}$  cation and  $O^{2-}$  anion.

$$F_a = \frac{-kZ_+Z_-e^2}{r_o^2}$$

Where  $k = 8.987 \times 10^9 \text{ Nm}^2/\text{C}^2$  is the Coulomb constant,  $Z_+$  is the average cation valence,  $Z_-$  is the average anion valence,  $e = 1.602 \times 10^{-19} \text{ C}$  is the electron charge and  $r_o$  is the sum of the cationic and anionic radii [45]. As shown in Figure 9, when the ionic attraction force increases, the value of CTE increases. As displayed in Figure 9, with the increase of distortion of the  $\text{AO}_6$  polyhedra in the family  $\text{A}_2\text{M}_3\text{O}_{12}$ , is possible to reach coefficient of thermal expansion close to zero.

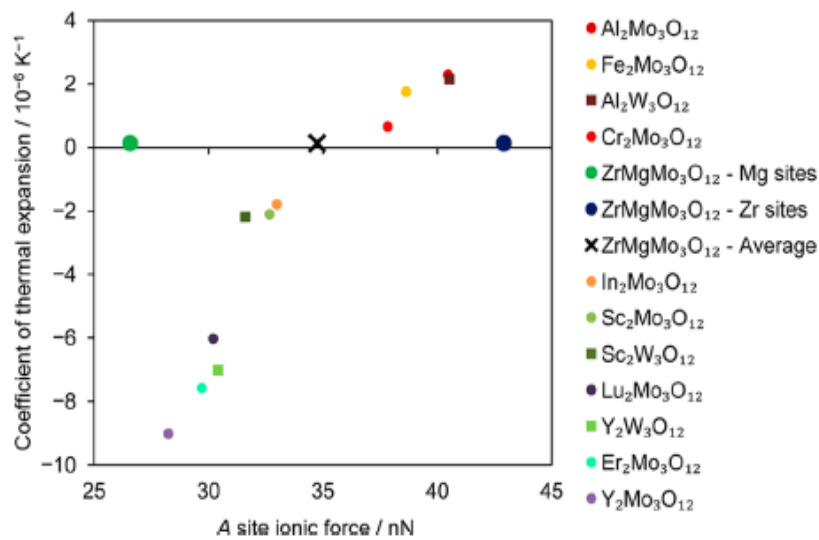


**Figure 9-** Coefficient of thermal expansion as a function of A site Ionic attractive force in  $\text{A}_2\text{M}_3\text{O}_{12}$  family [2].

From the Equation 4, it is observed that with increase of the distance between the ions, smaller the ionic attraction force will be. Transverse vibrations cause a slight distortion of the polyhedra ( $\text{AO}_6$ ) [47]. This distortion depends on the attraction force between the cation and the oxygen anion. Thus, when larger is the cationic radius, weaker the A-O bonds will be and consequently less rigid the octahedron and more negative the CTE will be [47].

This behavior would be expected for the partial substitution of  $\text{Zn}^{2+}$  (0.074nm) by  $\text{Mg}^{2+}$  (0.072nm) in  $\text{ZrMgMo}_3\text{O}_{12}$  system. On the other hand with a partial substitution of a smaller cationic radius  $\text{Ni}^{2+}$  (0.069nm) by  $\text{Mg}^{2+}$  (0.074nm), stronger bonds between Ni-O will be, established, thus, more rigid the octahedra become and higher CTE will be. Under this context, if the partial

substitution of these ions could be made successfully, a fine tuning of CTE of  $\text{ZrMgMo}_3\text{O}_{12}$  might be possible. Li et al., [48] has studied the effects of partial substitution of  $\text{Mg}^{2+}$  ( 0.072 nm) by  $\text{Zn}^{2+}$  ( 0.074 nm) in  $\text{HfMg}_{1-x}\text{Zn}_x\text{Mo}_3\text{O}_{12}$ , where it can be observed that the cation with larger radius generates a lower coefficient of thermal expansion ( $\alpha_1$ ), as can be showed in Table 2.

**Table 2-** Linear thermal expansion coefficient for some phases inside  $\text{HfMg}_{1-x}\text{Zn}_x\text{Mo}_3\text{O}_{12}$  system.

Phase	$\alpha_1$ ( $\times 10^{-6}\text{K}^{-1}$ )
$\text{HfMgMo}_3\text{O}_{12}$	0.96
$\text{HfMg}_{0.8}\text{Zn}_{0.2}\text{Mo}_3\text{O}_{12}$	0.37
$\text{HfMg}_{0.7}\text{Zn}_{0.3}\text{Mo}_3\text{O}_{12}$	0.29

## 2.7.

### Relation between thermal shock resistance and CTE

Thermal shock is defined as the ability of a material to resist a fracture when it is exposed either to abrupt heating or cooling [49]. Most materials, when exposed to drastic temperature gradients, tend to break. In the case of ceramic materials that have a lower coefficient of thermal expansion, such as the *Pyrex* glass brand, with a CTE  $\alpha_1 = 3.3 \times 10^{-6}\text{C}^{-1}$  in a range of 20 to 400 °C are more resistant than the similar materials with higher CTE. In this way, this glass not only supports repeated thermal shocks but also allows the manufacture of increasingly thicker materials [8]. According to studies of CTE, pyrex is one of the most lowest material with this behavior as depicted in Table 3 in a comparison with other materials.

**Table 3-** Coefficient of linear thermal expansion for some ceramic materials [50].

Material	$\alpha_1$ ( $\times 10^{-6} \text{K}^{-1}$ )
Silhouette	14.0
Ceramco	13.4
Vitadur	6.7
Pyrex	3.3

## 2.8. Merit figure for thermal shock resistance

The figure of merit for thermal shock resistance is related to the amount of heat that is applied to a given material. Thus, for example, greater the figure of merit will be when greater the heat flow or alteration of temperature that the material will endure without breaking. The parameter that measures the thermal diffusion rate is known as the Biot number ( $\beta$ ), which corresponds to one of the merit figure types of Hasselman as shown in Equation 5 [51] [52].

**Equation 5:** Biot ( $\beta$ ) number [51].

$$\text{Biot number} \left( \frac{W}{m^2 K} \right) = \beta = \frac{th}{k}$$

Where:

t= thickness of material

h= heat transfer coefficient for surface

k= thermal conductivity of material

With this parameters, a high Biot number means a slowly heat movement from a surface of the material to another. On the other hand, when heat is moved quickly through material, the Biot number will be lower [51]. When  $\beta \gg 1$ , the figure of merit for thermal shock resistance will be considered as severe, shown by Equation 6, while if  $\beta \ll 1$ , the figure of merit for thermal shock resistance will be considered moderate, shown in the Equation 7 [41][52].

**Equation 6:** Figure of merit for severe thermal shock resistance [51].

$$R = \frac{\sigma(1 - \nu)}{Y|\alpha|}$$

Where:

$\sigma$ = Rupture module

$\nu$ = Poisson coefficient

$Y$ = Young module

$|\alpha|$ = Linear coefficient of thermal expansion

**Equation 7:** Figure of merit for moderate thermal shock resistance [41] [51].

$$R' = \frac{\sigma(1 - \nu)k}{Y|\alpha|}$$

Where

$k$ = thermal conductivity of material

In both equations it can be seen that  $R$  and  $R'$  values are inversely proportional to the coefficient of linear thermal expansion and Young module, thus when near to zero is the CTE, greater the figures of merit will be [41]. However, the calculation of the Biot ( $\beta$ ) number becomes fundamental to determine which figure of merit should be used for a given application [51]. In the case of infrared windows, induction cookers as vitroceramics, and missile tips, a better equation to use is the merit for severe thermal shock resistance ( $R$ ), because these are materials exposed to high thermal shock. In table 4 some representative values for ceramics [41] [51].

Harris et al., [53] estimated the Hasselman thermal shock figures of merit for moderate and severe heating of  $Al_{0.5}Sc_{1.5}W_3O_{12}$ , which is a near zero thermal expansion material ( $\alpha_l=1.5 \times 10^{-7} K^{-1}$ ) and a good candidate for many applications as depicted in Table 4.

**Table 4-** Thermal shock resistance moderate and severe parameters for some ceramics [51].

Ceramic	R (°C)	R' (kWm <sup>-1</sup> )
Al <sub>2</sub> O <sub>3</sub>	73	2.2
ZrO <sub>2</sub>	324	0.8
SiC	206	20.6
Si <sub>3</sub> N <sub>4</sub>	495	17.3
Al <sub>0.5</sub> Sc <sub>1.5</sub> W <sub>3</sub> O <sub>12</sub>	600	80.8

## 2.9. Heat capacity (C<sub>p</sub>)

In the literature heat capacity is often described in different terms such as heat capacity at constant volume, molar heat capacity at constant volume, heat capacity at constant pressure and molar heat capacity at constant pressure. Heat capacity of solids is a function of temperature, and as the temperature increases, heat capacity increases, showing that the energy is absorbed by the body through different mechanisms. So, heat capacity is defined as the amount of heat required to change the temperature of an object by 1K. The unit of heat capacity is J/K. Heat capacity of a ceramic reaches  $3nR$  by 1000°C in which  $n$  is the number of atoms per formula unit that could affect heat capacity, for example for Cu  $C_p=3R$  and for MgO,  $C_p=6R$ , as shown in figure 10 [7]. Where heat capacity becomes constants, it is called as Debye Temperature,  $\theta_D$ , which value depends on bond strength, Young module and melting temperature.

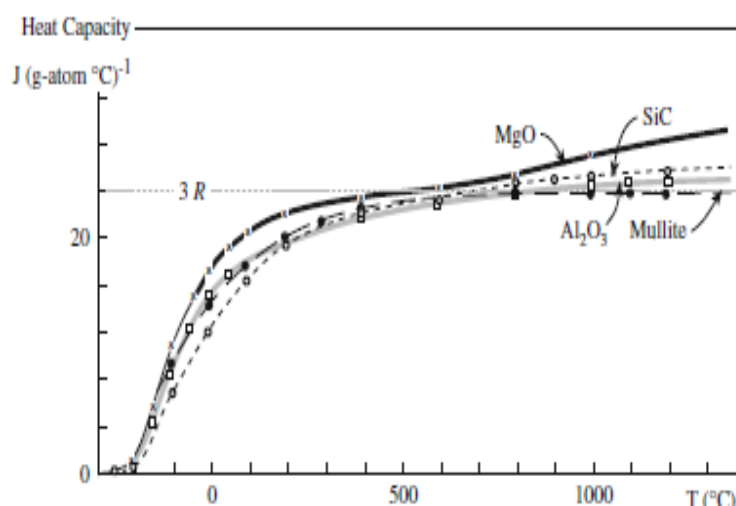


**Figure 10-** Heat capacity of MgO, SiC, Al<sub>2</sub>O<sub>3</sub> and 3Al<sub>2</sub>O<sub>3</sub>.2SiO<sub>2</sub> (mullite) as a function of temperature [7].

To calculate heat capacity at cryogenic temperatures Equation 8 is used:

**Equation 8-** Heat capacity at constant pressure and heat capacity at constant volume of ceramic materials.

$$C_p \sim C_v = K \left( \frac{T}{\theta_D} \right)^3 + \gamma T$$

Where K is a constant=1940 Jmol<sup>-1</sup>K<sup>-1</sup>, T is the temperature,  $\theta_D$  is a Debye temperature and  $\gamma$  is the electronic heat capacity coefficient [7].

## 2.10. Thermal conductivity

The ability of a material to transfer heat is known as thermal conductivity. In ceramic materials, when they are exposed to a temperature gradient, there is an increase in the number of phonons, which is why heat transfer is generated [7]. Lattice vibrations are primary source of heat transfer in ceramics, so that ceramics generally have low thermal conductivity when compared with metals [6]. Relation between heat flux and temperature gradient is given by Equation 9.

**Equation 9-** Rate of heat flow and temperature gradient for thermal conductivity [6].

$$\frac{dq}{dt} = -kA \frac{dT}{dx}$$

Where  $\frac{dq}{dt}$  is the rate of heat flow,  $\frac{dT}{dx}$  is the temperature gradient, A is the cross-sectional area normal to the direction of heat flow and k is the thermal conductivity. In order to determinate the thermal conductivity, Equation 10 is shown following:

**Equation 10-** Coefficient of thermal conductivity

$$k = \frac{C_V v_S \lambda}{3}$$

Where  $C_V$  is a heat capacity a constant volume,  $v_s$  is the velocity of propagation of elastic waves whose velocity is equal to the sound in certain solid and  $\lambda$  is the mean free path [7].

Thermomiotic materials have low thermal conductivities due to the transverse vibrations associated with NTE [18], which would decrease thermal shock resistance, therefore reducing thermal expansion. This fact could be explained by the propagation of phonons has deviations and then the half-free path decrease affecting the coefficient of thermal conductivity [54].

For a ceramic material to have a high thermal conductivity it needs to meet three conditions; very strong bonds, simple crystal structure and light elements. Related to the  $A_2M_3O_{12}$  family is known that the coefficient of thermal conductivity is low such as  $HfMgMo_3O_{12}$  [27] and  $Al_2W_3O_{12}$ [41]. In Table 5 are exposed some ceramic materials and their thermal conductivities, as shows in there all of them meet the three conditions [7].

**Table 5-** Thermal conductivity for some ceramic materials.

Material	$K(Wm^{-1}K^{-1})$
$Al_2O_3$	30.0 - 35.0
AlN	200.0 – 280.0
BeO	63.0 - 216.0
MgO	37.0
SiC	84.0 – 93.0
$SiO_2$	1.4
$TiB_2$	40.0
$Al_2W_3O_{12}$	0.63

## 2.11.

### Applications of thermomiotic materials

One of the main defects that occur with ceramic materials in the nuclear, chemical and electric power generation industries is the susceptibility of these materials to fracture when exposed to high temperatures [55]. That is why improvement of the resistance to thermal shock is mandatory for those applications.

In the manufacture of transparent infrared windows and missile tips, single crystal aluminum oxide ( $\alpha$ -  $\text{Al}_2\text{O}_3$ ) is used, better known as sapphire, which can survive extreme temperature environments [51]. The tips of the missiles are covered by a ceramic dome that protects the missile from suffering a possible rupture when it is launched into the air. In this way, this dome must have the capacity to withstand rapid aerothermal heating and resist the long-term erosion of both rain and dust [51]. An infrared window is one that allows separating two different environments considering pressures and temperatures permitting that the energy at a specific electromagnetic wavelength pass between the two environments [1].

At the level of the kitchen industry, several accidents have occurred due to the susceptibility that glass has to the fracture, for example when this material has been removed from an oven and comes into contact with cold water, there will be an abrupt decrease in the temperature that creates a temperature gradient, and thus the tensile stresses are generated causing propagation of microcracks. Taking into account the weakness of these materials, the necessity to synthesize novel materials were proposed, as in the case of induction cookers, which are supported on a surface of glass-ceramic material and which principal function is heat just the bottom of a pot, making food cook faster. In this way in a normal operation of the induction cooker, it will remain cold enough to touch it and thus reduce the number of accidents generated in the kitchen [56] [57].

In the vitreous industry there are a number of materials that can withstand the exposure to high temperatures without suffering any damage. These materials can be glass ceramics that are formed by heating this material until it begins to crystallize [58]. Thus, the so-called glass-ceramic materials, which contain crystalline grains embedded in the residual glass matrix. One of the most important glass ceramics is *Zerodur*, basically a material which composition is 78%  $\text{SiO}_2$  and whose coefficient of thermal expansion is very close to zero  $\alpha_1 = 0.05 \times 10^{-6} \text{ K}^{-1}$  between 20 °C and 300 °C.

### 3 Objectives

#### 3.1. General Objective

Synthesis and characterization of two new  $\text{ZrMgMo}_3\text{O}_{12}$ -based systems by adding  $\text{Zn}^{2+}$  and  $\text{Ni}^{2+}$ .

#### 3.2. Specific objectives

Determination of the solubility limits of  $\text{Zn}^{2+}$  and  $\text{Ni}^{2+}$  in  $\text{ZrMg}_{1-x}\text{Zn}_x\text{Mo}_3\text{O}_{12}$  and  $\text{ZrMg}_{1-x}\text{Ni}_x\text{Mo}_3\text{O}_{12}$  system, respectively.

Determination of the composition that presents the lowest linear thermal expansion coefficient.

Evaluation of the parameters of technological importance such as phase transition temperature (monoclinic for orthorhombic), hygroscopicity and band gap energy in the  $\text{ZrMg}_{1-x}\text{Zn}_x\text{Mo}_3\text{O}_{12}$  and  $\text{ZrMg}_{1-x}\text{Ni}_x\text{Mo}_3\text{O}_{12}$  system.

## 4 Materials and methods

### 4.1. Solid state reaction

The solid-state reaction method was carried out to assure good effective contacts between the particles of stoichiometric mixtures of starting oxides in order to promote obtaining of a chemically homogeneous powder.

#### 4.1.1. Synthesis of $\text{ZrMg}_{1-x}(\text{Zn/Ni})_x\text{Mo}_3\text{O}_{12}$ systems by solid state reaction

Solid-state reaction was carried out by mixing ZnO (Sigma Aldrich, 97%), MgO (Sigma Aldrich, 97%), MoO<sub>3</sub> (Fluka, 98%), NiO (ZRM - RS 5, 99%) and ZrO<sub>2</sub> (Sigma Aldrich, 99%). All the reagents were subjected to pre-heating at 500 °C for 1h. They were weighed in the respective stoichiometric quantities and a total of 2 g was used for each synthesis. Afterwards, the starting reagents were mixed in a mortar making circular movements for approximately 2h. Solid green bodies were obtained in a hydraulic press with a pressure of 98 MPa $\text{min}^{-1}$ , obtaining cylindrical test bodies of 2.75 mm thick and 6 mm long. For the  $\text{ZrMg}_{1-x}\text{Zn}_x\text{Mo}_3\text{O}_{12}$  system, the samples were calcined at 1073 K for 5 hours, while for the  $\text{ZrMg}_{1-x}\text{Ni}_x\text{Mo}_3\text{O}_{12}$  system the samples were calcined at 1073 K for 10 hours. The compositions  $x=0.1$ ,  $x=0.3$ ,  $x=0.35$ ,  $x=0.4$ ,  $x=1$  for  $\text{ZrMg}_{1-x}\text{Zn}_x\text{Mo}_3\text{O}_{12}$  and  $x=0.05$ ,  $x=0.1$ ,  $x=0.15$ ,  $x=0.2$ ,  $x=1$  for  $\text{ZrMg}_{1-x}\text{Ni}_x\text{Mo}_3\text{O}_{12}$  were considered. Figure 11 exhibits a diagram summarizing the methodology used for the synthesis of  $\text{ZrMg}_{1-x}(\text{Zn/Ni})_x\text{Mo}_3\text{O}_{12}$  system.

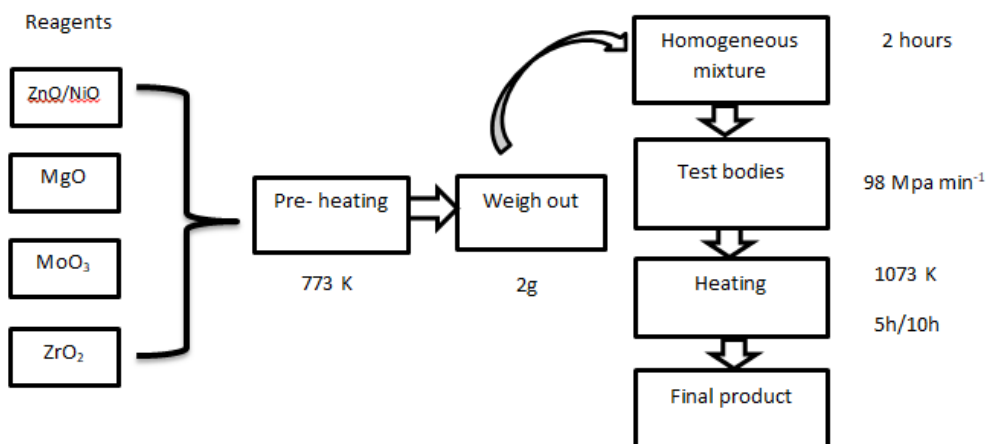


**Figure 11-** Schematic representation of the synthesis of  $\text{ZrMg}_{1-x}(\text{Zn/Ni})_x\text{Mo}_3\text{O}_{12}$  system by solid state reaction.

## 4.2. Characterization of $\text{ZrMg}_{1-x}(\text{Zn/Ni})_x\text{Mo}_3\text{O}_{12}$ systems

### 4.2.1. X-ray powder diffraction (XRPD)

The calcined  $\text{ZrMg}_{1-x}\text{Zn}_x\text{Mo}_3\text{O}_{12}$  and  $\text{ZrMg}_{1-x}\text{Ni}_x\text{Mo}_3\text{O}_{12}$  powders were analyzed by X-ray powder diffraction (XRPD) at room temperature in a D8 Discover X-ray diffractometer (Bruker, Karlsruhe, Germany), using  $\text{CuK}\alpha$  radiation of 40kV e 40mA in steps of  $0.02^\circ$  (2 s per step) over a range of  $10\text{--}60^\circ 2\theta$ . A zero-background sample holder was used. This analysis was carried out to identify phase composition of  $\text{ZrMg}_{1-x}\text{Zn}_x\text{Mo}_3\text{O}_{12}$  and  $\text{ZrMg}_{1-x}\text{Ni}_x\text{Mo}_3\text{O}_{12}$  systems. The diffractograms were analyzed using TOPAS 4.2 program and LeBail method.

### 4.2.2. High temperature X-ray powder diffraction

The calcined  $\text{ZrMg}_{1-x}\text{Zn}_x\text{Mo}_3\text{O}_{12}$  and  $\text{ZrMg}_{1-x}\text{Ni}_x\text{Mo}_3\text{O}_{12}$  powders were analyzed by X-ray powder diffraction (*in situ*-XRPD) in a D8 Advance X-ray diffractometer (Bruker, Karlsruhe, Germany), equipped with a reactive XRK900 camera (Anton Paar GmbH, Graz, Austria).  $\text{CuK}\alpha$  radiation of 40kV e 40mA has been used and the diffraction intensities have been collected in the steps of  $0.01^\circ$

(2.5 s per step) over a range of  $10\text{--}60^\circ 2\theta$ . The samples were analyzed at the following temperatures 373, 573, 773 and 973 K. Samples were heated at a rate of  $12\text{ }^\circ\text{Cmin}^{-1}$ . The diffractograms were also analyzed using TOPAS 4.2 software to investigate the phase composition and also to evaluate unit cells variation with the temperature and afterwards to calculate the intrinsic coefficient of thermal expansion (CTE) for the phases of the  $\text{ZrMg}_{1-x}\text{Zn}_x\text{Mo}_3\text{O}_{12}$  and  $\text{ZrMg}_{1-x}\text{Ni}_x\text{Mo}_3\text{O}_{12}$  systems.

### 4.2.3. Low temperature X-ray powder diffraction

The calcined  $\text{ZrMg}_{1-x}\text{Zn}_x\text{Mo}_3\text{O}_{12}$  and  $\text{ZrMg}_{1-x}\text{Ni}_x\text{Mo}_3\text{O}_{12}$  powders were analyzed by X-ray powder diffraction (XRPD-in situ) in a X'Pert PRO (Philips, Panalytical), using a PW 3373/00 Cu LFF DK 184754r radiation of 40 kV e 40 mA . The diffraction intensities have been acquired in steps of  $0.01^\circ$  (2s per step) over a range of  $10\text{--}60^\circ 2\theta$ . The samples were analyzed at different temperatures such as 298, 253, 213 and 173 K. Samples were cooled at a rate of  $10\text{ }^\circ\text{C min}^{-1}$ . The diffractograms were also analyzed using TOPAS 4.2 software to investigate the phase composition, unit-cell variations and possible phase transformations. The data was refined using the Le Bail method to determine the intrinsic CTE and phase transitions.

### 4.2.4. Thermogravimetry (TGA)

Both systems were analyzed in a Perkin-Elmer Simultaneous Thermal Analyzer STA-6000 (Seer Green, U.K.) in order to evaluate hygroscopicity, which is represented by the mass loss of the sample in temperature range above room temperature, but lower than  $150^\circ\text{C}$ . 10 mg for each sample were used for each analysis. The conditions of analysis were following:

- Atmosphere: Synthetic air
- Gas flow:  $20\text{mLmin}^{-1}$
- Temperature profile:
  - Initial temperature: 303 K
  - Heating rate:  $20\text{ }^\circ\text{Cmin}^{-1}$

- Final temperature: 873 K

#### 4.2.5. Differential Scanning Calorimetry (DSC)

Thermal Analysis was used for the identification of the phase transition temperature below the room temperature. The samples of 13.6 mg each were introduced in an aluminum pan. A TA Instruments Q200 differential scanning calorimeter equipped with a liquid N<sub>2</sub> cooling head was used for DSC measurements. The temperature range studied was between 98 and 573 K with a cooling/heating rate of 20 °Cmin<sup>-1</sup>. Measurements were performed under Helium purge gas at 25 mLmin<sup>-1</sup>. Three heating/cooling steps were performed: the first one was cooling from room temperature to 98K (first cooling stage), the second step was heating from the range of 98 to 573K (heating stage) and final step was a second cooling from 573 to 98K.

#### 4.2.6. Diffuse Reflectance Spectroscopy (DRS)

In order to determine the band-gap energy of the phases within the ZrMg<sub>1-x</sub>Zn<sub>x</sub>Mo<sub>3</sub>O<sub>12</sub> and ZrMg<sub>1-x</sub>Ni<sub>x</sub>Mo<sub>3</sub>O<sub>12</sub> systems, a spectrometer Perkin-Elmer Lambda 900 was used and  $\alpha$ -Al<sub>2</sub>O<sub>3</sub> as reflectance reference was applied. Samples were analyzed in powder form at room temperature. The measurement range for reflectance was between 200 and 800 nm. Assumed an indirect transition for the fundamental absorption, the apparent band-gap energies were obtained by Kubelka-Munk function, plotting  $(F(R)h\nu)^{1/2}$  as a function of excitation energy against  $h\nu$  (photon energy) and extrapolating the straight- line portion of the UV-Vis spectra to  $(F(R)h\nu)^{1/2} = 0$ .

#### 4.2.7. Raman Spectroscopy

The Raman spectra were collected in retro-scattering geometry, through a microscope connected to a triple grid spectrometer (Jobin Yvon T64000 Horiba brand), equipped with a CCD detector (charge-coupled device) and cooled by Peltier effect. The samples were excited by a laser line 532 nm, and the

spectrometer slits were defined for a resolution of  $2 \text{ cm}^{-1}$ . An Olympus objective microscope lens with a magnification of 20X and a focal length of 19 mm and a numerical aperture of 0.35 was used. Using the relation  $(\varphi) = 1.22 \times \lambda / \text{AN}$ ; where AN is the numerical aperture of the lens objective, and  $\lambda$  is the wavelength of the radiation, the diameter of the laser spot was estimated at  $1.8 \text{ }\mu\text{m}$ . The spectra were taken using two accumulations of 10s in each spectral region. For each sample 5 scanning points were probed in order to evaluate chemical homogeneity of the materials.

## 5 Results and discussions

### 5.1. Phase composition

XRPD patterns of  $\text{ZrMgMo}_3\text{O}_{12}$  (Figure 12) suggested that the principal phases within the  $\text{ZrMg}_{1-x}\text{Zn}_x\text{Mo}_3\text{O}_{12}$  and  $\text{ZrMg}_{1-x}\text{Ni}_x\text{Mo}_3\text{O}_{12}$  systems may crystallize in orthorhombic crystal system in  $Pna2_1$  space group. Some authors have reported that many phases within  $\text{A}_2\text{M}_3\text{O}_{12}$  family are orthorhombic at room temperature such as  $\text{Sc}_2\text{Mo}_3\text{O}_{12}$ ,  $\text{Al}_2\text{W}_3\text{O}_{12}$  [46]  $\text{HfMgMo}_3\text{O}_{12}$  [27]. This is different from some other phases for this family which adopted monoclinic structure at room temperature, such  $\text{Fe}_2\text{Mo}_3\text{O}_{12}$ ,  $\text{Cr}_2\text{Mo}_3\text{O}_{12}$  and  $\text{Al}_2\text{Mo}_3\text{O}_{12}$  [30].

Originally  $\text{HfMgW}_3\text{O}_{12}$ , a similar phase from the same subfamily, [58] has been reported to adopt orthorhombic symmetry with space group  $Pnma$  at room temperature. However, a few years later  $\text{HfMgMo}_3\text{O}_{12}$  [26] was synthesized and a space group  $Pna2_1$  has been determined as the correct one for the phases of this subfamily. Figure 12 indicates that  $\text{ZrMgMo}_3\text{O}_{12}$  phase was synthesized successfully as an orthorhombic crystalline structure with  $Pna2_1$  space group at room temperature. Nevertheless a small amount of  $\text{ZrMo}_2\text{O}_8$  was confirmed by LeBail as a trigonal structure.

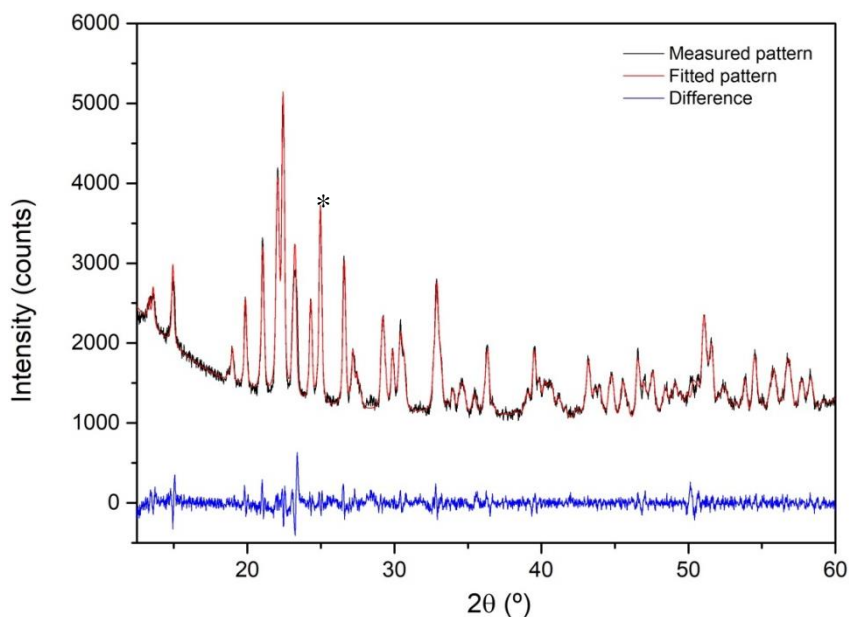


**Figure 12-** Diffraction pattern of  $\text{ZrMgMo}_3\text{O}_{12}$  adjusted by Le Bail method. (\*) trigonal  $\text{ZrMo}_2\text{O}_8$ .

According to Song et al., [59]  $\text{ZrMgMo}_3\text{O}_{12}$ , adopts an orthorhombic structure with space group  $Pnma$  or  $Pna2_1$ . Nevertheless, Romao et al., [59] solved that  $\text{ZrMgMo}_3\text{O}_{12}$  crystallized in  $Pna2_1$  space group.

For  $\text{ZrMg}_{1-x}\text{Zn}_x\text{Mo}_3\text{O}_{12}$  system the desired orthorhombic phase was successfully formed and it is stable at room temperature. The quality of LeBail adjustment for  $\text{ZrMg}_{1-x}\text{Zn}_x\text{Mo}_3\text{O}_{12}$  system, given by  $R_{wp}$  and GoF, are listed in Table 6.

**Table 6-** Le Bail adjustment for  $\text{ZrMgMo}_3\text{O}_{12}$  and  $\text{ZrMg}_{1-x}\text{Zn}_x\text{Mo}_3\text{O}_{12}$  system.

System	$R_{wp}$	GoF
$\text{ZrMgMo}_3\text{O}_{12}$	4.05	1.70
$\text{ZrMg}_{0.9}\text{Zn}_{0.1}\text{Mo}_3\text{O}_{12}$	2.70	1.59
$\text{ZrMg}_{0.7}\text{Zn}_{0.3}\text{Mo}_3\text{O}_{12}$	3.39	1.87
$\text{ZrMg}_{0.65}\text{Zn}_{0.35}\text{Mo}_3\text{O}_{12}$	2.96	1.72
$\text{ZrMg}_{0.6}\text{Zn}_{0.4}\text{Mo}_3\text{O}_{12}$	3.36	1.83

It was determined that at room temperature the main-phases of the systems  $\text{ZrMg}_{1-x}\text{Zn}_x\text{Mo}_3\text{O}_{12}$  and  $\text{ZrMg}_{1-x}\text{Ni}_x\text{Mo}_3\text{O}_{12}$  (Figure 13a,b) adopted at room temperature orthorhombic crystal system within the space group  $Pna2_1$ , therefore, keeping the same space group as that of the mother phase  $\text{ZrMgMo}_3\text{O}_{12}$ . [8].

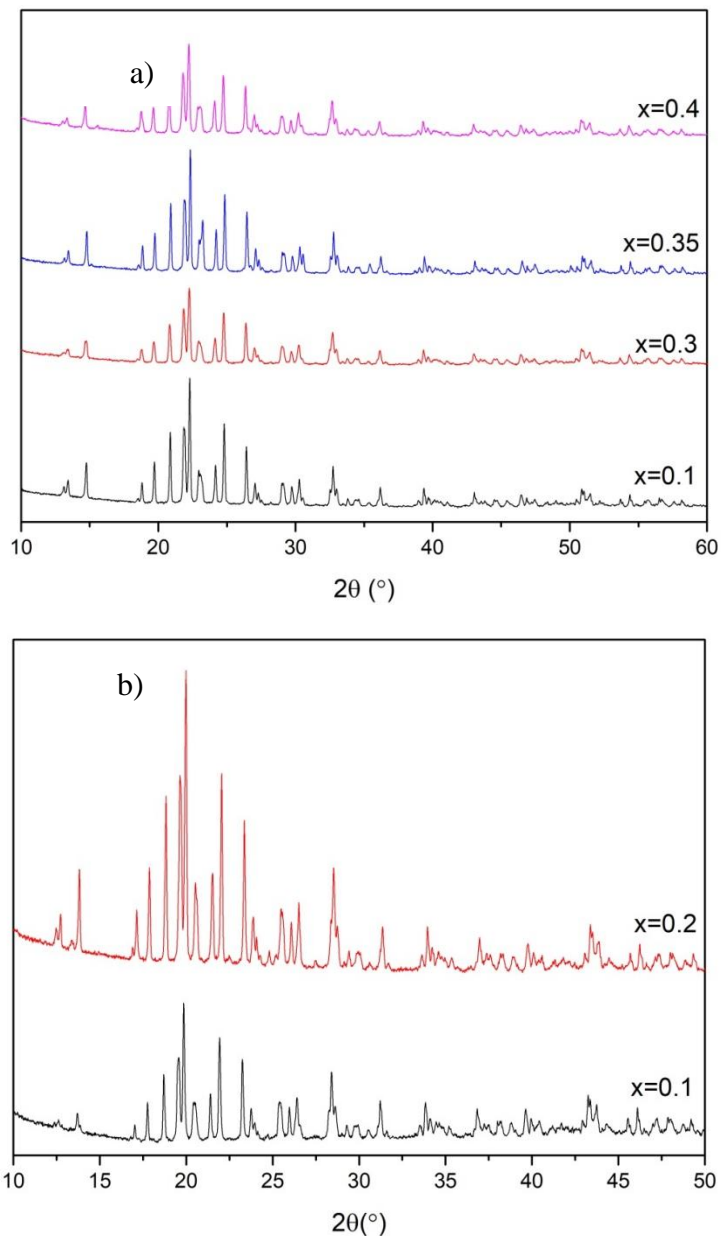


**Figure 13-** Diffraction patterns of a)  $\text{ZrMg}_{1-x}\text{Zn}_x\text{Mo}_3\text{O}_{12}$  and b)  $\text{ZrMg}_{1-x}\text{Ni}_x\text{Mo}_3\text{O}_{12}$ .

The two peaks, marked in Figure 14, at  $21.8^\circ$  and  $22.2^\circ$  ( $2\theta$ ) are typically associated with the symmetry of the orthorhombic  $Pna2_1$  space group of the  $\text{A}_2\text{M}_3\text{O}_{12}$  family [26].

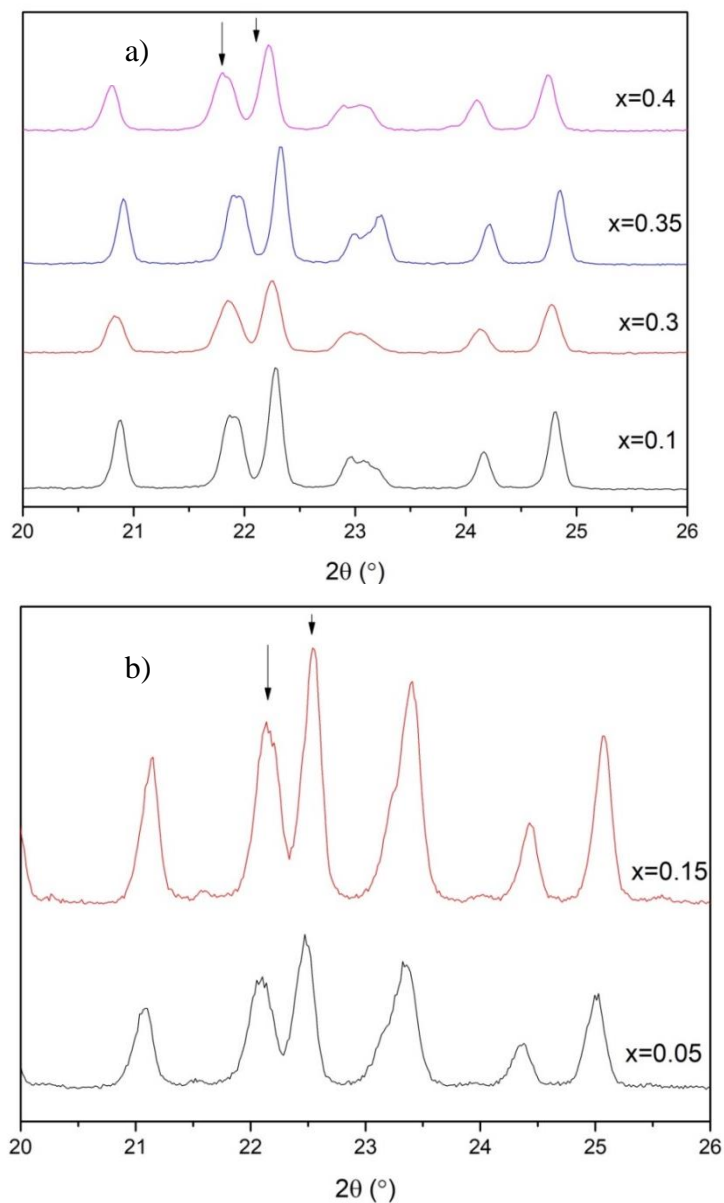


**Figure 14**-X-ray diffraction patterns for a)  $\text{ZrMg}_{1-x}\text{Zn}_x\text{Mo}_3\text{O}_{12}$  phases and b)  $\text{ZrMg}_{1-x}\text{Ni}_x\text{Mo}_3\text{O}_{12}$  phases, showing the characteristic peaks of orthorhombic crystal system for the  $\text{ABM}_3\text{O}_{12}$  subfamily.

With the purpose of evaluate a possible total substitution of  $\text{Zn}^{2+}$  and  $\text{Ni}^{2+}$  by  $\text{Mg}^{2+}$  within  $\text{ZrMgMo}_3\text{O}_{12}$ , XRPD was applied. In the case of  $\text{ZrZnMo}_3\text{O}_{12}$  two phases have been formed corresponding to  $\text{ZrMo}_2\text{O}_8$ , trigonal structure, P-31c space group and  $\text{ZnMoO}_4$ , monoclinic structure, C2/m space group. For  $\text{ZrNiMo}_3\text{O}_{12}$  two phases have been formed, as well. The one was  $\text{ZrMo}_2\text{O}_8$  with trigonal structure, P-31c space group and the second was  $\text{NiMoO}_4$  monoclinic structure, C2/m space group. Diffraction patterns for both systems, together with

LeBail fits, are shown in Figure 15. These findings suggested that these two phases may not be thermodynamically stable.

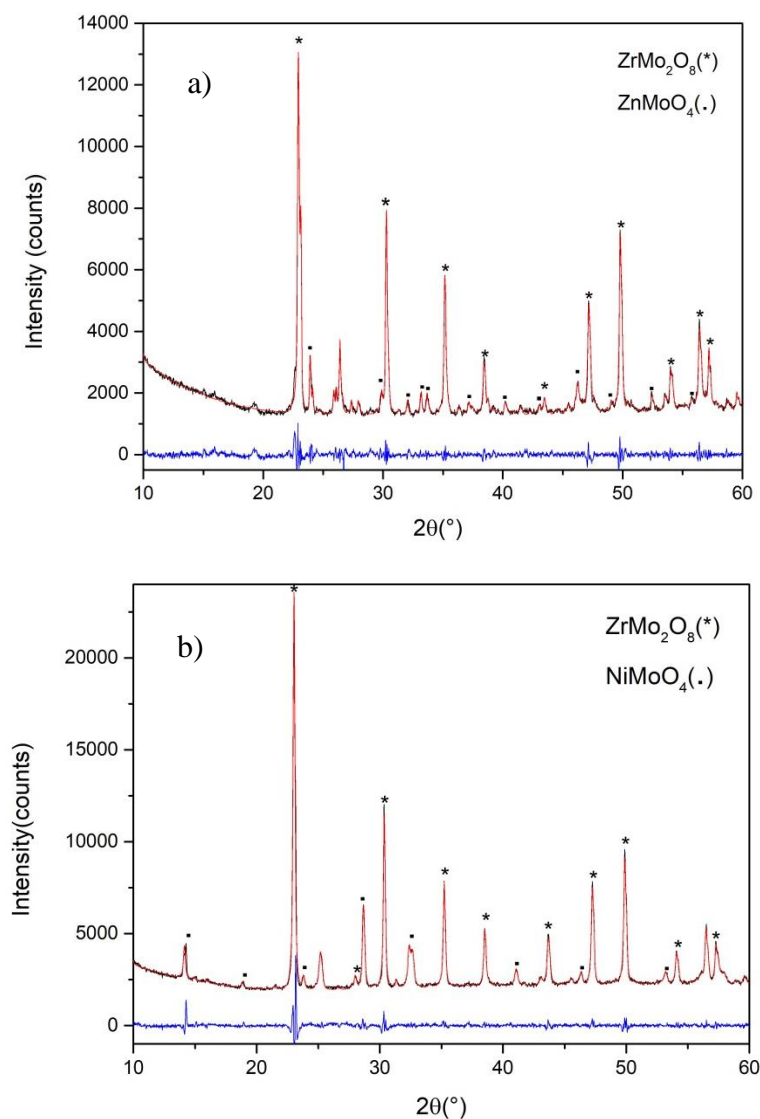


**Figure 15-** Diffraction pattern for a)  $\text{ZrZnMo}_3\text{O}_{12}$  composition with two phases (\*) trigonal  $\text{ZrMo}_2\text{O}_8$  and (.) monoclinic  $\text{ZnMoO}_4$  and for b)  $\text{ZrNiMo}_3\text{O}_{12}$  composition with two phases (\*)trigonal  $\text{ZrMo}_2\text{O}_8$  and (.) monoclinic  $\text{NiMoO}_4$ .

## 5.2.

### Determination of the solubility limit of $\text{Zn}^{2+}$ and $\text{Ni}^{2+}$ in $\text{ZrMg}_{1-x}(\text{Zn/Ni})_x\text{Mo}_3\text{O}_{12}$ systems

In order to determine the  $\text{Zn}^{2+}$  and  $\text{Ni}^{2+}$  solubility in  $\text{ZrMg}_{1-x}(\text{Zn/Ni})_x\text{Mo}_3\text{O}_{12}$  systems and to analyze the formed structures, compositions were characterized by

the technique of X-Ray Diffraction and their diffractograms adjusted by the LeBail method.

Beside the expected orthorhombic phase, presented at room temperature for all compositions, a secondary phase,  $\text{ZrMo}_2\text{O}_8$  (PDF: 77-1784) appeared in the  $\text{ZrMg}_{1-x}\text{Zn}_x\text{Mo}_3\text{O}_{12}$  system for compositions from  $x=0.1$  to  $x=0.4$ , and corresponds to trigonal space group P-31c, as shown in Figure 16, identified through the X-ray diffraction line at  $23^\circ$ - $2\theta$ . According to Allen et al., [59] and Sahoo et al., [60] there are two peaks, around  $23^\circ$  and  $30^\circ$   $2\theta$ , identified as  $\text{ZrMo}_2\text{O}_8$  peaks. In this work the peak around  $23^\circ$   $2\theta$  is perfectly clear in all compositions as shown in Figure 16. It is different, therefore, from  $\text{ZrMgMo}_3\text{O}_{12}$  phase [58] where no secondary phase has been found.

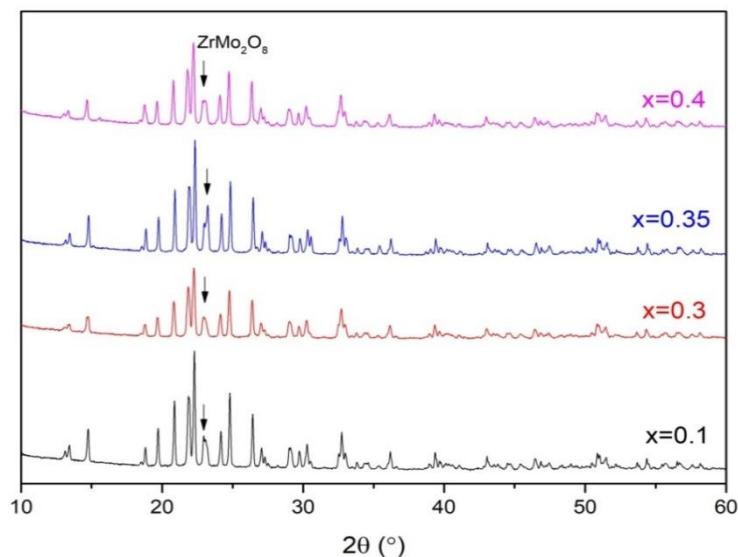
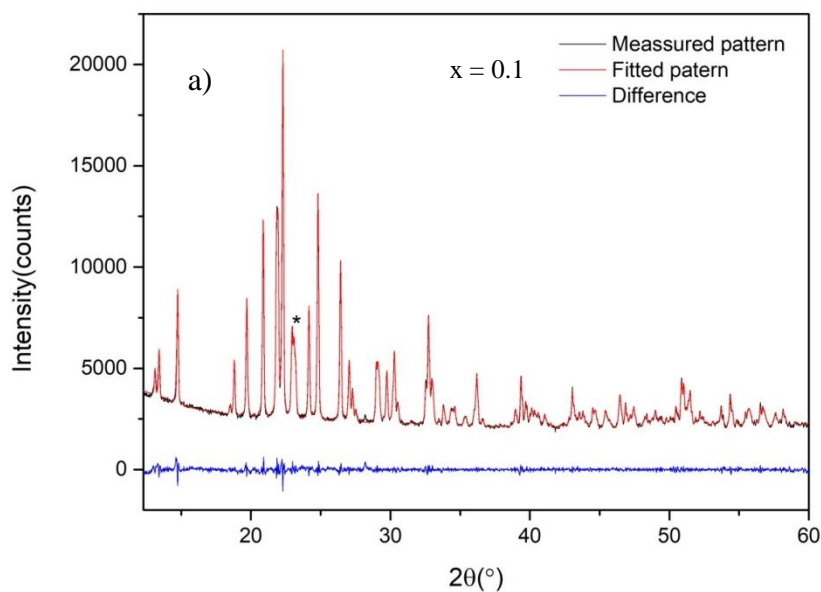


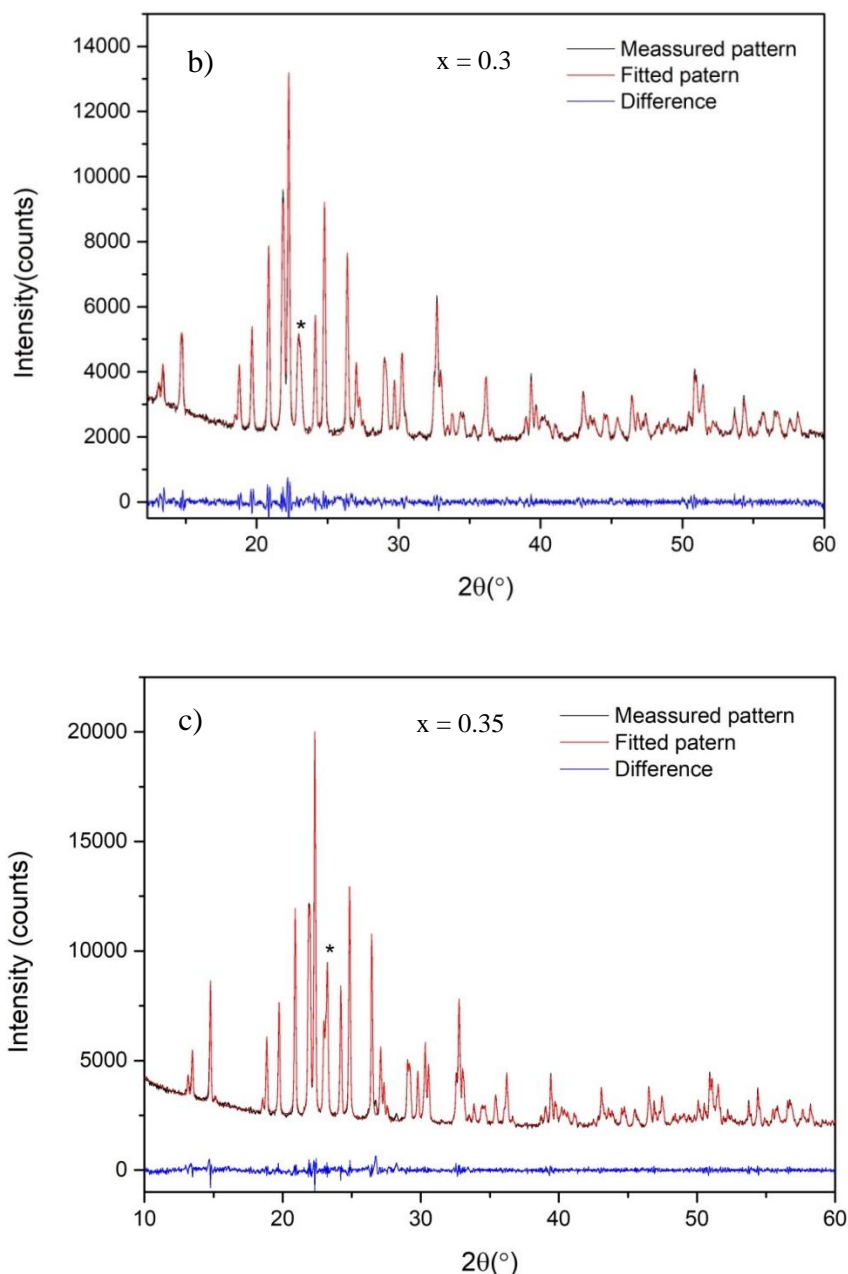
**Figure 16-** X-ray diffraction patterns of the composition  $x=0.1$ ;  $0.3$ ;  $0.35$  and  $0.4$  of the  $\text{ZrMg}_{1-x}\text{Zn}_x\text{Mo}_3\text{O}_{12}$  system in the range from  $10^\circ$  to  $60^\circ$  ( $2\theta$ ) with  $\text{ZrMo}_2\text{O}_8$  as a second phase. The arrow is marking the position of  $\text{ZrMo}_2\text{O}_8$  diffraction line.

The  $\text{ZrMo}_2\text{O}_8$  phase was already reported in the NTE  $\text{AM}_2\text{O}_8$  family by Mittal et al., [60]. Also several different polymorphs of the  $\text{ZrMo}_2\text{O}_8$  phase were reported, some stable at low and others at high temperatures. For example, the trigonal phase  $\alpha$ -  $\text{ZrMo}_2\text{O}_8$  studied by Auray et al., [61] [62] and  $\beta$ -  $\text{ZrMo}_2\text{O}_8$  monoclinic phase studied by Sahoo et al.,[63]. However, Lind et al [64] reported another polymorph, the cubic  $\gamma$ - $\text{ZrMo}_2\text{O}_8$  phase which demonstrates NTE, and transforms to trigonal phase  $\alpha$   $\text{ZrMo}_2\text{O}_8$  at 663K.

The formation of the  $\text{ZrMo}_2\text{O}_8$  phase can be attributed to the lack of homogeneity during the reagent mixing process, since this process is carried out manually and not in a ball mill as recommended for solid-state reaction. Therefore, the probability of obtaining a single phase is lower than in some soft-chemistry methods. Figure 17 displayed the characteristic peak of the  $\text{ZrMo}_2\text{O}_8$  phase, which is evident for all compositions in the  $\text{ZrMg}_{1-x}\text{Zn}_x\text{Mo}_3\text{O}_{12}$  system, from  $x=0.1$  to  $x=0.35$ . It is relevant to observe that the adjustment of the experimental patterns, showed in Figure 17, have been performed by LeBail method and that beside  $\text{ZrMg}_{1-x}\text{Zn}_x\text{Mo}_3\text{O}_{12}$ -type phase, trigonal  $\text{ZrMo}_2\text{O}_8$  phase has been considered in all diffratograms for the purpose of adjustment.

$\text{ZrMgMo}_3\text{O}_{12}$  phase has been studied recently by Yang et al., [65], in which the  $\text{ZrMo}_2\text{O}_8$  is present as a secondary phase after synthesis at 925K, while other secondary phases, such as  $\text{MgMoO}_4$  and  $\text{ZrO}_2$  were found at higher temperatures. In our work only  $\text{ZrMo}_2\text{O}_8$  was identified after the synthesis at 1073K.

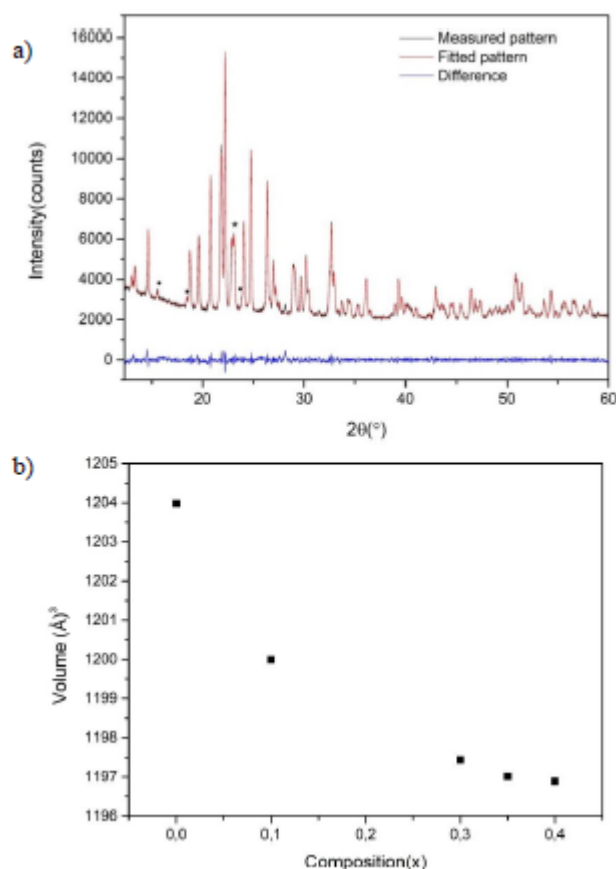




**Figure 17-** X-ray diffraction patterns adjusted by the Le Bail method of the compositions: a)  $\text{ZrMg}_{0.9}\text{Zn}_{0.1}\text{Mo}_3\text{O}_{12}$  b)  $\text{ZrMg}_{0.7}\text{Zn}_{0.3}\text{Mo}_3\text{O}_{12}$  and c)  $\text{ZrMg}_{0.65}\text{Zn}_{0.35}\text{Mo}_3\text{O}_{12}$ . (\*) Peak associated with the space group  $P\bar{3}_1c$  of trigonal  $\text{ZrMo}_2\text{O}_8$ .

For composition  $x = 0.4$ , monoclinic  $\text{ZnMoO}_4$  phase with the  $C2/m$  space group has been identified as well (PDF: 01-084-6506), Figure 18. Cavalcante et al., [66] studied  $\text{ZnMoO}_4$  phase and characteristic peaks around  $15^\circ$ ,  $18^\circ$ ,  $25^\circ$  and  $30^\circ$  ( $2\theta$ ) have been attributed to this phase. In our work the peaks at around  $15.63^\circ$ ,  $18.49^\circ$  and  $24^\circ$  ( $2\theta$ ) have been identified and attributed to  $\text{ZnMoO}_4$ . Therefore, this finding suggested that the solubility limit of  $\text{Zn}^{2+}$  in the  $\text{ZrMg}_{1-x}\text{Zn}_x\text{Mo}_3\text{O}_{12}$  is between  $0.35 \leq x \leq 0.4$ . It is worth noting that the diffraction

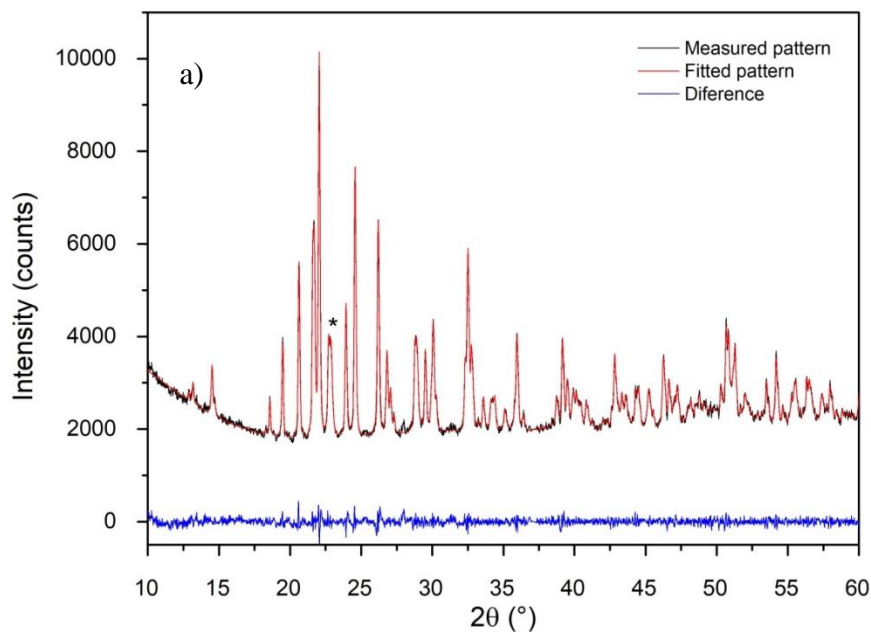
pattern of the composition  $x=0.4$  (Figure 18a) was adjusted by Le Bail method considering three different phases such as  $\text{ZrMg}_{1-x}\text{Zn}_x\text{Mo}_3\text{O}_{12}$ -based phase,  $\text{ZrMoO}_4$  and  $\text{ZnMoO}_4$ . Li et al., [48] have reported for the  $\text{HfMg}_{1-x}\text{Zn}_x\text{Mo}_3\text{O}_{12}$  system that the solubility limit of  $\text{Zn}^{2+}$  is  $x \leq 0.5$ , close to the one reported for  $\text{ZrMg}_{1-x}\text{Zn}_x\text{Mo}_3\text{O}_{12}$ . The same authors reported that for compositions above this value additional phases are formed such as  $\text{HfMo}_2\text{O}_8$  as a trigonal structure [67] and  $\text{ZnMoO}_4$  as a monoclinic structure [60]. Another fact that indicates the solubility limit can be analyzed by the change produced in the volume of the unit cell, as seen in Figure 18b. The value of the volume remains almost constant in a range of  $x=0.35-0.4$ , indicating a solubility limit of  $\text{Zn}^{2+}$  within  $\text{ZrMgMo}_3\text{O}_{12}$  system.



**Figure 18-** a) X-ray diffraction pattern adjusted by the Le Bail method of the compositions  $\text{ZrMg}_{0.6}\text{Zn}_{0.4}\text{Mo}_3\text{O}_{12}$  (\*) Peaks associated with the trigonal space group  $P\bar{3}_1c$  of  $\text{ZrMo}_2\text{O}_8$  phase. (o) Peaks associated with the monoclinic space group  $C2/m$ , of  $\text{ZnMoO}_4$ . b) Volume of unit cell as a function of composition of  $\text{Zn}^{2+}$ .

For the  $\text{ZrMg}_{1-x}\text{Ni}_x\text{Mo}_3\text{O}_{12}$  system XRPD indicated also the formation of the desired orthorhombic phases for all tested compositions (Figure 19a,b). Nevertheless, small amounts of  $\text{ZrMo}_2\text{O}_8$  phase was found in all samples (Figure 19 a). It corresponds to a trigonal crystalline structure and space group P-31c. This phase is formed due to the same reasons already mentioned for the  $\text{ZrMg}_{1-x}\text{Zn}_x\text{Mo}_3\text{O}_{12}$  system.

For  $\text{ZrMg}_{0.8}\text{Ni}_{0.2}\text{Mo}_3\text{O}_{12}$  peaks as ( $13.4^\circ$ ,  $25.3^\circ$ ,  $28.16^\circ$ , and  $28.7^\circ - 20$ ) are identified for monoclinic  $\text{NiMoO}_4$  phase, space group C2/m (Figure 19 b). According to Zavoianu et al., [68] and Mazzocchia et al., [69] characteristic peaks for  $\text{NiMoO}_4$  as a monoclinic structure were obtained at  $2\theta=14^\circ$ ,  $23^\circ$ ,  $28^\circ$  and  $38^\circ$ , being the most intensity peak at  $28^\circ$  as same of this work. Therefore, these results suggested that the solubility limit of  $\text{Ni}^{2+}$  in the  $\text{ZrMg}_{1-x}\text{Ni}_x\text{Mo}_3\text{O}_{12}$  is between  $0.1 \leq x \leq 0.2$ .



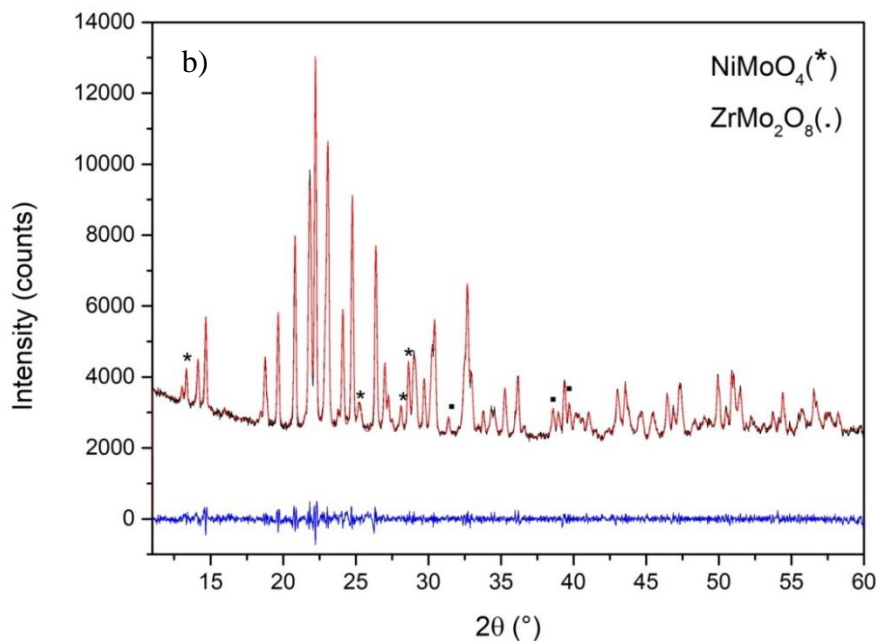


**Figure 19-** a) X-ray diffraction pattern adjusted by the LeBail method for  $\text{ZrMg}_{0.9}\text{Ni}_{0.1}\text{Mo}_3\text{O}_{12}$ . and b)  $\text{ZrMg}_{0.8}\text{Ni}_{0.2}\text{Mo}_3\text{O}_{12}$ . (.) Peaks associated with the hexagonal space group  $P-3_1c$  of  $\text{ZrMo}_2\text{O}_8$  phase. (\*) Peaks associated with the monoclinic space group  $C2/m$ , of  $\text{NiMoO}_4$ .

### 5.3. Phase transition temperature

#### 5.3.1. Phase transition temperature by XRPD

One characteristic of XRPD patterns of orthorhombic phases in  $\text{A}_2\text{M}_3\text{O}_{12}$  family are two strong peaks close to  $22^\circ$  ( $2\theta$ ) [70]. As reported by Li et al [48] for the  $\text{HfMg}_{0.7}\text{Zn}_{0.3}\text{Mo}_3\text{O}_{12}$  phase based on XRPD it was found that this phase presents a phase transition at around 225K, to lower temperature monoclinic phase.

In our study it was found that diffraction patterns for  $\text{ZrMgMo}_3\text{O}_{12}$  was almost identical at the evaluating temperatures (173-298) K, as shown in Figure 20a. Thus it can be concluded that there is no phase transition at this temperature range. In the other hand, changes in diffraction patterns were presented for the  $\text{ZrMg}_{1-x}\text{Zn}_x\text{Mo}_3\text{O}_{12}$  system which transforms for monoclinic to orthorhombic

structure in this temperature range. For  $x=0.10$  (Figure 20b), the transition temperature is not well defined by XRPD since at 173 K the system was close to the phase transition temperature and possibly there is the coexistence of both orthorhombic and monoclinic phases. For  $x=0.3$  (Figure 20c) the transition temperature is situated between 213 and 253 K, while in the case of  $x=0.35$  (Figure 20d) it is within 253 and 298 K.

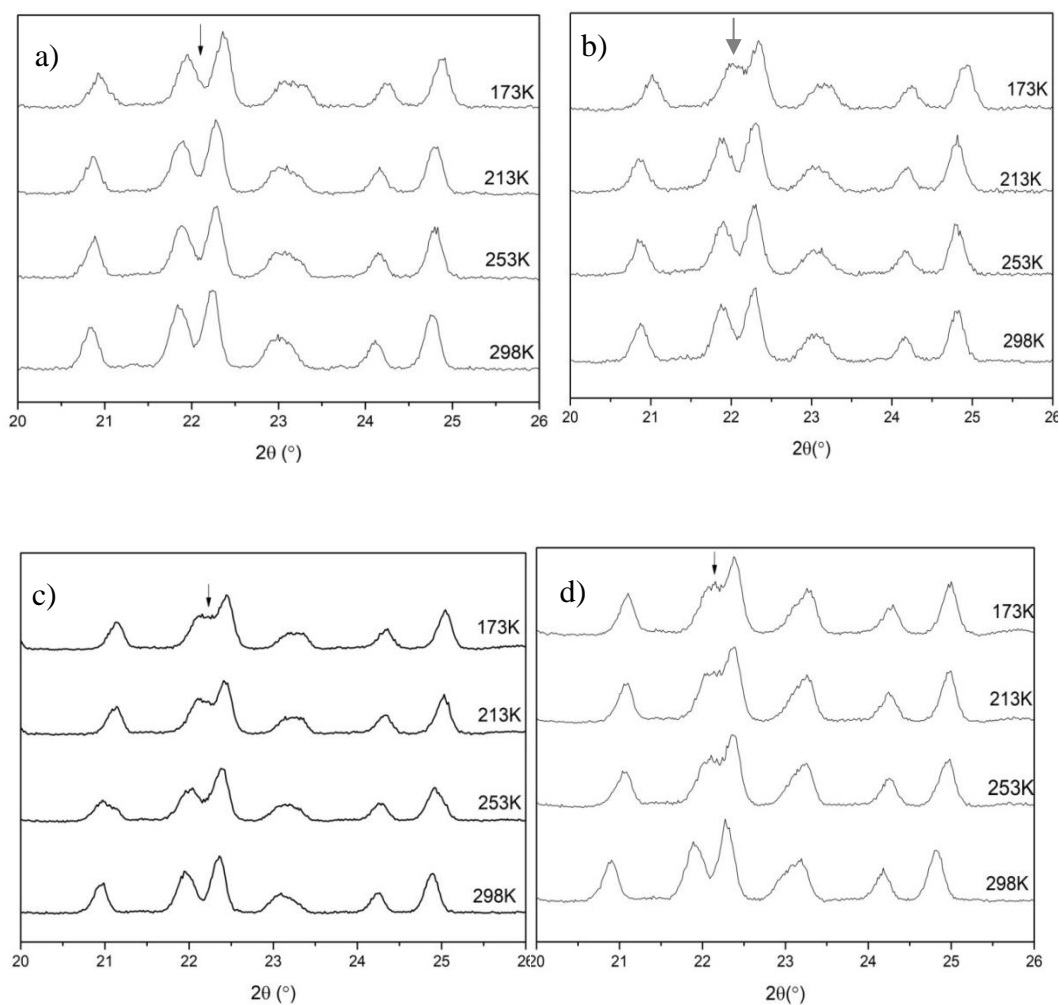


**Figure 20-** Diffraction pattern lines for a)  $\text{ZrMgMo}_3\text{O}_{12}$ , b)  $\text{ZrMg}_{0.9}\text{Zn}_{0.1}\text{Mo}_3\text{O}_{12}$ , c)  $\text{ZrMg}_{0.7}\text{Zn}_{0.3}\text{Mo}_3\text{O}_{12}$  and d)  $\text{ZrMg}_{0.65}\text{Zn}_{0.35}\text{Mo}_3\text{O}_{12}$ . (↓) Characteristic pick which corresponds to the transition of monoclinic to orthorhombic structure by the division of peak at  $22^\circ$ - $22.5^\circ$  ( $2\theta$ ).

In the case of  $\text{ZrMg}_{0.95}\text{Ni}_{0.05}\text{Mo}_3\text{O}_{12}$  (Figure 21a) and  $\text{ZrMg}_{0.9}\text{Ni}_{0.1}\text{Mo}_3\text{O}_{12}$  (Figure 21b), the transition temperature is not well defined from XRPD since at 173K the system was close to the phase transformation temperature. This fact indicates that possibly there is below 173K.

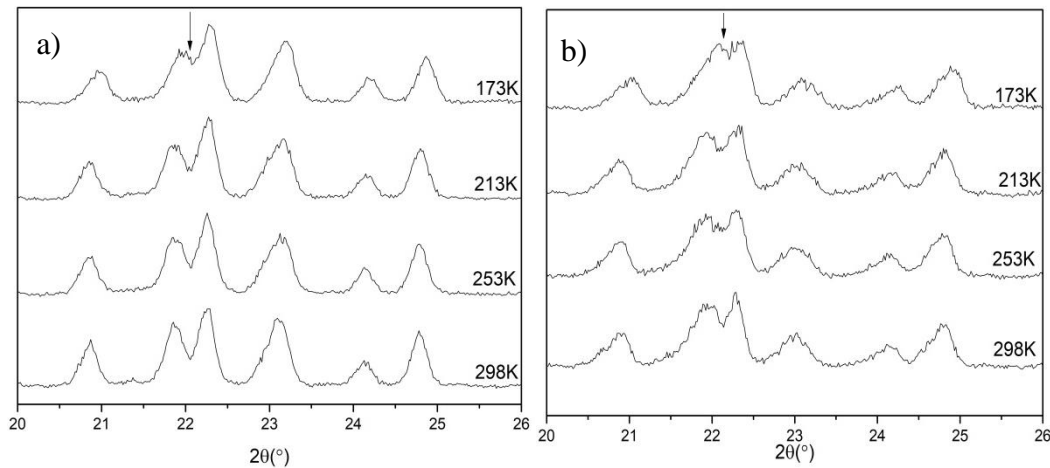


**Figure 21-** a) Diffraction pattern of  $\text{ZrMg}_{0.95}\text{Ni}_{0.05}\text{Mo}_3\text{O}_{12}$  system and b) Diffraction pattern of  $\text{ZrMg}_{0.9}\text{Ni}_{0.1}\text{Mo}_3\text{O}_{12}$  system. (↓) Characteristic pick which corresponds to the transition of monoclinic to orthorhombic structure by the division of peak at  $22^\circ$ - $22.5^\circ$  ( $2\theta$ ).

### 5.3.2. Phase transition temperature by DSC

DSC was applied to determine phase transition temperature more accurately. The temperature variation of phase transition in this ceramic family is attributed to the electronegativity of the cations [48]. In this case, electronegativity of  $\text{Zn}^{2+}$  is 1.65 (in accordance to Pauling scale), of  $\text{Ni}^{2+}$  is 1.91, while electronegativity of  $\text{Mg}^{2+}$  is 1.31 (Pauling) [48]. A displaced phase transition for monoclinic to orthorhombic structure was observed due to the breakage of secondary bonds between neighboring polyhedra, leaving more space within the orthorhombic crystal structure in comparison to monoclinic one [23][71].

Romao et al., [2] found a temperature phase transition (monoclinic to orthorhombic structure) for  $\text{ZrMgMo}_3\text{O}_{12}$  pattern phase at 147 K. In this work, this fact could be observed at 153 K, quite close to the previously reported. An endothermic event on heating is shown in Figure 22, associated to transition phase from monoclinic to orthorhombic structure [72]. In this figure it is demonstrated that when composition of a higher electronegative cation ( $\text{Zn}^{2+}$ ) is increased, the temperature phase transition is raised as shown in Table 7.

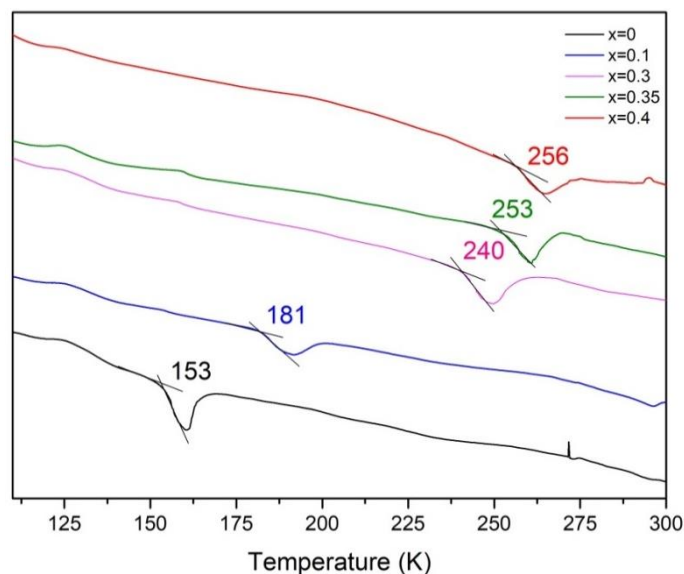


**Figure 22-** Onset temperatures getting by DSC. As increasing  $Zn^{2+}$  composition in  $ZrMg_{1-x}Zn_xMo_3O_{12}$ ; the phase transition temperature increase.

**Table 7-** Transition Temperature (K) of  $ZrMg_{1-x}Zn_xMo_3O_{12}$  system determined by DSC.

System	Transition Temperature (K)
$ZrMgMo_3O_{12}$	153
$ZrMg_{0.9}Zn_{0.1}Mo_3O_{12}$	181
$ZrMg_{0.7}Zn_{0.3}Mo_3O_{12}$	240
$ZrMg_{0.65}Zn_{0.35}Mo_3O_{12}$	253
$ZrMg_{0.6}Zn_{0.4}Mo_3O_{12}$	256

Temperature phase transition for some other phases in  $ABM_3O_{12}$  subfamily was also studied by DSC such as  $HfMgMo_3O_{12}$ , which temperature of phase transition is below room temperature at  $\sim 175$  K. [19]. Nevertheless, for  $HfMgW_3O_{12}$  [73], the temperature phase transition occurs above room temperature about (400-473K).

In some materials a characteristic event for phase transition from more dense structure (monoclinic) to less dense structure (orthorhombic) is occurred at high temperatures such as  $In_{0.5}(ZrMg)_{0.75}Mo_3O_{12}$  which temperature phase transition is around 355K [71],  $Al_{2-x}Ga_xW_3O_{12}$  system [74] for values  $x \leq 0.5$ , the phase transition temperature is between 343-373 K.

For the  $\text{ZrMg}_{1-x}\text{Ni}_x\text{Mo}_3\text{O}_{12}$  system, the same behavior as  $\text{ZrMg}_{1-x}\text{Zn}_x\text{Mo}_3\text{O}_{12}$  system was observed (Figure 23). The onset temperature phase transition is depicted in Table 8.

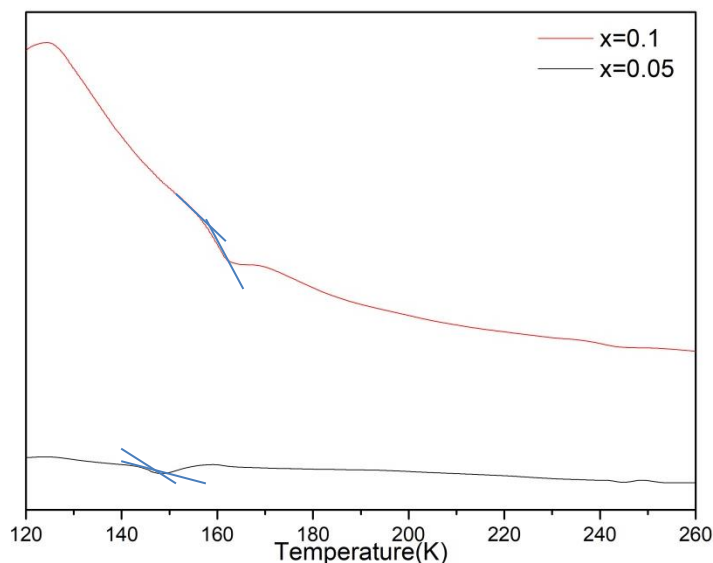


**Figure 23**-DSC curves for  $\text{ZrMg}_{0.95}\text{Ni}_{0.05}\text{Mo}_3\text{O}_{12}$  and  $\text{ZrMg}_{0.9}\text{Ni}_{0.1}\text{Mo}_3\text{O}_{12}$  phases.

**Table 8**- Temperatures of phase transition of  $\text{ZrMg}_{1-x}\text{Ni}_x\text{Mo}_3\text{O}_{12}$  determined by DSC.

System	Transition Temperature (K)
$\text{ZrMg}_{0.95}\text{Ni}_{0.05}\text{Mo}_3\text{O}_{12}$	144
$\text{ZrMg}_{0.9}\text{Ni}_{0.1}\text{Mo}_3\text{O}_{12}$	161

#### 5.4.

#### Thermal expansion coefficient at low temperatures

As already mentioned in section 2.6, through partial substitution of a smaller cation by a larger one, the chemical bonds between  $\text{A}^{2+}$  and  $\text{O}^{2-}$  become weaker and, consequently, the octahedra will be less rigid and a more negative CTE will be generated, as understood to occur in the case of the substitution of  $\text{Mg}^{2+}$  (0.072nm) by  $\text{Zn}^{2+}$  (0.074nm). On the other hand, when a larger size cation is partially substituted by a lower one, bonds between  $\text{A}^{2+}$  and  $\text{O}^{2-}$  will be stronger and the polyhedra will be less rigid, obtaining a less negative CTE, as in the case of Mg (0.072nm) substitution by Ni (0.069nm). Therefore, by these two paths, a

CTE closer to zero could be obtained [45]. Song et al., [3] reported that  $\text{ZrMgMo}_3\text{O}_{12}$  has a negative thermal expansion ( $\alpha_l = -3.8 \times 10^{-6} \text{ K}^{-1}$ ) covering a large temperature range from 300 to 1000 K, without phase transition and no hygroscopicity. However, Romao et al., [2] reported that  $\text{ZrMgMo}_3\text{O}_{12}$  exhibits near-zero thermal expansion ( $\alpha_l = 1.6 \times 10^{-7} \text{ K}^{-1}$ ) in a range of 298-723K. In order to determine the coefficient of thermal expansion in  $\text{ZrMg}_{1-x}\text{Zn}_x\text{Mo}_3\text{O}_{12}$  and  $\text{ZrMg}_{1-x}\text{Ni}_x\text{Mo}_3\text{O}_{12}$ , XRPD powder diffraction was performed at low temperatures (298, 253, 213 and 173 K).

The coefficient of thermal expansion for  $\text{ZrMgMo}_3\text{O}_{12}$ , are showed in Appendix A, Figure A.1. For  $\text{ZrMg}_{0.9}\text{Zn}_{0.1}\text{Mo}_3\text{O}_{12}$  phase was observed that the lowest measurement temperature was situated very close to its phase transition temperature  $\sim 181\text{K}$ , reason why this last measurement was discarded and the evaluation of the CET was carried out with only three temperatures 298 K, 253 K and 213 K. In Figure 24 the linearization of these three points is demonstrated, showing the values of the coefficient of volumetric CTE, which corresponds to  $\alpha_v = 8.45 \times 10^{-7} \text{ K}^{-1}$ . As shown is section 2.2.1, to obtain the value of the linear CTE, Equation 3 was applied. As a result  $\text{ZrMg}_{0.9}\text{Zn}_{0.1}\text{Mo}_3\text{O}_{12}$  shows a near zero linear thermal expansion  $\alpha_l = 2.82 \times 10^{-7} \text{ K}^{-1}$ .

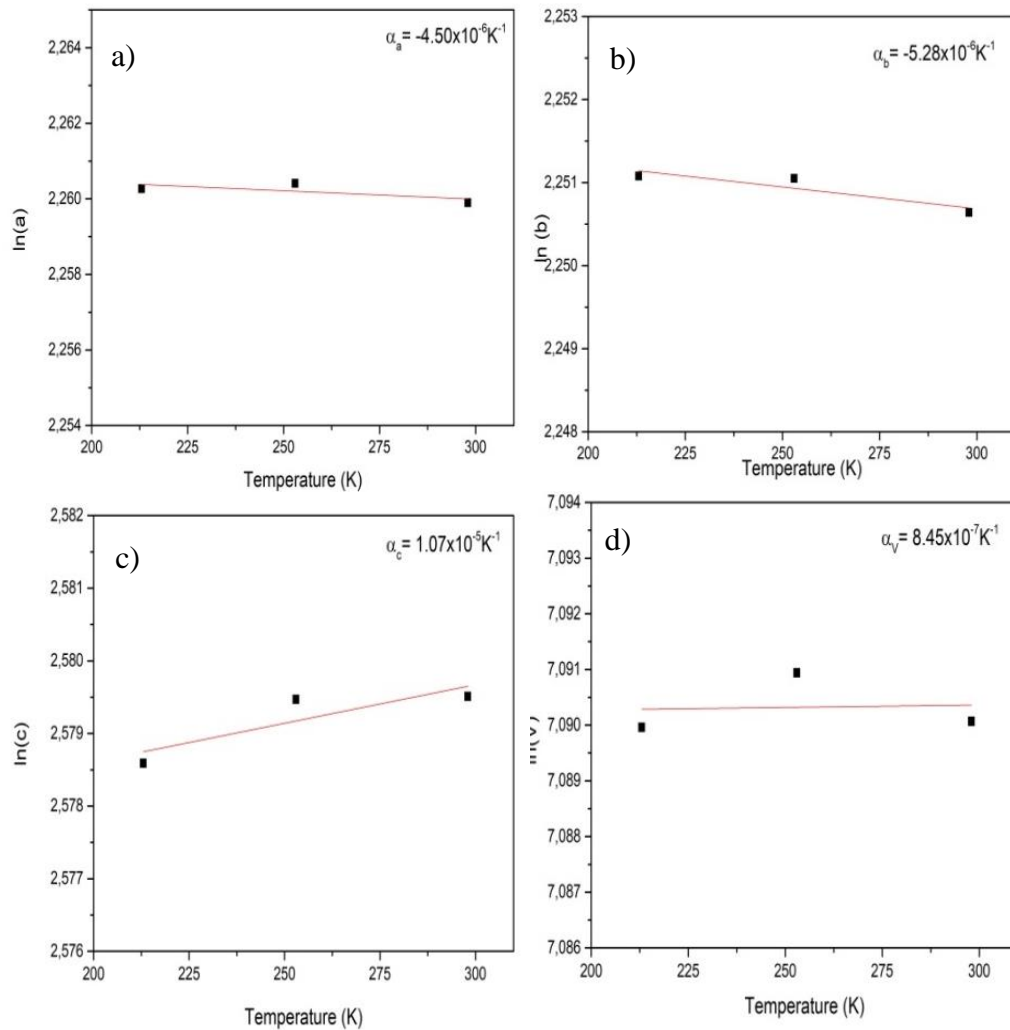


**Figure 24-** Coefficients of thermal expansion for  $\text{ZrMg}_{0.9}\text{Zn}_{0.1}\text{Mo}_3\text{O}_{12}$  phase in three crystallographic directions and volumetric one; a) a-axes, b) b-axes c) c-axes and d) volume.

Most of the estimations of CTE in  $\text{A}_2\text{M}_3\text{O}_{12}$  family are done in high temperatures by virtue of many materials are used in some applications such as thermal shock resistance [50].

## 5.5. Thermal expansion coefficient at high temperatures

Based on the same considerations discussed in 5.4 section it is expected to obtain a near-zero CTE in the proposed phases of  $\text{ZrMg}_{1-x}\text{Zn}_x\text{Mo}_3\text{O}_{12}$  system.  $\text{ZrMg}_{0.7}\text{Zn}_{0.3}\text{Mo}_3\text{O}_{12}$  phase (Figure 26), shows a  $\alpha_v = 2.34 \times 10^{-6} \text{K}^{-1}$  with a near zero linear thermal expansion  $\alpha_l = 7.80 \times 10^{-7} \text{K}^{-1}$ .

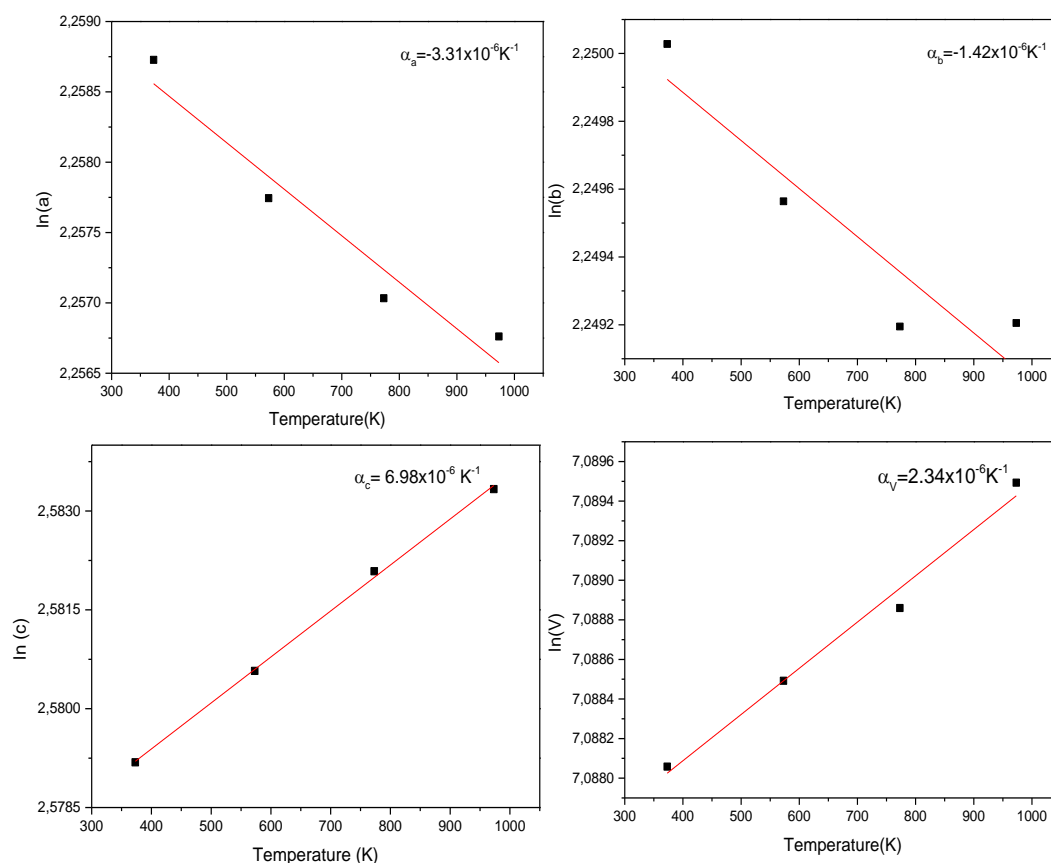


**Figure 25-** Coefficients of thermal expansion for  $\text{ZrMg}_{0.7}\text{Zn}_{0.3}\text{Mo}_3\text{O}_{12}$  phase in three crystallographic directions and volume; a) a-axes, b) b-axes c) c-axes and d) volume.

In respect to  $\text{ZrMg}_{0.6}\text{Zn}_{0.4}\text{Mo}_3\text{O}_{12}$  phase, although the solubility limit of  $\text{Zn}^{2+}$  has been reached and the presence of more phases is observed such as  $\text{ZrMo}_2\text{O}_8$  and  $\text{ZnMoO}_4$ , the volumetric CET obtained is  $\alpha_v = 2.31 \times 10^{-6} \text{K}^{-1}$  and its linear CTE value is  $\alpha_l = 7.70 \times 10^{-7} \text{K}^{-1}$ . A summary for the CTE in  $\text{ZrMg}_{1-x}\text{Zn}_x\text{Mo}_3\text{O}_{12}$  system is shown in Table 9. Results obtained in this work is not possible to compare with other authors, since the range of temperature used here was different as other ones already reported as  $\text{ZrMgMo}_3\text{O}_{12}$ , which range of temperature for CTE determination was about (298-723K)[2].

**Table 9-** Near zero thermal expansion coefficients for some  $\text{ZrMg}_{1-x}\text{Zn}_x\text{Mo}_3\text{O}_{12}$  phases.

System	$\alpha_t \times 10^{-7} (\text{K}^{-1})$	Temperature range (K)
ZrMg <sub>0.8</sub> Zn <sub>0.3</sub> Mo <sub>3</sub> O <sub>12</sub>	7.80x10 <sup>-7</sup>	373-973
ZrMg <sub>0.6</sub> Zn <sub>0.4</sub> Mo <sub>3</sub> O <sub>12</sub>	7.70x10 <sup>-7</sup>	373-973

As already shown in chapter 2.5 and 2.6, there is a relationship between the A cation and the CTE. In the case of partial substitution of a large cation in A<sub>2</sub>M<sub>3</sub>O<sub>12</sub> family, is possible to reach coefficient of thermal expansion close to zero as shown in Table 10. An example is the replacement of Zn (0.74Å) by Mg (0.72Å) in HfMg<sub>1-x</sub>Zn<sub>x</sub>Mo<sub>3</sub>O<sub>12</sub> system, resulting in a near zero thermal expansion material [46]. Nevertheless in other study, replacement of smaller cation such as Mo<sup>2+</sup> (0.62 Å) by Mg<sup>2+</sup> (0.72 Å) in HfMgMo<sub>2.5</sub>W<sub>0.5</sub>O<sub>12</sub> phase and Zr<sup>4+</sup> (0.72 Å) and Mg<sup>2+</sup> (0.72Å) by In<sup>3+</sup> (0.81 Å) is resulting in a near zero thermal expansion [75]. Bearing in mind the hypotheses which is related to CTE and A<sup>2+</sup> size, for the case of partial substitution of Zn<sup>2+</sup> by Mg<sup>2+</sup>, the CTE turned more positive as it was unexpected. It could be deduced that a bigger A cation do not follow this hypothesis, in which applying a bigger cation, less negative the CTE will be. In other hand this hypothesis is clearly demonstrated for other phases such as HfMgMoWO<sub>12</sub> [19] and ZrFeMo<sub>2</sub>VO<sub>12</sub> [76].

A lower CTE is shown for molybdates, (Tabe 10), confirmed a considerably distortion of AO<sub>6</sub> polyhedra molybdate when compared with tungstate, and it is concluded that a chemical substitution dramatically influences in the thermal expansion properties of materials [46].

**Table 10-** Near zero thermal expansion coefficients for some A<sub>2</sub>M<sub>3</sub>O<sub>12</sub> phases, according to the literature.

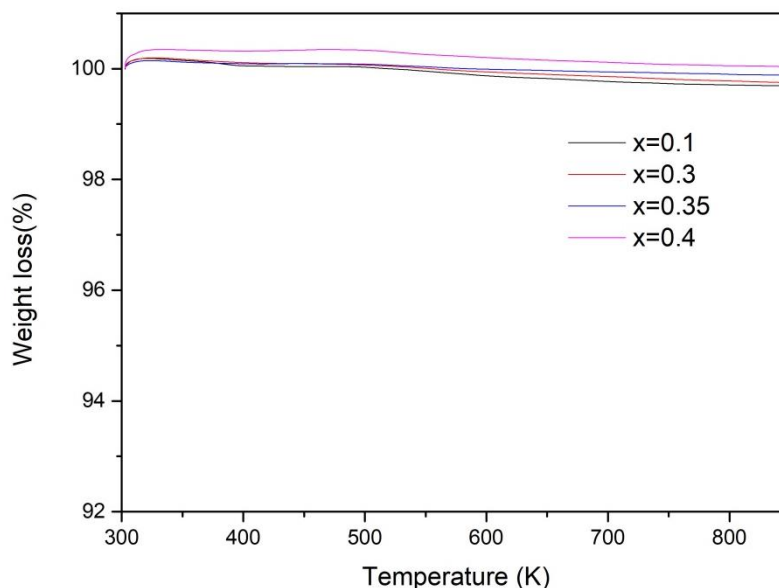
Phase	$\alpha_t \times 10^{-7} (\text{K}^{-1})$	Temperature range (K)	Reference
ZrFeMo <sub>2</sub> VO <sub>12</sub>	3.6	401-573	[76]
HfMgMo <sub>2.5</sub> W <sub>0.5</sub> O <sub>12</sub>	4.8	300-700	[75]
HfMg <sub>0.9</sub> Zn <sub>0.1</sub> Mo <sub>3</sub> O <sub>12</sub>	0.5	303-673	[77]
HfMg <sub>0.7</sub> Zn <sub>0.3</sub> Mo <sub>3</sub> O <sub>12</sub>	-0.9	323-673	[77]
HfMg <sub>0.5</sub> Zn <sub>0.5</sub> Mo <sub>3</sub> O <sub>12</sub>	-1.1	373-673	[77]
In <sub>0.5</sub> (ZrMg) <sub>0.75</sub> Mo <sub>3</sub> O <sub>12</sub>	-1.6	373-773	[71]

## 5.6.

### Hygroscopicity in $\text{ZrMg}_{1-x}\text{Zn}_x\text{Ni}_x\text{Mo}_3\text{O}_{12}$ systems

In order to evaluate hygroscopicity and eventual decomposition of the orthorhombic phases at high temperatures thermogravimetric analyses have been performed. Hygroscopicity would be relevant since affects thermal expansion behavior of the hygroscopic phases [28].

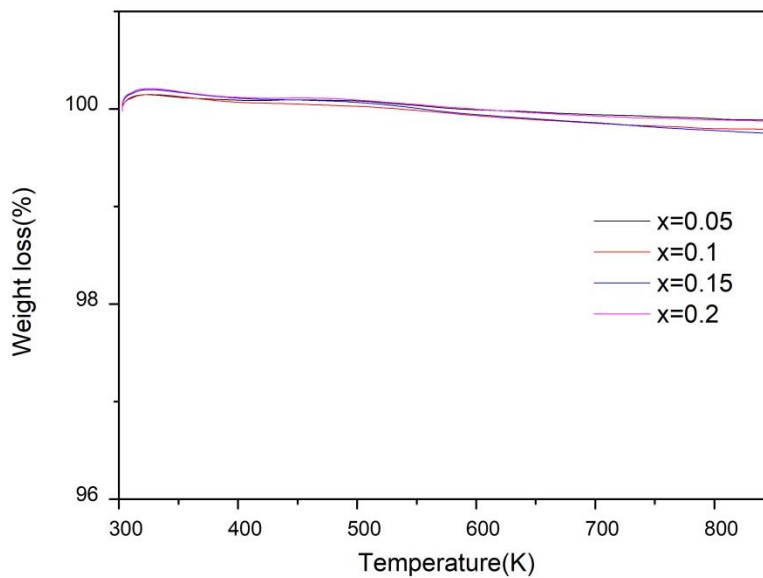
For all samples corresponding to the  $\text{ZrMg}_{1-x}\text{Zn}_x\text{Mo}_3\text{O}_{12}$  (Figure 27) and  $\text{ZrMg}_{1-x}\text{Ni}_x\text{Mo}_3\text{O}_{12}$  (Figure 28) systems, the mass loss was negligible in whole temperature range (from room temperature until  $900^\circ\text{C}$ ), and lower than 0.31% as could be observed in Figures 27, 28 and, more accurately, on Tables 11 and 12. Besides that no decomposition of the material has been observed up to 900K. The absence of hygroscopicity would be expected in both phases since  $\text{ZrMgMo}_3\text{O}_{12}$  is not hygroscopic [78], however, the entrance of a larger cation ( $\text{Zn}^{2+}$ ) was considered to have certain potential to change this properties, which was not confirmed.



**Figure 26-** Weight loss for  $\text{ZrMg}_{1-x}\text{Zn}_x\text{Mo}_3\text{O}_{12}$  system.

**Table 11** - Weight loss in  $\text{ZrMg}_{1-x}\text{Zn}_x\text{Mo}_3\text{O}_{12}$  system as determined by TGA.

System	Weight loss (%)
$\text{ZrMgMo}_3\text{O}_{12}$	0.31
$\text{ZrMg}_{0.7}\text{Zn}_{0.3}\text{Mo}_3\text{O}_{12}$	0.25
$\text{ZrMg}_{0.65}\text{Zn}_{0.35}\text{Mo}_3\text{O}_{12}$	0.12
$\text{ZrMg}_{0.6}\text{Zn}_{0.4}\text{Mo}_3\text{O}_{12}$	0.02

**Figure 27**- Weight loss as a function of temperature for  $\text{ZrMg}_{1-x}\text{Ni}_x\text{Mo}_3\text{O}_{12}$  system.**Table 12**- Weight loss (%) of  $\text{ZrMg}_{1-x}\text{Ni}_x\text{Mo}_3\text{O}_{12}$  system as determined by TGA.

System	Weight loss (%)
$\text{ZrMg}_{0.95}\text{Ni}_{0.05}\text{Mo}_3\text{O}_{12}$	0.12
$\text{ZrMg}_{0.9}\text{Ni}_{0.1}\text{Mo}_3\text{O}_{12}$	0.13
$\text{ZrMg}_{0.85}\text{Ni}_{0.15}\text{Mo}_3\text{O}_{12}$	0.21
$\text{ZrMg}_{0.8}\text{Ni}_{0.2}\text{Mo}_3\text{O}_{12}$	0.25

As already reported by Duan et al., [79] for  $\text{ZrW}_2\text{O}_8$ , the incorporation of water molecules in the framework hinders the rocking motion of the  $\text{WO}_4$  tetrahedra and the  $\text{ZrO}_6$  octahedra, converting CTE to be slightly positive. In the case of the  $\text{Y}_2\text{W}_3\text{O}_{12}$  studied by Sumithra et al.,[28] the incorporation of water

molecules arrest the transverse thermal vibrations and prevent negative thermal expansion. Phases of the  $A_2M_3O_{12}$  family can be hygroscopic, especially those that are formed by large trivalent cations, such as rare earths  $Y^{3+}$  [45],  $Ho^{3+}$  [9],  $Yb^{3+}$  [44] among others. Since here studied phases present a non-significant mass loss the water will not hinder transverse vibrations between the polyhedra and thus these phases will present their intrinsic thermal expansion properties

In addition in some phases such as  $Y_2Mo_3O_{12}$ [29] and  $Lu_2W_3O_{12}$  [80] water molecules that occupy the microchannels along c- crystallographic direction, are capable to amorphize the phase. This is not the case of the phases within the  $ZrMg_{1-x}Zn_xMo_3O_{12}$  and  $ZrMg_{1-x}Ni_xMo_3O_{12}$  systems due to almost complete absence of water. For all compositions it is possible to observe a mass gain at the beginning of the scan, this can be attributed to the time in which the equipment is stabilized before making the measurement.

## 5.7.

### **Effect of the addition of $Zn^{2+}$ and $Ni^{2+}$ cations on the UV-Vis absorption in $ZrMg_{1-x}Zn_xMo_3O_{12}$ and $ZrMg_{1-x}Ni_xMo_3O_{12}$ systems**

The most suitable ceramic semiconductor materials for photocatalytic development have similar characteristics and promote studies to increase the efficiency and commercial viability of photocatalysis. In this context the band-gap energy study could be applied in order to know if the as-prepared phases are promising candidates for photocatalysis [81].

Within the  $A_2M_3O_{12}$  family  $Al_2W_3O_{12}$  phase when  $Al^{3+}$  is replaced by  $Y^{3+}$ ,  $Sc^{3+}$ ,  $Fe^{2+/3+}$  and  $Cr^{3+}$ , the color of the material changes by the presence of  $Y^{3+}$  and transition metal cations [82][83][4]. An indirect transition for the fundamental absorption is assumed for the two new systems (Figure 29 and Figure 31) and band-gap energies were obtained by the Kubelka-Munk equation, by plotting  $(F(R)hv)^{1/2}$  and extrapolating the straight-line portion of the UV-Vis spectra to  $(F(R)hv)^{1/2} = 0$  [84]. The band-gap values for ZnO (as a wurtzite structure) and for  $ZrMg_{1-x}Zn_xMo_3O_{12}$  system are displayed in Table 13.

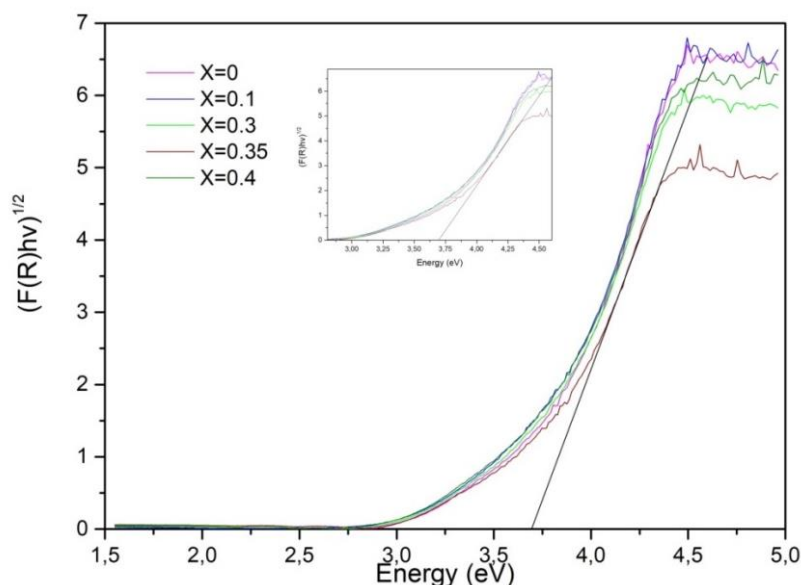


**Figure 28-** Kubelka-Munk plots of  $\text{ZrMg}_{1-x}\text{Zn}_x\text{Mo}_3\text{O}_{12}$  system, regarding an indirect transition as a function of excitation energy and the extrapolations  $(F(R)hv)^{1/2} = 0$  used to obtain the band-gap energies.

**Table 13-** Band-gap energies for  $\text{ZrMg}_{1-x}\text{Zn}_x\text{Mo}_3\text{O}_{12}$  system.

Phase	Band- Gap Energy (eV)
ZnO	3.22
$\text{ZrMgMo}_3\text{O}_{12}$	3.73
$\text{ZrMg}_{0.9}\text{Zn}_{0.1}\text{Mo}_3\text{O}_{12}$	3.61
$\text{ZrMg}_{0.8}\text{Zn}_{0.2}\text{Mo}_3\text{O}_{12}$	3.65
$\text{ZrMg}_{0.7}\text{Zn}_{0.3}\text{Mo}_3\text{O}_{12}$	3.65
$\text{ZrMg}_{0.65}\text{Zn}_{0.35}\text{Mo}_3\text{O}_{12}$	3.69
$\text{ZrMg}_{0.6}\text{Zn}_{0.4}\text{Mo}_3\text{O}_{12}$	3.63

Considering a large gap semiconductor, if pure, the material is colorless, but the presence of impurities can introduce color in the semiconductor [54]. Prisco et al., [41] studied the  $\text{Al}_2\text{W}_3\text{O}_{12}$  phase, which band-gap energy is around 3.11eV, appearing as a white powder. However, Müller et al., [74] reported the replacement of  $\text{Al}^{3+}$  by  $\text{Ga}^{3+}$  within the  $\text{Al}_2\text{W}_3\text{O}_{12}$  phase, which makes the system sensitive to the UV- vis absorption, adopting a yellow-green color. The same occurs with the addition of  $\text{Ni}^{2+}$  in  $\text{ZrMgMo}_3\text{O}_{12}$ , getting a yellow color powder.

For  $\text{ZrMg}_{1-x}\text{Ni}_x\text{Mo}_3\text{O}_{12}$  (Figure 29), a decrease was observed in the band-gap energy when  $\text{Ni}^{2+}$  composition increases (Table 14). This fact could be explained by the increment of 3d orbitals from  $\text{Ni}^{2+}$  transition metal within the band-gap and their interaction with valence band of the material, resulting in a decreasing of the band-gap energy, since  $\text{Ni}^{2+}$  ions are regarded as p-type semiconductor. This evidence was also studied by Morgado et al., [84][85] for  $\text{Co}^{2+}$  and  $\text{Fe}^{2+}$  and Nishikawa et al., for  $\text{Ni}^{2+}$  in transition metals in which band gap values are decreasing as the composition of the transition metal increases. Thus this similar behavior is observed for  $\text{ZrMg}_{1-x}\text{Ni}_x\text{Mo}_3\text{O}_{12}$  system. Another behavior is shown for  $x=0.4$ , in which is evident two more transitions; it could be explained by the presence of one more phase ( $\text{NiMoO}_4$ ).

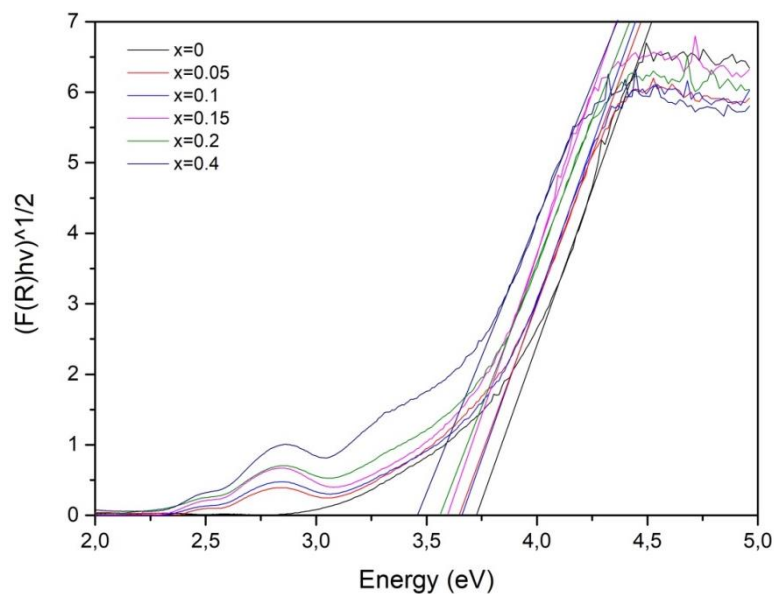


**Figure 29-** Kubelka-Munk curves of  $\text{ZrMg}_{1-x}\text{Ni}_x\text{Mo}_3\text{O}_{12}$  system, considering an indirect transition.

**Table 14-** Band-gap energy of  $\text{ZrMg}_{1-x}\text{Ni}_x\text{Mo}_3\text{O}_{12}$  system.

Samples	Bans-gap energy (eV)
NiO	3.60
$\text{ZrMgMo}_3\text{O}_{12}$	3.73

ZrMg <sub>0.95</sub> Ni <sub>0.05</sub> Mo <sub>3</sub> O <sub>12</sub>	3.65
ZrMg <sub>0.9</sub> Ni <sub>0.1</sub> Mo <sub>3</sub> O <sub>12</sub>	3.63
ZrMg <sub>0.85</sub> Ni <sub>0.15</sub> Mo <sub>3</sub> O <sub>12</sub>	3.59
ZrMg <sub>0.8</sub> Ni <sub>0.2</sub> Mo <sub>3</sub> O <sub>12</sub>	3.57
ZrMg <sub>0.6</sub> Ni <sub>0.4</sub> Mo <sub>3</sub> O <sub>12</sub>	3.45

Figure 30 exhibit a band around 2.7-2.9 eV, which is related to the typical *d-d* transition of Ni<sup>2+</sup> ions [86]. The absorption band due to *d-d* transition is a common behavior for semiconductors which are doped by transition metals [84][85].

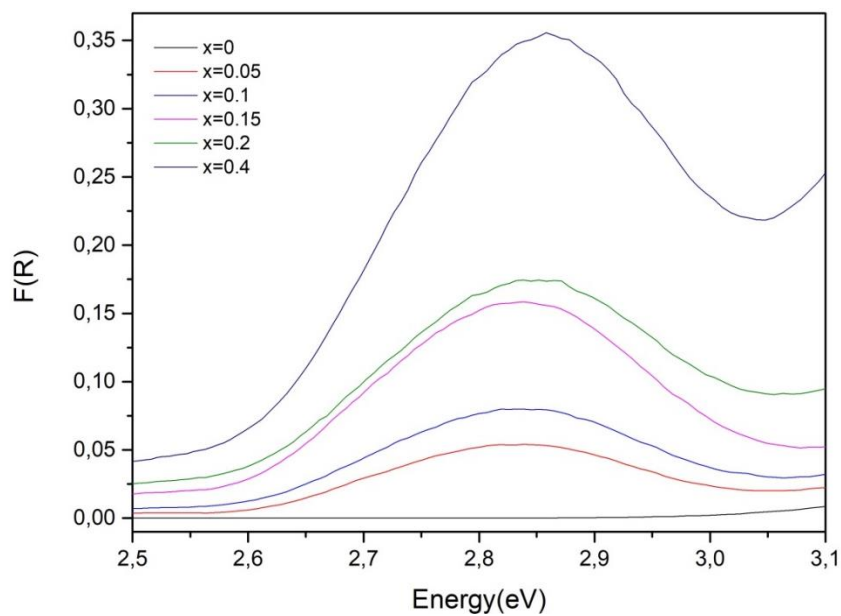


**Figure 30-** UV-Vis spectra for ZrMg<sub>1-x</sub>Ni<sub>x</sub>Mo<sub>3</sub>O<sub>12</sub> system.

In fact, the intensity of the absorption band remarkable enhances with the increment of Ni<sup>2+</sup> ions in the composition, improving the photon absorption process in the visible region of the electromagnetic spectrum, indicated by a strong band narrowing [86].

## 5.8. Raman Spectroscopy

In order to understand the vibrational properties, phase composition and homogeneity of the as-synthesized materials,  $\text{ZrMg}_{1-x}\text{Zn}_x\text{Mo}_3\text{O}_{12}$  and  $\text{ZrMg}_{1-x}\text{Ni}_x\text{Mo}_3\text{O}_{12}$  systems were studied using the Raman spectroscopy. This is a complementary technique, since it is more sensitive for phase detection when compared with XRPD, while also could identify stretching modes of  $\text{AO}_6$  and  $\text{MO}_4$  coordination polyhedral, low-energy bending, librational modes and symmetric and antisymmetric stretching at high modes [46]. The Raman spectra of the initial reactants materials were performed as sake of comparison with the as-prepared systems.

Raman spectrum of the  $\text{MoO}_3$  sample shows the four vibrational modes of the  $\text{MoO}_4^{2-}$  species:  $\nu_1$  ( $A_1$ )(850-1100  $\text{cm}^{-1}$ ), attributed to the symmetric modes,  $\nu_2$  (E) (300-500  $\text{cm}^{-1}$ ), assigned to the bending modes,  $\nu_3$  ( $F_2$ ) (720-820  $\text{cm}^{-1}$ ), related to the antisymmetric vibrational modes and  $\nu_4$  ( $F_2$ ) (300-500  $\text{cm}^{-1}$ ), attributed as bending modes of  $\text{MoO}_4^{2-}$  species. In detail, the peak at 995  $\text{cm}^{-1}$  is assigned as  $\nu_s$  and  $\nu_{\text{ass}}$  of O-Mo-O units, while the band at 820  $\text{cm}^{-1}$  is attributed to the symmetric and antisymmetric stretching of Mo-O-Mo brigdes [87]. The weak peak at 660  $\text{cm}^{-1}$  is related to antisymmetric stretching of Mo-O bonds. The peaks present in the spectral range from 300 to 550  $\text{cm}^{-1}$  are assigned as bending modes of Mo-O bonds. The bands at 102, 110, 160 and 180  $\text{cm}^{-1}$  are associated to the translation and rotation modes of  $\text{MoO}_4^{2-}$  [88].  $\text{MoO}_3$  spectra is shown in Figure 31.

Raman spectrum of  $\text{ZrO}_2$  reactant present peaks related to two crystalline phases of zirconia: tetragonal and monoclinic [89] [90]. The bands centered at 177, 192, 337, 348, 386, 485, 561 and 614  $\text{cm}^{-1}$  are attributed to the vibrational stretching of monoclinic  $\text{ZrO}_2$  and the peak at 639  $\text{cm}^{-1}$  is described as vibrational stretching of tetragonal  $\text{ZrO}_2$  [91].  $\text{ZrO}_2$  spectra is shown in Figure 31.

$\text{ZnO}$  Raman spectrum presents five active vibrational modes: a narrow band at 437  $\text{cm}^{-1}$  is assigned as  $E_2$  mode of the wurtzite phase, the two bands around 330  $\text{cm}^{-1}$  are ascribed as second-order Raman scattering arising from phonon modes [92]. A weak band at 538  $\text{cm}^{-1}$  associated with  $\text{ZnO}$  vacancy and its intensity varies as the crystallinity of the sample. Finally, the band at 383  $\text{cm}^{-1}$

is related to the order-disorder of the lattice [93] [94]. MgO Raman spectra is constituted by a band  $440\text{ cm}^{-1}$  related to the cubic phase as shown in Figure 31.

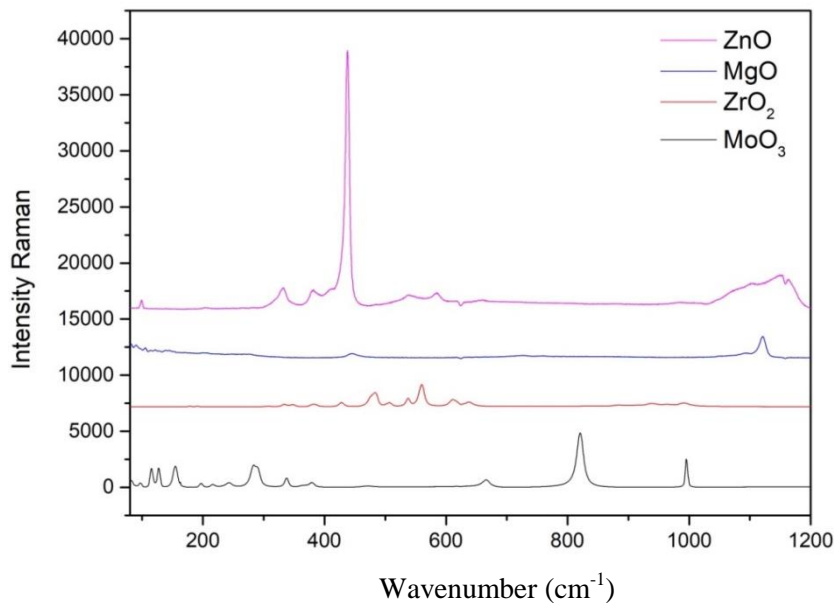


**Figure 31-** Raman spectra for precursor oxides (ZnO, MgO, ZrO<sub>2</sub> and MoO<sub>3</sub>).

Figure 32 shows Raman spectra of the a) ZrMg<sub>0.7</sub>Zn<sub>0.3</sub>Mo<sub>3</sub>O<sub>12</sub> and b) ZrMg<sub>0.8</sub>Ni<sub>0.2</sub>Mo<sub>3</sub>O<sub>12</sub> compositions and a degree of low homogeneity could be observed in comparison to the un-doped c) ZrMgMo<sub>3</sub>O<sub>12</sub> phase powder. The same behavior has been observed for other compositions (shown in Appendix A.4). ZrMgMo<sub>3</sub>O<sub>12</sub> exhibits very similar bands to those of the family A<sub>2</sub>M<sub>3</sub>O<sub>12</sub> with corner-sharing between AO<sub>6</sub> and MoO<sub>4</sub> polyhedra. A similar Raman spectrum was also acquired for ZrMnMo<sub>3</sub>O<sub>12</sub> phase [95].

In Figure 32 c, for ZrMgMo<sub>3</sub>O<sub>12</sub> system the bands below  $160\text{ cm}^{-1}$  are attributed to translation and rotation modes of MoO<sub>4</sub><sup>2-</sup> [78]. The bands at  $305$ ,  $334$  and  $353\text{ cm}^{-1}$ , are ascribed as bending modes of the MoO<sub>4</sub><sup>2-</sup> species as well as MoO<sub>3</sub> amount [3]. The bands at  $728$ ,  $737$ ,  $747$  and  $789\text{ cm}^{-1}$  are related to the antisymmetric stretching of Mo-O [96]. The band centered at  $820\text{ cm}^{-1}$  is assigned as symmetric and antisymmetric vibration modes of Mo-O-Mo bridges, characteristic of the corner-sharing polyhedra [96]. The band at  $950\text{ cm}^{-1}$  is attributed to the symmetric vibration stretching of O-Mo-O linkages [3] [95].

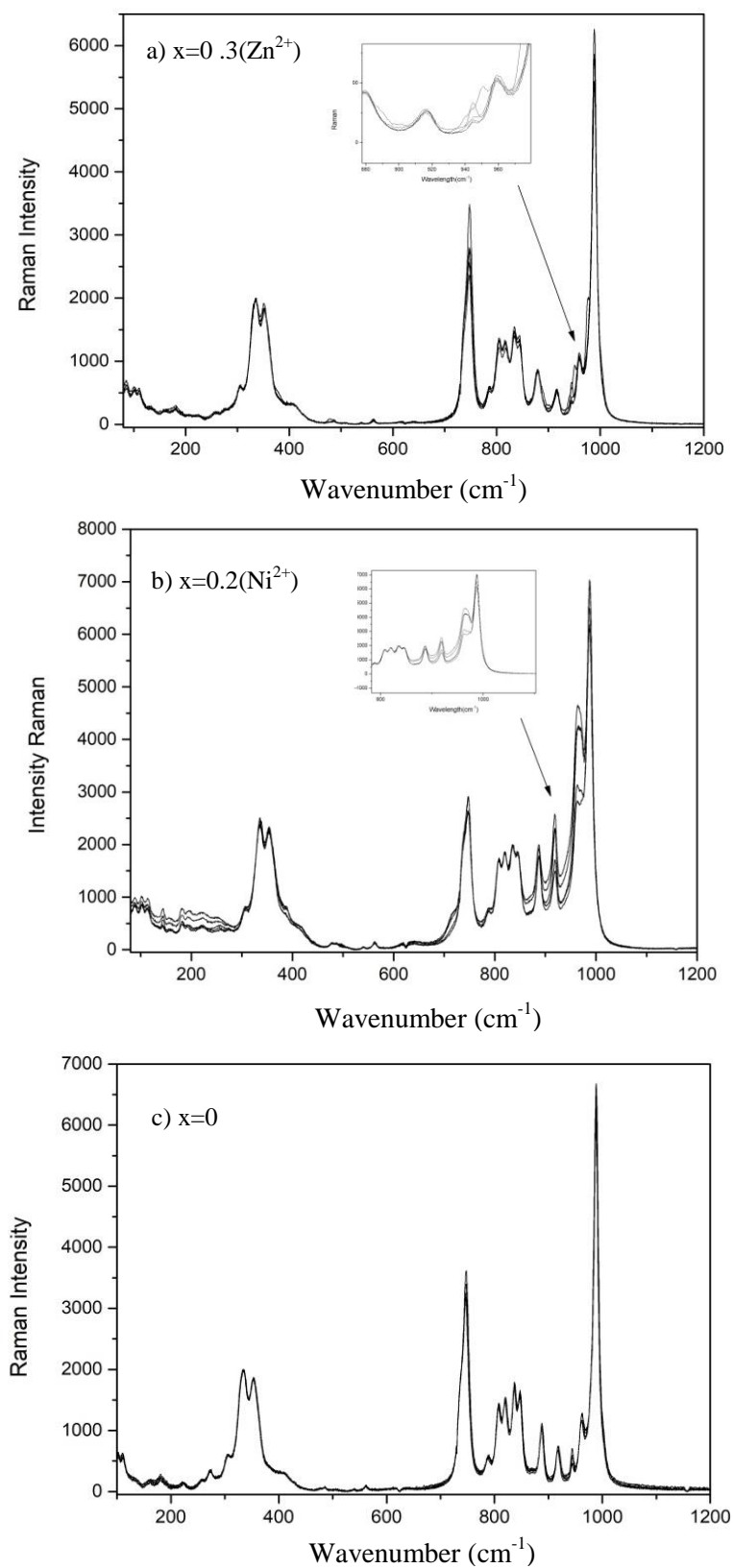


**Figure 32-** Raman spectrum of the a)  $\text{ZrMg}_{0.7}\text{Zn}_{0.3}\text{Mo}_3\text{O}_{12}$ , b)  $\text{ZrMg}_{0.8}\text{Ni}_{0.2}\text{Mo}_3\text{O}_{12}$ , and c)  $\text{ZrMgMo}_3\text{O}_{12}$  systems and depicts spectral information of five points of the phases.

The peaks and a more accurate assignment of the vibrational modes of the Raman spectra of  $\text{ZrMg}_{1-x}\text{Zn}_x\text{Mo}_3\text{O}_{12}$  and  $\text{ZrMg}_{1-x}\text{Ni}_x\text{Mo}_3\text{O}_{12}$  systems are listed in Table 15.

**Table 15-** Assignment of vibrational modes of Raman spectra obtained in this work (according to the literature).

Mode	Range ( $\text{cm}^{-1}$ )	Peak ( $\text{cm}^{-1}$ )	Reference
Phonon modes	75-111	Below 300	[3]
Librational and translational	Below 200	100	[78]
Modes in $(\text{MoO}_4)^{2-}$	280-320	-	[95]
Tetrahedra Symmetric bending	320-400	-	[95]
Mo-O longer vibrations	300-400	392	[96]
Bending vibrations $(\text{MoO}_4)^{2-}$	300-400	-	[3]
$\nu_4$ ( $F_2$ ) Triply degenerate bending vibrations $(\text{MoO}_4)^{2-}$	300-500	318	[97]
$\nu_2$ (E) Doubly degenerate bending vibrations $(\text{MoO}_4)^{2-}$	300-500	381	[97]
$\nu_3$ ( $F_2$ ) Triply degenerate antisymmetric stretching vibrations $(\text{MoO}_4)^{2-}$	720-850	833	[97]
Stretching vibrations of the Mo-O bonds Mixing between Mo-O and $(\text{MoO}_4)^{2-}$	750-800	772	[96]
Antisymmetric stretching (Mo-O-Mo)	750-900	-	[3], [95]
$\nu_1$ ( $A_1$ ) Symmetrically stretching vibrations Mo-O-Mo	850-1100	894	[97], [96]
Internal Symmetric stretching $(\text{MoO}_4)^{2-}$	900-1050	-	[3], [95]

According to Song, et al.,[3] in the spectral range bellow  $200 \text{ cm}^{-1}$ , the most likely librational optical modes can be occurring. Lately, Romao et al.,[2] corroborated this statement for the  $\text{ZrMgMo}_3\text{O}_{12}$  phase, in which, at approximately  $100 \text{ cm}^{-1}$ , these modes are possible to occurring, in addition to

translation modes. Since lattice vibrations have a predominant role in the CTE, most of the phonon modes, such as 75 and 100  $\text{cm}^{-1}$ , contribute to negative thermal expansion [3]. As already reported by XRPD powder at room temperature in this work, the desired phases were formed and the presence of small amounts of  $\text{ZrMo}_2\text{O}_8$  is evident for all compositions of  $\text{ZrMg}_{1-x}\text{Zn}_x\text{Mo}_3\text{O}_{12}$  (Figure 33a) and  $\text{ZrMg}_{1-x}\text{Ni}_x\text{Mo}_3\text{O}_{12}$  (Figure 33b), presenting bending modes located at 178 [2] , 326, 352, 745 and 943  $\text{cm}^{-1}$  according to Liang et al., [98].

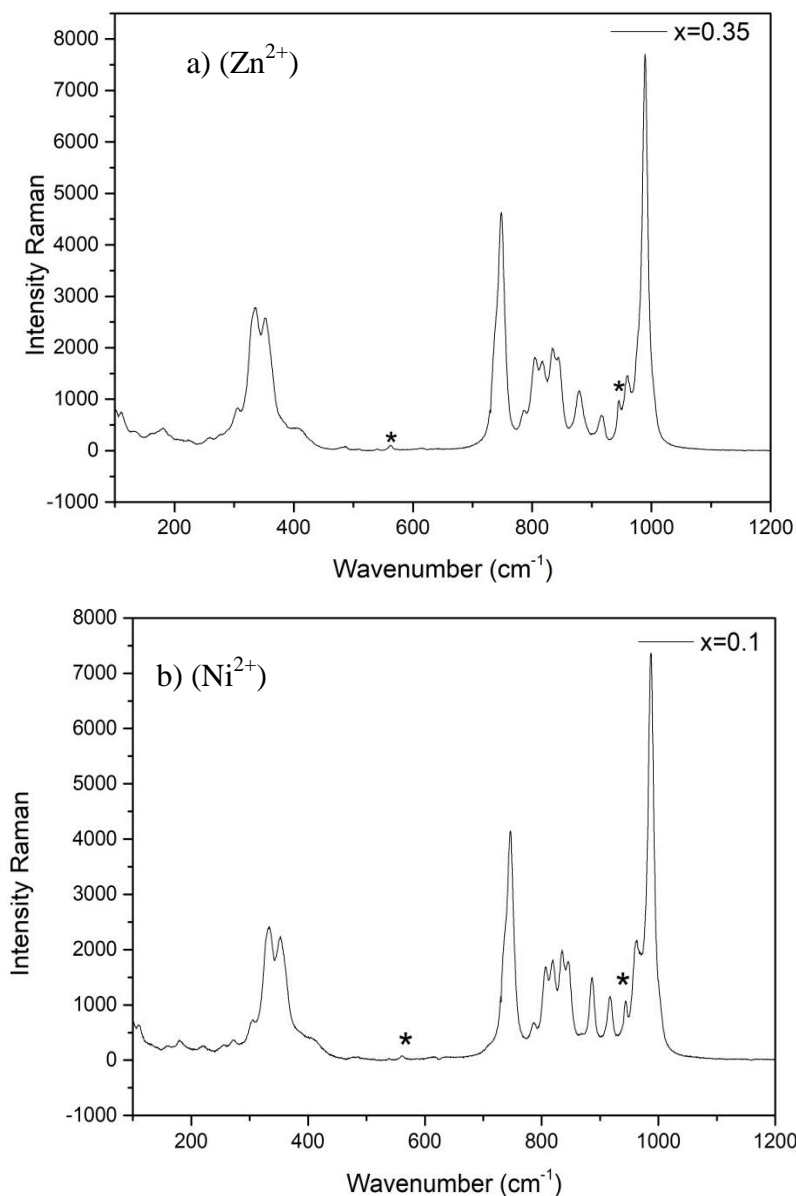


**Figure 33-** Raman spectrum of a)  $\text{ZrMg}_{0.65}\text{Zn}_{0.35}\text{Mo}_3\text{O}_{12}$  and b)  $\text{ZrMg}_{0.9}\text{Ni}_{0.1}\text{Mo}_3\text{O}_{12}$ . (\*) represents  $\text{Zr}_2\text{Mo}_2\text{O}_8$ .

The Raman spectrum of  $\text{ZrMg}_{0.7}\text{Zn}_{0.3}\text{Mo}_3\text{O}_{12}$  is quite similar to  $\text{ZrMgMo}_3\text{O}_{12}$  phase spectrum (Figure 34). However, for the compositions of  $x =$

0.35 and 0.4, the band at  $945\text{ cm}^{-1}$  appears and has been marked with (\*) in Figure 36. This fact could be attributed to the  $\text{MoO}_4^{2-}$  units, indicate short-range structural changes with the incorporation of  $\text{Zn}^{2+}$  ions. For instance, Raman spectrum of the sample  $x = 0.35$  shows the higher intensity of the aforementioned band, which indicates changes in the coordination of  $\text{Mo}^{6+}$  with the incorporation of  $\text{Zn}^{2+}$  ions, as depicted in Figure 34. Moreover, it can be inferred by the intensity of the band at  $945\text{ cm}^{-1}$  the formation of a secondary crystalline phase such as  $\text{ZnMoO}_4$ . This fact is very interesting due to the presence of  $\text{ZnMoO}_4$  for  $\text{ZrMg}_{0.65}\text{Zn}_{0.35}\text{Mo}_3\text{O}_{12}$  (Figure 34), which has not been recognized by XRPD, allowing us to affirm the more sensitive behavior of the Raman spectroscopy when compared to XRPD.

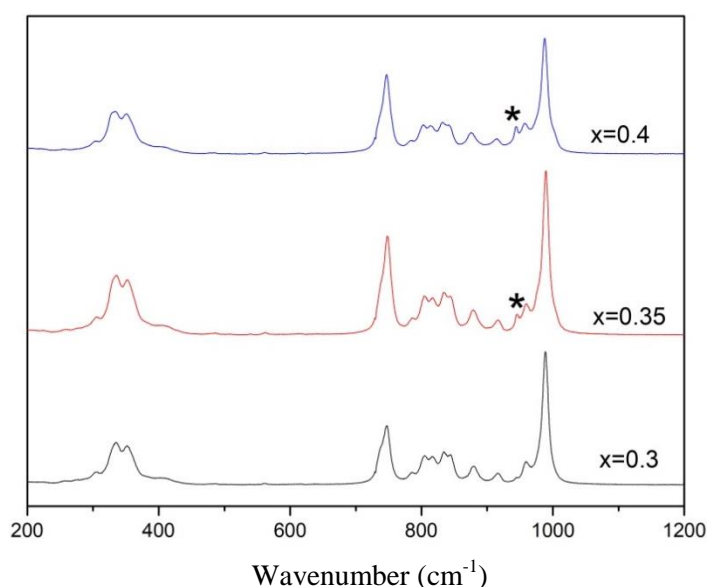


**Figure 34-** Raman spectra of  $\text{ZrMg}_{1-x}\text{Zn}_x\text{Mo}_3\text{O}_{12}$ , where  $x=0.3, 0.35$  and  $0.4$ . (\*) Represents the peak of  $\text{ZnMoO}_4$  phase.

For the  $\text{ZrMg}_{0.9}\text{Ni}_{0.1}\text{Mo}_3\text{O}_{12}$  system (Figure 35), Raman spectrum is very similar to the  $\text{ZrMgMo}_3\text{O}_{12}$  phase spectrum. Nevertheless, for  $\text{ZrMg}_{0.8}\text{Ni}_{0.2}\text{Mo}_3\text{O}_{12}$  phase, it can be observed the formation of another phase, such as  $\text{NiMoO}_4$  [97] by the appearance of the band around  $560\text{ cm}^{-1}$  and  $945\text{ cm}^{-1}$ .

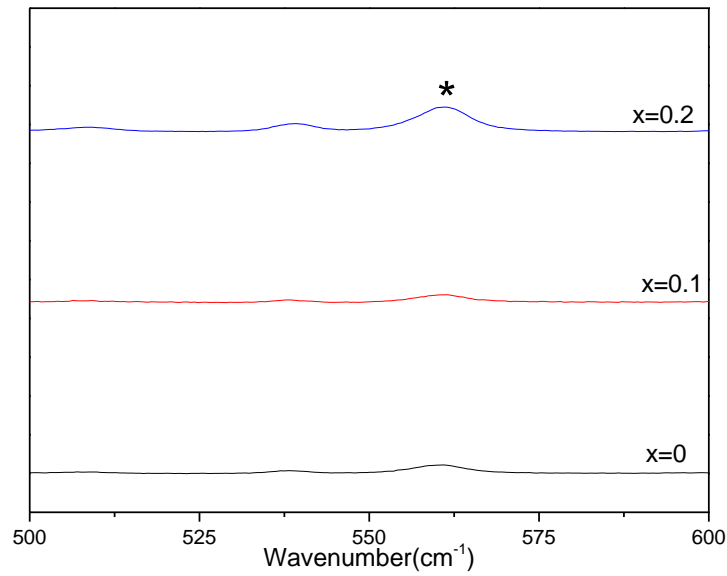


**Figure 35-** Raman spectrum of  $\text{ZrMg}_{1-x}\text{Ni}_x\text{Mo}_3\text{O}_{12}$ , where  $x=0, 0.1$  and  $0.2$ . (\*) Represents the peak of  $\text{NiMoO}_4$ .

These peaks are related to the  $\text{NiMoO}_4$  monoclinic crystalline phase [97]. As could be seen through XRPD measurements, the  $x = 0.2$  phase does not constitute a monophasic crystalline system, since it presents XRPD peaks indexed for secondary crystalline phase. In this way, Raman spectra corroborate the XRPD analysis for  $\text{ZrMg}_{0.9}\text{Ni}_{0.1}\text{Mo}_3\text{O}_{12}$  system.

## 6

### Conclusions and future works

1. Two new crystalline systems  $\text{ZrMg}_{1-x}\text{Zn}_x\text{Mo}_3\text{O}_{12}$  ( $x=0.1, 0.3, 0.35, 0.4$ ) and  $\text{ZrMg}_{1-x}\text{Zn}_x\text{Mo}_3\text{O}_{12}$  ( $x=0.05, 0.1, 0.15$ ) were successfully synthesized by solid state reaction.
2. An attempt to synthesize  $\text{ZrZnMo}_3\text{O}_{12}$  phase was not successful and the final product was a mixture of hexagonal  $\text{ZrMo}_2\text{O}_8$  and monoclinic  $\text{ZnMoO}_4$ , as observed by XRPD. The same attempt was applied for  $\text{ZrNiMo}_3\text{O}_{12}$ , which presented as two phases  $\text{ZrMo}_2\text{O}_8$  (trigonal) and  $\text{NiMoO}_4$  (monoclinic). Thus, both phases are not thermodynamically stable.
3. The solubility of  $\text{Zn}^{2+}$  and  $\text{Ni}^{2+}$  in  $\text{ZrMgMo}_3\text{O}_{12}$ , at room temperature, was established by XRPD, where the diffraction patterns were adjusted by Le Bail method. The solubility limit was  $0.35 \leq x \leq 0.4$  and  $0.1 \leq x \leq 0.2$ , respectively. With the increment of  $\text{Zn}^{2+}$  or  $\text{Ni}^{2+}$  ions in composition, phases such as  $\text{ZnMoO}_4$  and  $\text{NiMoO}_4$  were formed.
4. For all compositions, the phase transition temperature were established (monoclinic structure to orthorhombic structure), presenting values below room temperature. Thus, they can be considered as excellent potential materials for thermal shock resistance.
5. The orthorhombic phases obtained in this work do not present hygroscopicity, then, transversal motions are possible between the polyhedra, allowing near to zero CTE, as already reported for  $\text{ZrMgMo}_3\text{O}_{12}$
6. In the range from 373 up to 973 K,  $\text{ZrMg}_{0.7}\text{Zn}_{0.3}\text{Mo}_3\text{O}_{12}$  phase showed a near-zero thermal expansion  $\alpha_l=7.80 \times 10^{-7} \text{K}^{-1}$ . In spite of  $x = 0.4$  is a multiphasic material ( $\text{ZrMo}_2\text{O}_8$  and  $\text{ZnMoO}_4$ ), CTE was also near to zero  $\alpha_l=7.70 \times 10^{-7} \text{K}^{-1}$ . At lower temperatures (173-298 K),  $\text{ZrMg}_{0.9}\text{Zn}_{0.1}\text{Mo}_3\text{O}_{12}$  phase presented the same behavior, with  $\alpha_l=2.82 \times 10^{-7} \text{K}^{-1}$ .
7. The band-gap energy, calculated by the Kubelka-Munk equation, did not showed remarkable differences in their values with the increase of  $\text{Zn}^{2+}$  in the  $\text{ZrMg}_{1-x}\text{Zn}_x\text{Mo}_3\text{O}_{12}$  system. On the other hand, the increase of  $\text{Ni}^{2+}$  in the

8.  $\text{ZrMg}_{1-x}\text{Ni}_x\text{Mo}_3\text{O}_{12}$  system caused the decrease of the band-gap energy by a possible interaction between “d” orbitals of  $\text{Ni}^{2+}$  and “p” orbitals of oxygen.
9. The Raman spectrum evidenced the low homogeneity of the phases when the composition of the metal increases. This spectroscopy corroborated the presence of secondary phases, previously established by XRPD of  $\text{ZrMg}_{1-x}\text{Ni}_x\text{Mo}_3\text{O}_{12}$  system. Nevertheless, for the  $\text{ZrMg}_{0.65}\text{Zn}_{0.35}\text{Mo}_3\text{O}_{12}$  system was identified the  $\text{ZnMoO}_4$  phase, which was not determined by XRPD.
10. CTEs were obtained by XRPD at high temperatures measurements only for three proposed phases, due to inconveniences with the XRPD equipment. CTE measurements for the other phases, which were not analyzed in this study, will be performed as soon as possible.
11. For future works, the synthesis of these materials by ball mill is being proposed, in order to obtain a better homogeneity degree. In addition, a study of the coefficients of thermal expansion by the dilatometry technique (to compare with the results obtained by XRPD, in high and low temperatures) will be performed. A refinement by Rietveld method, in order to know specific data of the as-synthesized crystalline structure is also a future goal.

## 7 References

- [1] R. Martin, ten things you need to know about infrared windows, *Infrared Window*. **25** (2009) 1–42. doi:10.1006/jssc.1998.7744.
- [2] C.P. Romao, F.A. Perras, U. Werner-Zwanziger, J.A. Lussier, K.J. Miller, C.M. Calahoo, J.W. Zwanziger, M. Bieringer, B.A. Marinkovic, D.L. Bryce, M.A. White, Zero thermal expansion in  $\text{ZrMgMo}_3\text{O}_{12}$ : NMR crystallography reveals origins of thermoelastic properties, *Chemistry of Materials*. **27** (2015) 2633–2646. doi:10.1021/acs.chemmater.5b00429.
- [3] W.B. Song, E.J. Liang, X.S. Liu, Z.Y. Li, B.H. Yuan, J.Q. Wang, A negative thermal expansion material of  $\text{ZrMgMo}_3\text{O}_{12}$ , *Chinese Physics Letters*. **30** (2013) 0–4. doi:10.1088/0256-307X/30/12/126502.
- [4] M. Ari, P.M. Jardim, B.A. Marinkovic, F. Rizzo, F.F. Ferreira, Thermal expansion of  $\text{Cr}_2\text{xFe}_{2-2\text{x}}\text{Mo}_3\text{O}_{12}$ ,  $\text{Al}_2\text{xFe}_{2-2\text{x}}\text{Mo}_3\text{O}_{12}$  and  $\text{Al}_2\text{xCr}_{2-2\text{x}}\text{Mo}_3\text{O}_{12}$  solid solutions, *Journal of Solid State Chemistry*. **181** (2008) 1472–1479. doi:10.1016/j.jssc.2008.03.015.
- [5] T. Properties, Specific properties, definitions and applications **8** (2003.) 453–483.
- [6] Barsoum M. W, *Fundamentals of ceramics*, 2003. doi:10.1016/0014-**299** (90)90648-P.
- [7] C.B.C. and M.G. Norton, *Ceramic Material Science and Engineering* Springer 2007, **2** (2007) 712. doi:10.1006/jssc.1998.7744.
- [8] G. Cunningham, K. Leveno, *Dilatacion*, *Williams Obstetricia*. (2010) 544.
- [9] A.W. Sleight, L.H. Brixner, A New Ferroelastic Transition in some  $\text{A}_2\text{M}_3\text{O}_{12}$  molybdates and Tungstates, **74** (1973) 172–174.
- [10] G.D. Barrera, J.A.O. Bruno, T.H.K. Barron, N.L. Allan, Negative thermal expansion, *Journal of Physics Condensed Matter*. **17** (2005). doi:10.1088/0953-8984/17/4/R03.
- [11] J.S.O. Evans, T.A. Mary, A.W. Sleight, Negative Thermal Expansion in  $\text{Sc}_2(\text{WO}_4)_3$ , *Journal of Solid State Chemistry*. **137** (1998) 148–160.

doi:10.1006/jssc.1998.7744.

- [12] C.P. Romao, K.J. Miller, C.A. Whitman, M.A. White, B.A. Marinkovic, Negative Thermal Expansion (Thermomiotic) Materials, Elsevier Ltd., **23** (2013). doi:10.1016/B978-0-08-097774-4.00425-3.
- [13] A. Mathew, Lattice Vibrations – Phonons in Solid State, Workshop on Advanced Topics in Semiconductor Devices. **12** (2006) 1–3. [http://www.ece.rochester.edu/courses/ECE423/ECE223\\_423\\_MSC426Workshop06/term papers 06/Mathew\\_06.pdf](http://www.ece.rochester.edu/courses/ECE423/ECE223_423_MSC426Workshop06/term%20papers%2006/Mathew_06.pdf).
- [14] B.A. Marinkovic, M. Ari, P.M. Jardim, R.R. de Avillez, F. Rizzo, F.F. Ferreira, In<sub>2</sub>Mo<sub>3</sub>O<sub>12</sub>: A low negative thermal expansion compound, *Thermochimica Acta*. **49** (2010) 48–53. doi:10.1016/j.tca.2009.10.021.
- [15] B.A. Marinkovic, M. Ari, R.R. De Avillez, F. Rizzo, F.F. Ferreira, K.J. Miller, M.B. Johnson, M.A. White, Correlation between AO<sub>6</sub> polyhedral distortion and negative thermal expansion in orthorhombic Y<sub>2</sub>Mo<sub>3</sub>O<sub>12</sub> and related materials, *Chemistry of Materials*. **21** (2009) 2886–2894. doi:10.1021/cm900650c.
- [16] W. Miller, C.W. Smith, D.S. MacKenzie, K.E. Evans, Negative thermal expansion: A review, *Journal of Materials Science*. **44** (2009) 5441–5451. doi:10.1007/s10853-009-3692-4.
- [17] W.F. Krupke, M.D. Shinn, J.E. Marion, J.A. Caird, S.E. Stokowski, Spectroscopic , optical , and thermomechanical properties of gadolinium scandium gallium garnet, *J.Opt.Soc.Am.B*. **3** (1986) 102–114.
- [18] C.A. Kennedy, M.A. White, A.P. Wilkinson, T. Varga, Low thermal conductivity of the negative thermal expansion material, HfMo<sub>2</sub>O<sub>8</sub>, *Applied Physics Letters*. **90** (2007) 2005–2008. doi:10.1063/1.2721860.
- [19] K.J. Miller, M.B. Johnson, M.A. White, B.A. Marinkovic, Low-temperature investigations of the open-framework material HfMgMo<sub>3</sub>O<sub>12</sub>, *Solid State Communications*. **15** (2012) 1748–1752. doi:10.1016/j.ssc.2012.06.022.
- [20] L. Young, P.T. Alvarez, H. Liu, C. Lind, Extremely Low Temperature Crystallization in the A<sub>2</sub>M<sub>3</sub>O<sub>12</sub> Family of Negative Thermal Expansion Materials, *European Journal of Inorganic Chemistry*. **26** (2016) 1251–1256. doi:10.1002/ejic.201501420.
- [21] A. Pryde, M.T. Dove, V. Heine, Simulation studies of ZrW<sub>2</sub>O<sub>8</sub> at high

- pressure, *Journal of Physics Condensed Matter*. **10** (1998) 8417–8428. doi:10.1088/0953-8984/10/38/004.
- [22] V. Korthuis, N. Khosrovani, A.W. Sleight, N. Roberts, R. Dupree, W.W. Warren, Negative Thermal Expansion and Phase Transitions in the  $ZrV_2-xPxO_7$  Series, *Chemistry of Materials*. **7** (1995) 412–417. doi:10.1021/cm00050a028.
- [23] J.S.O. Evans, T.A. Mary, A.W. Sleight, Negative Thermal Expansion in a Large Molybdate and Tungstate Family, **583** (1997) 580–583. doi:10.1126/science.275.5296.61.
- [24] C. Lind, Two Decades of Negative Thermal Expansion Research: Where do we stand?, *Materials*. **5** (2012) 1125–1154. doi:10.3390/ma5061125.
- [25] M. Ari, K.J. Miller, B.A. Marinkovic, P.M. Jardim, R. De Avillez, F. Rizzo, M.A. White, Rapid synthesis of the low thermal expansion phase of  $Al_2Mo_3O_{12}$  via a sol-gel method using polyvinyl alcohol, *Journal of Sol-Gel Science and Technology*. **58** (2011) 121–125. doi:10.1007/s10971-010-2364-9.
- [26] R. Truitt, I. Hermes, A. Main, A. Sendeki, C. Lind, Low temperature synthesis and characterization of  $AlScMo_3O_{12}$ , *Materials*. **8** (2015) 700–716. doi:10.3390/ma8020700.
- [27] B.A. Marinkovic, P.M. Jardim, M. Ari, R.R. De Avillez, F. Rizzo, F.F. Ferreira, Low positive thermal expansion in  $HfMgMo_3O_{12}$ , *Physica Status Solidi (B) Basic Research*. **245** (2008) 2514–2519. doi:10.1002/pssb.200880262.
- [28] S. Sumithra, A.M. Umarji, Hygroscopicity and bulk thermal expansion in  $Y_2W_3O_{12}$ , *Materials Research Bulletin*. **40** (2005) 167–176. doi:10.1016/j.materresbull.2004.09.009.
- [29] B.A. Marinkovic, P.M. Jardim, R.R. De Avillez, F. Rizzo, Negative thermal expansion in  $Y_2Mo_3O_{12}$ , *Solid State Sciences*. **7** (2005) 1377–1383. doi:10.1016/j.solidstatesciences.2005.08.012.
- [30] A.K. Tyagi, S.N. Achary, M.D. Mathews, Phase transition and negative thermal expansion in  $A_2(MoO_4)_3$  system ( $A = Fe^{3+}$ ,  $Cr^{3+}$  and  $Al^{3+}$ ), *Journal of Alloys and Compounds*. **339** (2002) 207–210. doi:10.1016/S0925-8388(01)02003-5.
- [31] T. Suzuki, A. Omote, Negative thermal expansion of a interesting material,

- 137** (2004) 3–4. doi:10.1006/jssc.1998.7744.
- [32] Y. Cheng, Y. Liang, Y. Mao, X. Ge, B. Yuan, J. Guo, M. chao, E. Liang, A novel material of HfScW<sub>2</sub>PO<sub>12</sub> with negative thermal expansion from 140 K to 1469 K and intense blue photoluminescence, *Materials Research Bulletin*. **85** (2017) 176–180. doi:10.1016/j.materresbull.2016.09.008.
- [33] A. Omote, S. Yotsuhashi, Y. Zenitani, Y. Yamada, High ion conductivity in MgHfW<sub>3</sub>O<sub>12</sub> solids with ordered structure:1-D Alignments of Mg<sup>2+</sup> and Hf<sup>4+</sup> ions, *American Ceramic Society*. **2288** (2011) 2285–2288. doi:10.1111/j.1551-2916.2011.04644.x.
- [34] B. Steele, H. and Angelika, *Materials for fuel-cell technologies*, *Insight Review Articles*. 414 (2001) 345–352.
- [35] T. Li, X. Ge, X. Liu, Y. Cheng, Y. Liu, H. Yuan, S. Li, Y. Liu, J. Guo, Q. Sun, Y. Li, E. Liang, Enhanced negative thermal expansion by solid solution of HfMgMo<sub>1.5</sub>W<sub>1.5</sub>O<sub>12</sub>, *Materials Express*. **6** (2016) 515–520. doi:10.1166/mex.2016.1337.
- [36] D.A. Woodcock, P. Lightfoot, C. Ritter, Negative thermal expansion in Y<sub>2</sub>(WO<sub>4</sub>)<sub>3</sub>, *Journal of Solid State Chemistry*. **149** (2000) 92–98. doi:10.1006/jssc.1999.8502.
- [37] E. Makovicky, T. Balić-Žunić, New Measure of Distortion for Coordination Polyhedra, *Acta Crystallographica Section B: Structural Science*. **54** (1998) 766–773. doi:10.1107/S0108768198003905.
- [38] T.A. Mary, J.S. Evans, T. Vogt, A.W. Sleight, Negative Thermal Expansion from 0 . 3 to 1050 Kelvin in ZrW<sub>20</sub>O<sub>8</sub>, *Science*. **272** (1996) 90–92.
- [39] M.T. Dove, H. Fang, Negative thermal expansion and associated anomalous physical properties: Review of the lattice dynamics theoretical foundation, *Reports on Progress in Physics*. **79** (2016) 66503. doi:10.1088/0034-4885/79/6/066503.
- [40] C.P. Romao, S.P. Donegan, J.W. Zwanziger, M.A. White, Relationships between elastic anisotropy and thermal expansion in A<sub>2</sub>Mo<sub>3</sub>O<sub>12</sub>materials, *Physical Chemistry Chemical Physics*. **18** (2016) 30652–30661. doi:10.1039/c6cp06356j.
- [41] L.P. Prisco, P.I. Pontón, M. V. Guamán, R.R. Avillez, C.P. Romao, M.B. Johnson, M.A. White, B.A. Marinkovic, Assessment of the Thermal Shock

- Resistance Figures of Merit of Al<sub>2</sub>W<sub>3</sub>O<sub>12</sub>, a Low Thermal Expansion Ceramic, *Journal of the American Ceramic Society*. **99** (2016) 1742–1748. doi:10.1111/jace.14160.
- [42] L.P. Prisco, C.P. Romao, F. Rizzo, M.A. White, B.A. Marinkovic, The effect of microstructure on thermal expansion coefficients in powder-processed Al<sub>2</sub>Mo<sub>3</sub>O<sub>12</sub>, *Journal of Materials Science*. **48** (2013) 2986–2996. doi:10.1007/s10853-012-7076-9.
- [43] R. Allada, A. Maruthapillai, K. Palanisamy, P. Chappa, Hygroscopicity Categorization of pharmaceutical solids by gravimetric sorption analysis: A systematic approach, *Asian Journal of Pharmaceutics*. **10** (2016) 279–286.
- [44] M.Y. Wu, Y. Jia, Q. Sun, Effects of A<sup>3+</sup> cations on hydration in A<sub>2</sub>M<sub>3</sub>O<sub>12</sub> family materials: A first-principles study, *Computational Materials Science*. **111** (2016) 28–33. doi:10.1016/j.commatsci.2015.09.010.
- [45] R. Shannon, M. H, N.H. Baur, O.H. Gibbs, M. Eu, V. Cu, Revised effective ionic radii and systematic studies of interatomic distances in halides and chalcogenides, *Act. Cryst.* (1976).
- [46] W. Paraguassu, M. Maczka, A.G.S. Filho, P.T.C. Freire, F.E.A. Melo, J.M. Filho, J. Hanuza, A comparative study of negative thermal expansion materials Sc<sub>2</sub>(MoO<sub>4</sub>)<sub>3</sub> and Al<sub>2</sub>(WO<sub>4</sub>)<sub>3</sub> crystals, *Vibrational Spectroscopy*. **44** (2007) 69–77. doi:10.1016/j.vibspec.2006.08.006.
- [47] S. Block, E.M. Levin, Structural Interpretation of Immiscibility in Oxide Systems: II, Coordination Principles Applied to Immiscibility, *Journal of the American Ceramic Society*. **40** (1957) 113–118. doi:10.1111/j.1151-2916.1957.tb12586.x.
- [48] S. Li, X. Ge, H. Yuan, D. Chen, J. Guo, R. Shen, M. Chao, E. Liang, Near-zero thermal expansion and phase transitions in HfMg<sub>1-x</sub>Zn<sub>x</sub>Mo<sub>3</sub>O<sub>12</sub>, *Frontiers in Chemistry*. **6** (2018) 1–9. doi:10.3389/fchem.2018.00115.
- [49] E. LARA-CURZIO, Properties of CVI–SiC Matrix Composites, *Comprehensive Composite Materials*. **22** (2004) 533–577. doi:10.1016/b0-08-042993-9/00112-1.
- [50] G.S. Upadhyaya, Thermal Shock Resistance, Cemented Tungsten Carbides. **28** (2008) 249–253. doi:10.1016/b978-081551417-6.50011-3.
- [51] D.C. Harris, *Materials for Infrared Windows and Domes*, **29** (1999).

- doi:10.1117/3.349896.
- [52] W.R.C. M.J.M. John B.Wachtman, Mechanical properties of ceramics, **29** (2009).
- [53] D.C. Harris, L. Cambrea, Assessment of low-expansion tungstates for thermal-shock-resistant infrared windows, Window and Dome Technologies and Materials XIII. **8708** (2013) 870809. doi:10.1117/12.2014815.
- [54] M.A. White, A.J. Avery, M.W. Vernon, Physical Properties of Materials, **14** (2012). doi:10.1007/978-94-011-6065-0.
- [55] M.V. Swain, Brittle Materials: Thermal Shock, Encyclopedia of Materials: Science and Technology. **58** (2004) 825–828. doi:10.1016/b0-08-043152-6/00158-3.
- [56] M. Aarchiba, Aecis, Aldousleung. Alex Selby, Induction cooking and important applications **12** (2014) 1–13.
- [57] S. Villacís, J. Martínez, A.J. Riofrío, D.F. Carrión, M.A. Orozco, D. Vaca, Energy Efficiency Analysis of Different Materials for Cookware Commonly Used in Induction Cookers, Energy Procedia. **75** (2015) 925–930. doi:10.1016/j.egypro.2015.07.252.
- [58] J. P.F, Glass Ceramics: New Compositions and Uses, Journal of Non-Crystalline Solids. **181** (1995) 1–15.
- [59] C.P. Romao, F.A. Perras, U. Werner-Zwanziger, J.A. Lussier, K.J. Miller, C.M. Calahoo, J.W. Zwanziger, M. Bieringer, B.A. Marinkovic, D.L. Bryce, M.A. White, Zero thermal expansion in ZrMgMo<sub>3</sub>O<sub>12</sub>: NMR crystallography reveals origins of thermoelastic properties, Chemistry of Materials. **27** (2015) 2633–2646. doi:10.1021/acs.chemmater.5b00429.
- [60] S. Allen, R.J. Ward, M.R. Hampson, R.K.B. Gover, J.S.O. Evans, Structures and phase transitions of trigonal ZrMo<sub>2</sub>O<sub>8</sub> and HfMo<sub>2</sub>O<sub>8</sub>, Acta Crystallographica Section B: Structural Science. **60** (2004) 32–40. doi:10.1107/S0108768103025138.
- [61] M. Auray, M. Quarton, P. Tarte, New structure of high-temperature zirconium molybdate, Acta Crystallographica Section C Crystal Structure Communications. **42** (1986) 257–259. doi:10.1107/s0108270186096579.
- [62] M. Auray, M. Quarton, P. Tarte, Crystal Data for Two Molybdates MIV (MoO<sub>4</sub>)<sub>2</sub> With MIV = Zr, Hf, Powder Diffraction. **2** (1987) 36–38.

- doi:10.1017/S0885715600012215.
- [63] P.P. Sahoo, S. S., G. Madras, T.N. Guru Row, Synthesis, Characterization, and Photocatalytic Properties of  $ZrMo_2O_8$ , *The Journal of Physical Chemistry C*. **113** (2009) 10661–10666. doi:10.1021/jp901897s.
- [64] C. Lind, D.G. Vanderveer, A.P. Wilkinson, J. Chen, M.T. Vaughan, D.J. Weidner, Lind, Cora, et al. “New high-pressure form of the negative thermal expansion materials zirconium molybdate and hafnium molybdate.” *Chemistry of materials* **13.2** (2001): 487-490., (2001) 487–490.
- [65] J. Yang, Z. Liu, Y. Shi, M. Li, M. Yang, E. Liang, Investigation on the synthesis and the mechanical and thermal expansion properties of  $ZrMgMo_3O_{12}$  ceramic bodies, *Ceramics International*. **45** (2019) 8750–8760. doi:10.1016/j.ceramint.2019.01.199.
- [66] L.S. Cavalcante, J.C. Sczancoski, M. Siu Li, E. Longo, J.A. Varela,  $\beta$ - $ZnMoO_4$  microcrystals synthesized by the surfactant-assisted hydrothermal method: Growth process and photoluminescence properties, *Colloids and Surfaces A: Physicochemical and Engineering Aspects*. **396** (2012) 346–351. doi:10.1016/j.colsurfa.2011.12.021.
- [67] W. Reichelt, T. Weber, T. So, È. Die, È. Kanten, Mischkristallbildung im System  $CuMoO_4/ZnMoO_4$ , **4** (2002). doi:10.1006/jssc.1998.7744.
- [68] R. Zăvoianu, C.R. Dias, A.P.V. Soares, M.F. Portela, Oxidative dehydrogenation of i-butane over nanostructured silica-supported  $NiMoO_4$  catalysts with low content of active phase, *Applied Catalysis A: General*. **298** (2006) 40–49. doi:10.1016/j.apcata.2005.09.017.
- [69] C. Mazzocchia, C. Aboumrar, C. Diagne, E. Tempesti, J.M. Herrmann, G. Thomas, On the  $NiMoO_4$  oxidative dehydrogenation of propane to propene: some physical correlations with the catalytic activity, *Catalysis Letters*. **10** (1991) 181–191. doi:10.1007/BF00772070.
- [70] M. Cetinkol, A.P. Wilkinson, P.L. Lee, Structural changes accompanying negative thermal expansion in  $Zr_2(MoO_4)(PO_4)_2$ , *Journal of Solid State Chemistry*. **182** (2009) 1304–1311. doi:10.1016/j.jssc.2009.02.029.
- [71] L.P. Prisco, P.I. Pontón, W. Paraguassu, C.P. Romao, M.A. White, B.A. Marinkovic, Near-zero thermal expansion and phase transition in  $In_{0.5}(ZrMg)_{0.75}Mo_3O_{12}$ , *Journal of Materials Research*. **31** (2016) 3240–

3248. doi:10.1557/jmr.2016.329.
- [72] J.S.O. Evans, T.A. Mary, A.W. Sleight, Negative Thermal Expansion in a Large Molybdate and Tungstate Family, **583** (1997) 580–583.
- [73] A.M. Gindhart, C. Lind, M. Green, Polymorphism in the negative thermal expansion material magnesium hafnium tungstate, (2008). doi:10.1557/JMR.2008.0013.
- [74] I.M. Costa, V.L. Blair, W. Paraguassu, B.A. Marinkovic, Evaluating Al<sub>2</sub>-xGa<sub>x</sub>W<sub>3</sub>O<sub>12</sub> system for thermal shock resistance, *Journal of Solid State Chemistry*. **277** (2019) 149–158. doi:10.1016/j.jssc.2019.05.041.
- [75] T. Li, X.-S. Liu, Y.-G. Cheng, X.-H. Ge, M.-D. Zhang, H. Lian, Y. Zhang, E.-J. Liang, Y.-X. Li, Zero and controllable thermal expansion in HfMgMo<sub>3-x</sub>W<sub>x</sub>O<sub>12</sub>, *Chinese Physics B*. **26** (2017) 016501. doi:10.1088/1674-1056/26/1/016501.
- [76] D. Chen, B. Yuan, Y. Cheng, X. Ge, Y. Jia, E. Liang, M. Chao, Phase transition and near-zero thermal expansion in ZrFeMo<sub>2</sub>VO<sub>12</sub>, *Physics Letters A*. **380** (2016) 4070–4074. doi:10.1016/j.physleta.2016.10.009.
- [77] S. Li, X. Ge, H. Yuan, D. Chen, J. Guo, R. Shen, M. Chao, E. Liang, Near-Zero Thermal Expansion and Phase Transitions in HfMg<sub>1-x</sub>Zn<sub>x</sub>Mo<sub>3</sub>O<sub>12</sub>, *Frontiers in Chemistry*. **6** (2018) 1–9. doi:10.3389/fchem.2018.00115.
- [78] C.P. Romao, F. a. Perras, U. Werner-Zwanziger, J. a. Lussier, K.J. Miller, C.M. Calahoo, J.W. Zwanziger, M. Bieringer, B. a. Marinkovic, D.L. Bryce, M.A. White, Zero Thermal Expansion in ZrMgMo<sub>3</sub>O<sub>12</sub>: NMR Crystallography Reveals Origins of Thermoelastic Properties, *Chemistry of Materials*. **27** (2015) 2633–2646. doi:10.1021/acs.chemmater.5b00429.
- [79] N. Duan, U. Kameswari, A.W. Sleight, Further contraction of ZrW<sub>2</sub>O<sub>8</sub> [9], *Journal of the American Chemical Society*. **121** (1999) 10432–10433. doi:10.1021/ja992569+.
- [80] S. Sumithra, A.M. Umarji, Role of crystal structure on the thermal expansion of Ln<sub>2</sub>W<sub>3</sub>O<sub>12</sub> (Ln = La, Nd, Dy, Y, Er and Yb), *Solid State Sciences*. **6** (2004) 1313–1319. doi:10.1016/j.solidstatesciences.2004.07.023.
- [81] R. López, R. Gómez, Band-gap energy estimation from diffuse reflectance measurements on sol-gel and commercial TiO<sub>2</sub>: A comparative study, *Journal of Sol-Gel Science and Technology*. **61** (2012) 1–7.

- doi:10.1007/s10971-011-2582-9.
- [82] H. jun ZHANG, Q. ZHANG, Q. li JIA, G. tian YE, Preparation of Al<sub>2-x</sub>Y<sub>x</sub>W<sub>3</sub>O<sub>12</sub> powders by citrate sol-gel process, Transactions of Nonferrous Metals Society of China (English Edition). **18** (2008) 1112–1116. doi:10.1016/S1003-6326(08)60190-9.
- [83] J. Zhu, J. Yang, X. Cheng, Synthesis and tunable thermal expansion property of Al<sub>2-δ</sub>Sc<sub>δ</sub>W<sub>3</sub>O<sub>12</sub>, Solid State Sciences. **14** (2012) 187–190. doi:10.1016/j.solidstatesciences.2011.11.023.
- [84] E. Morgado, B.A. Marinkovic, P.M. Jardim, M.A.S. de Abreu, F.C. Rizzo, Characterization and thermal stability of cobalt-modified 1-D nanostructured trititanates, Journal of Solid State Chemistry. **182** (2009) 172–181. doi:10.1016/j.jssc.2008.10.008.
- [85] E. Morgado, B.A. Marinkovic, P.M. Jardim, M.A.S. De Abreu, M.D.G.C. Rocha, P. Bargiela, Studies on Fe-modified nanostructured trititanates, Materials Chemistry and Physics. **126** (2011) 118–127. doi:10.1016/j.matchemphys.2010.11.054.
- [86] T. Nishikawa, T. Nakajima, Y. Shinohara, An exploratory study on effect of the isomorphic replacement of Ti<sup>4+</sup> ions by various metal ions on the light absorption character of TiO<sub>2</sub>, Journal of Molecular Structure: THEOCHEM. **545** (2001) 67–74. doi:10.1016/S0166-1280(01)00394-3.
- [87] B.C. Windom, W.G. Sawyer, D.W. Hahn, A raman spectroscopic study of MoS<sub>2</sub> and MoO<sub>3</sub>: Applications to tribological systems, Tribology Letters. **42** (2011) 301–310. doi:10.1007/s11249-011-9774-x.
- [88] M. Dieterle, G. Mestl, Raman spectroscopy of molybdenum oxides: Part II. Resonance Raman spectroscopic characterization of the molybdenum oxides Mo<sub>4</sub>O<sub>11</sub> and MoO<sub>2</sub>, Physical Chemistry Chemical Physics. **4** (2002) 822–826. doi:10.1039/b107046k.
- [89] a P. Naumenko, N.I. Berezovska, M.M. Biliy, O. V Shevchenko, Vibrational analysis and Raman spectra of tetragonal Zirconia, Phys. Chem. Solid State. **9** (2008) 121–125.
- [90] A.J. Bauer, ZrO<sub>2</sub> Phase Identification with Raman Spectroscopy, **12** (2018) 4–7.
- [91] F. Monroy-Guzman, T. Rivero Gutiérrez, I.Z. López Malpica, S. Hernández Cortes, P. Rojas Nava, J.C. Vazquez Maldonado, A. Vazquez,

- Production optimization of  $^{99}\text{Mo}/^{99\text{m}}\text{Tc}$  zirconium molybdate gel generators at semi-automatic device: DISIGEG, *Applied Radiation and Isotopes*. **70** (2012) 103–111. doi:10.1016/j.apradiso.2011.09.017.
- [92] S.S. A K Bhunia, P K Jha, D Rout, Morphological Properties and Raman Spectroscopy of ZnO Nanorods, *Journal of Physical Science*. **21** (2016) 111–118.
- [93] J.Z. Marinho, F.C. Romeiro, S.C.S. Lemos, F. V. Motta, C.S. Riccardi, M.S. Li, E. Longo, R.C. Lima, Urea-Based Synthesis of Zinc Oxide Nanostructures at Low Temperature, *Journal of Nanomaterials*. **21** (2012) 1–7. doi:10.1155/2012/427172.
- [94] U. Eduok, J. Szpunar, Ultrasound-assisted synthesis of zinc molybdate nanocrystals and molybdate-doped epoxy/PDMS nanocomposite coatings for Mg alloy protection, *Ultrasonics Sonochemistry*. **44** (2018) 288–298. doi:10.1016/j.ultsonch.2018.02.036.
- [95] X.H. Ge, Y.C. Mao, L. Li, L.P. Li, N. Yuan, Y.G. Cheng, J. Guo, M.J. Chao, E.J. Liang, Phase Transition and Negative Thermal Expansion Property of  $\text{ZrMnMo}_3\text{O}_{12}$ , *Chinese Physics Letters*. **33** (2016) 0–4. doi:10.1088/0256-307X/33/4/046503.
- [96] E.J. Liang, Y. Liang, Y. Zhao, J. Liu, Y. Jiang, Low-Frequency Phonon Modes and Negative Thermal Expansion in  $\text{A}(\text{MO}_4)_2(\text{A} \text{ Zr, Hf and M} \text{ W, Mo})$  by Raman and Terahertz Time-Domain Spectroscopy, *J. Phys. Chem. A*. **2** (2008) 12582–12587.
- [97] A.P. De Moura, L.H. De Oliveira, I.L.V. Rosa, C.S. Xavier, P.N. Lisboa-Filho, M.S. Li, F.A. La Porta, E. Longo, J.A. Varela, Structural, optical, and magnetic properties of NiMoO nanorods prepared by microwave sintering, *Scientific World Journal*. **20** (2015). doi:10.1155/2015/315084.

## Appendix A: Supplementary material to support Chapter 5.

### A.1.

#### Coefficient of thermal expansion in low temperatures (173-298) K for $\text{ZrMgMo}_3\text{O}_{12}$ .

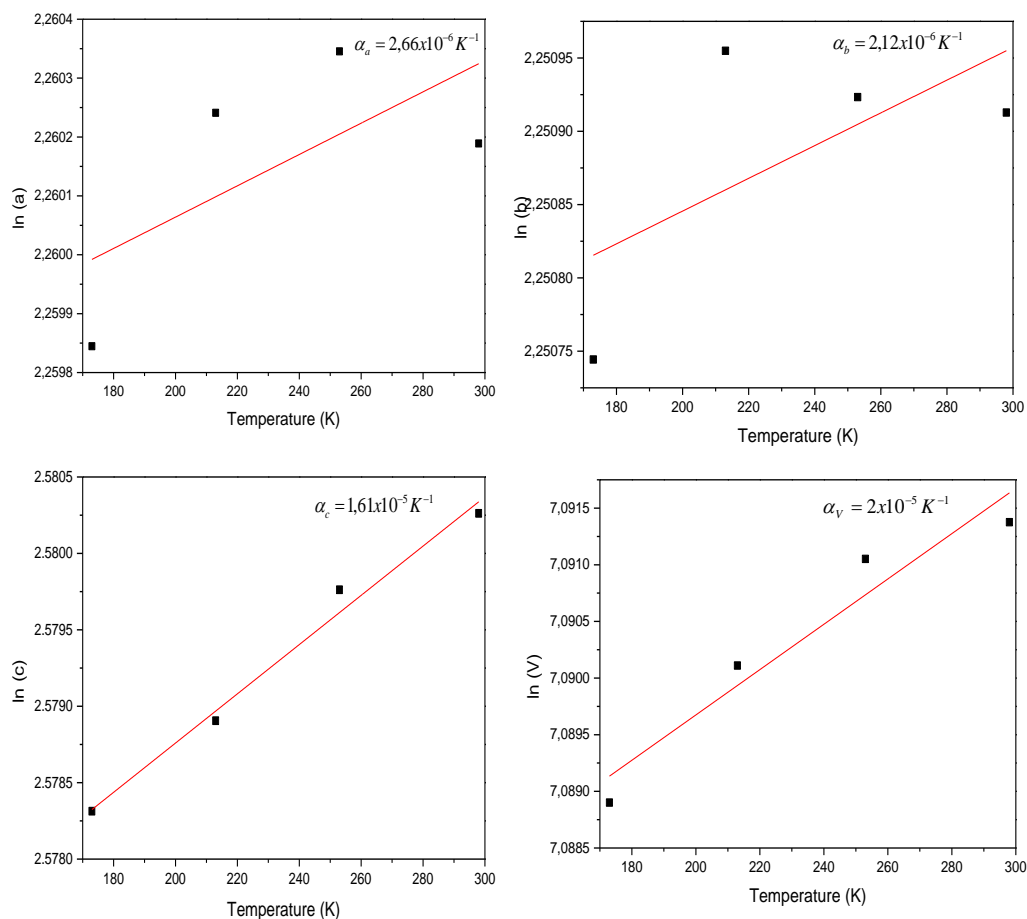


Figure A.1- Linear coefficients of thermal expansion for  $\text{ZrMgMo}_3\text{O}_{12}$  phase in three crystallographic directions and volumetric; a) a-axes, b) b-axes c) c-axes and d) Volume.  $\alpha_1 = 6,66 \times 10^{-6} \text{ K}^{-1}$ .

### A.2.

#### Coefficient of thermal expansion in high temperatures (373-397) K for $\text{ZrMg}_{0.6}\text{Zn}_{0.4}\text{Mo}_3\text{O}_{12}$ .

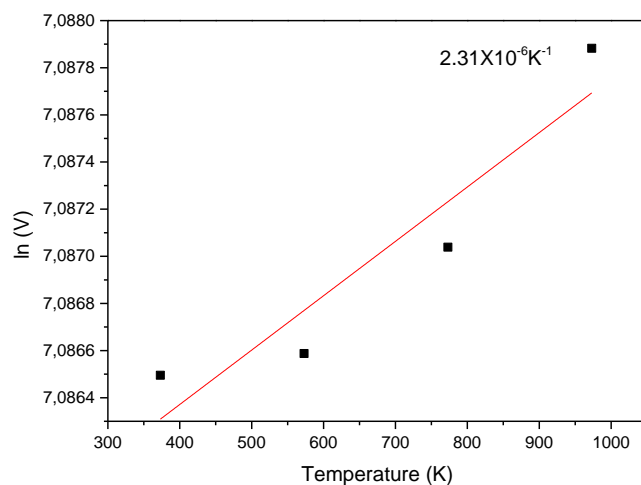


Figure A.2- Linear coefficients of thermal expansion for  $\text{ZrMg}_{0.6}\text{Zn}_{0.4}\text{Mo}_3\text{O}_{12}$  phase in the volumetric axe.  $\alpha_l = 7.7 \times 10^{-7} \text{K}^{-1}$

### A.3.

**Diffraction patterns for  $\text{ZrMg}_{0.85}\text{Ni}_{0.15}\text{Mo}_3\text{O}_{12}$  in low temperatures (298-173) K.**

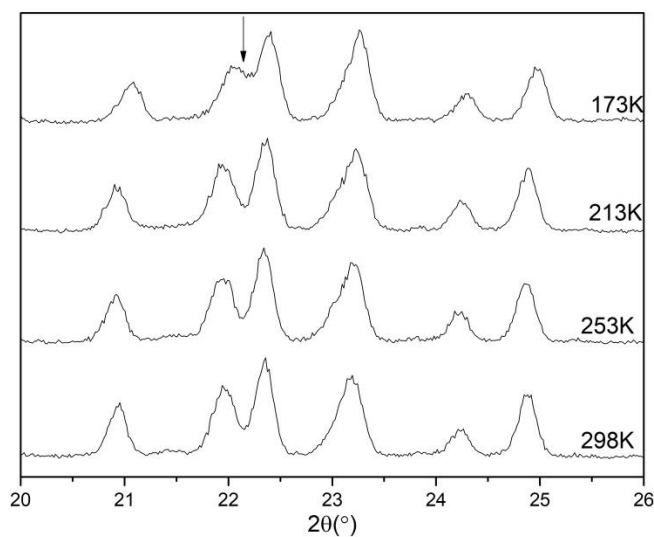
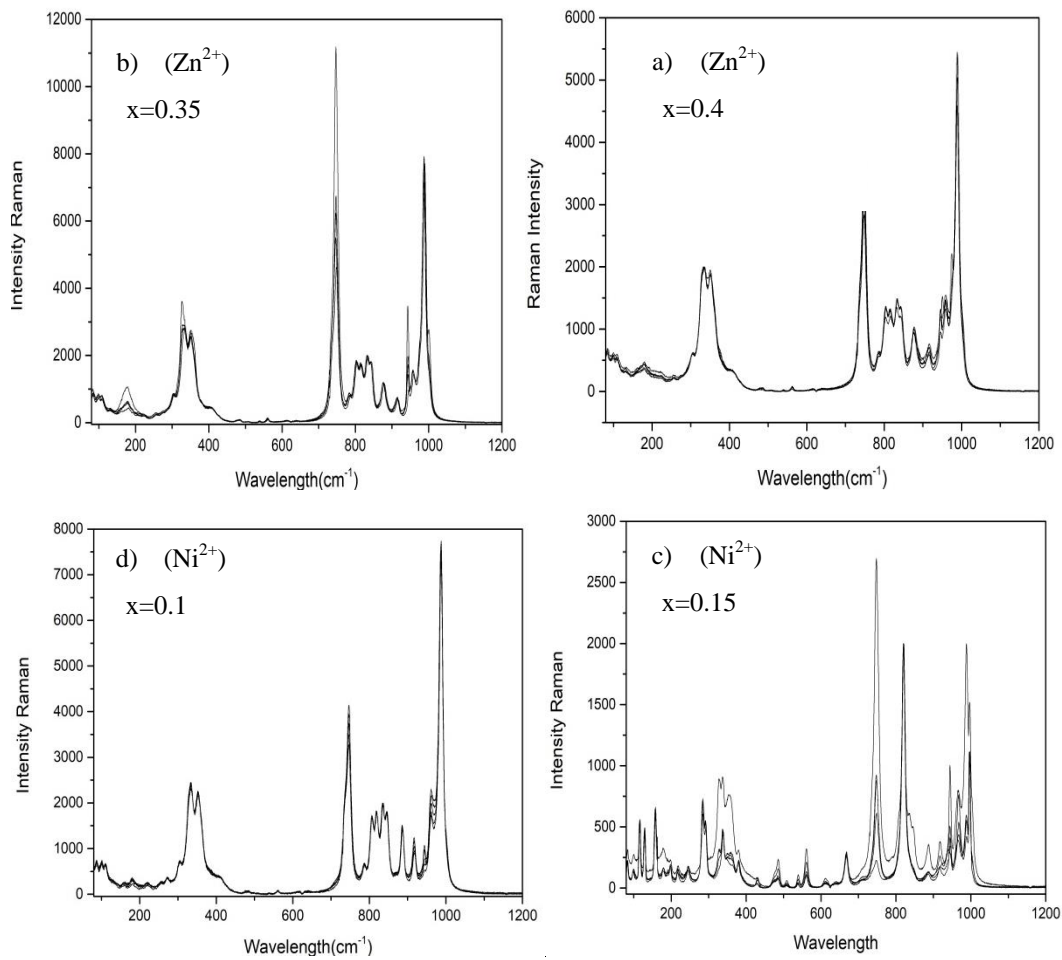


Figure A.3- Diffraction pattern lines for  $\text{ZrMg}_{0.85}\text{Ni}_{0.15}\text{Mo}_3\text{O}_{12}$  ( $\downarrow$ ) Characteristic pick which corresponds to the transition of monoclinic to orthorhombic structure by the division of peak at  $22^\circ$ - $22.5^\circ$  ( $2\theta$ ).

### A.4.

**Raman spectra for  $\text{ZrMg}_{1-x}\text{Zn}_x\text{Mo}_3\text{O}_{12}$  and  $\text{ZrMg}_{1-x}\text{Ni}_x\text{Mo}_3\text{O}_{12}$  systems.**



**Figure A.4-** Raman spectra for a)  $\text{ZrMg}_{0.65}\text{Zn}_{0.35}\text{Mo}_3\text{O}_{12}$ , b)  $\text{ZrMg}_{0.6}\text{Zn}_{0.4}\text{Mo}_3\text{O}_{12}$ , c)  $\text{ZrMg}_{0.9}\text{Ni}_{0.1}\text{Mo}_3\text{O}_{12}$  and d)  $\text{ZrMg}_{0.85}\text{Ni}_{0.15}\text{Mo}_3\text{O}_{12}$  systems with 5 scanning points.

**Appendix B: Publication generated from this research.**

- **Title:** Solubility limit of  $Zn^{2+}$  in low thermal expansion  $ZrMgMo_3O_{12}$  and its influence on phase transition temperature.

**Elsevier Editorial System (tm) for Ceramics International. CERI-S-19-09787 (QUALIS A1)**

Alison Madrid<sup>1</sup>, Patricia I. Pontón<sup>2</sup>, Flávio Garcia<sup>3</sup>, Michel B. Johnson<sup>4</sup>, Mary Anne White<sup>4</sup>, Bojan A. Marinkovic<sup>1,\*</sup>

<sup>1</sup> Department of Chemical and Materials Engineering, Pontifical Catholic University of Rio de Janeiro (PUC-Rio), 22453-900, Rio de Janeiro, RJ, Brazil

<sup>2</sup> Department of Materials, Escuela Politécnica Nacional, 170525, Quito, Ecuador

<sup>3</sup> Centro Brasileiro de Pesquisas Físicas (CBPF), 22290-180, Rio de Janeiro - RJ, Brazil

<sup>4</sup> Clean Technologies Research Institute, Dalhousie University, Halifax, Nova Scotia B3H 4R2, Canada

<sup>5</sup> Department of Chemistry, Dalhousie University, Halifax, Nova Scotia B3H 4R2, Canada